2011-01-01

Design and CFD Optimization of Methane Regenerative Cooled Rocket Nozzles

Christopher Linn Bradford
University of Texas at El Paso, christopherbradford@yahoo.com

DESIGN AND CFD OPTIMIZATION OF METHANE

REGENERATIVE COOLED ROCKET NOZZLES

CHRISTOPHER LINN BRADFORD

Department of Mechanical Engineering

APPROVED :

_____
Jack Chessa, Ph.D., Chair

_____
Ahsan Choudhuri, Ph.D.

_____
Cesar Carrasco, Ph.D.

_____
Benjamin C. Flores, Ph.D.
Acting Dean of the Graduate School

DESIGN AND CFD OPTIMIZATION OF METHANE REGENERATIVE COOLED ROCKET NOZZLES

by

CHRISTOPHER LINN BRADFORD, B.S.A.E.

THESIS

Presented to the Faculty of the Graduate School of

The University of Texas at El Paso

in Partial Fulfillment

of the Requirements

for the Degree of

MASTER OF SCIENCE

Department of Mechanical Engineering

THE UNIVERSITY OF TEXAS AT EL PASO

August 2011

ACKNOWLEDGEMENTS

The material contained herein is being conducted in conjunction with work for the Center for Space Exploration Technology Research (cSETR) at the University of Texas at El Paso, under principal investigator Dr. Ahsan Choudhuri. The cSETR is a National Aeronautics and Space Administration (NASA) supported Group 5 University Research Center awarded in fiscal year 2009 under award number NNX09AV09A. More information can be found at [1] and [2].

TABLE OF CONTENTS

LIST OF TABLES

LIST OF FIGURES

CHAPTER 1

INTRODUCTION TO THE REGENERATIVE COOLING CONCEPT

The extreme thermal and stress loadings encountered by rocket engine combustion chambers is of critical importance to the design life of the engine, and subsequently the mission life of the unit to which the engine is attached. Missions beyond the orbit of Earth into deep space require a highly reliable engine with a long life of multiple firing cycles, especially since the engine is not able to be serviced once launched. Adequate cooling of the engine nozzle, throat, and combustion chamber is essential for such long equipment lives, and is typically performed through some active cooling method.

The use of regenerative cooling involves the fuel of a liquid fed engine being forced through channels adjacent to or forming the nozzle, throat, and chamber walls. A conceptual view of the process is shown in Figure 1-1. Typical applications are shown in Figures 1-2 and 1-3, where the channels are milled out of an inner liner wall (usually some copper alloy) and closed off by an applied outer jacket shell (usually some nickel alloy), which is marked conceptually in Figure 1-4. There are many machinable cross sectional sizes, shapes, and topologies possible for the channels as can be seen in Figure 1-5. In particular, the size is determined by the aspect ratio (AR) of the cross section for the rectangular shape, seen and defined in Figure 1-6. Changing the cross section along the channel length is also a possibility, and is especially important in the design for optimal channel pressure drop from the inlet to the outlet. Various lengthwise shapes are shown in Figure 1-7. Finally, the number of channels placed about the engine circumference can be varied, all for the purpose of optimal heat transfer away from the wall and to the cooling fluid with an acceptable pressure drop along the channel length.

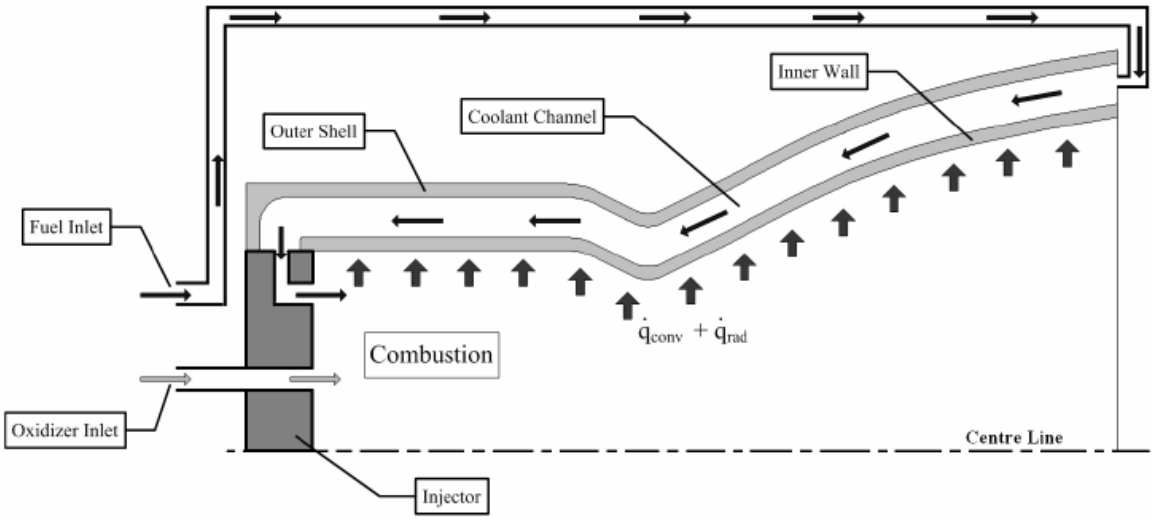

Figure 1-1: Conceptual view of the regenerative cooling technique for a bi-propellant liquid rocket engine. Obtained from [3].

Figure 1-2: Typical milled out liquid rocket engine cooling channel application on the inner liner with detached outer jacket portion. Obtained from [4].

Figure 1-3: Typical cross section showing copper alloy inner liner with milled out channels and applied nickel alloy outer jacket. Obtained from [4].

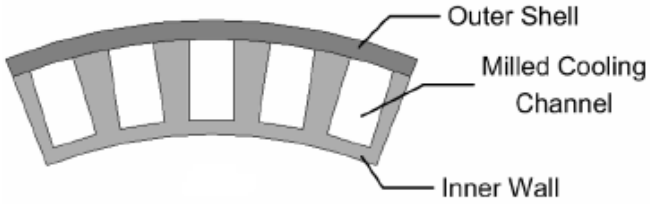

Figure 1-4: Conceptual view of engine cross section portion showing details of construction. Obtained from [3].

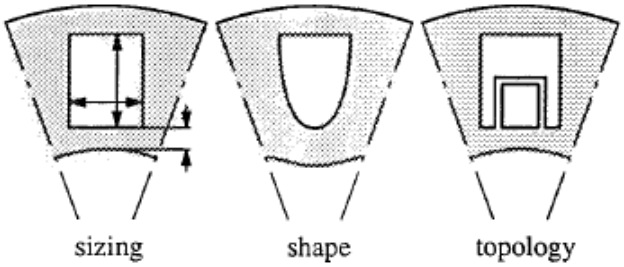

Figure 1-5: Example of possible channel cross sectional size, shape, and topology designs. Obtained from [5].

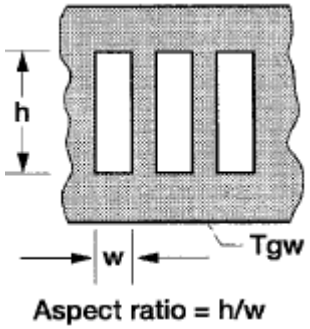

Figure 1-6: Rectangular channel with aspect ratio defined. Tgw represents the temperature of the wall inside the combustion chamber. Obtained from [6].

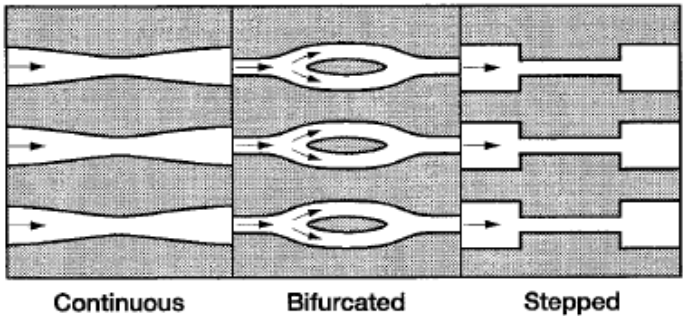

Figure 1-7: Various channel lengthwise shapes as viewed from the top. Obtained from [6].

During the steady state cooling process, the relatively lower temperature fuel picks up the heat conducted into the walls, and reduces the wall temperature to below critical material failure levels. As the walls are cooled the fuel is warmed, and depending on the feed system design of the particular engine, is either used to drive fuel and oxidizer pumps in an expander cycle and then sent to the injector plate, or directly dumped into the injector plate before entering the combustion chamber.

In most liquid rocket engines the non-steady state transient processes of throttling and pulsing the thrust, and stopping and restarting the engine are experienced. The changes in pressure and temperature then become higher over a shorter amount of time, and introduce the problems of cyclic loading, thinning, and failure due to material fatigue. Because of the inherent design of regenerative cooling, the location of highest fatigue stress and weakest structural strength can be at the bottoms of the cooling passages. This location separates the combustion gasses from the coolant, so material failure in this location would lead to total engine failure. Figure 1-8 depicts this scenario as well as indicates the locations of the other structural members in the vicinity where failure can occur, i.e. the fins and jacket.

The design of the cooling passages for adequate structural integrity is directly dependent upon the materials used and the cross sectional geometry details. A preliminary stress analysis must be performed even if the cooling performance is the primary focus. Then upon completion of the initial cooling passage design, a more detailed stress analysis would be necessary and structural improvements made. The structural improvements will affect the cooling performance, and the second cooling passage design iteration would be necessary, et cetera until the engine design is both structurally and thermally optimal. Furthermore, the design of the cooling passages for optimal cooling performance is highly dependent upon the fuel used in the

engine because of the different properties and behaviors of various useful propellants.

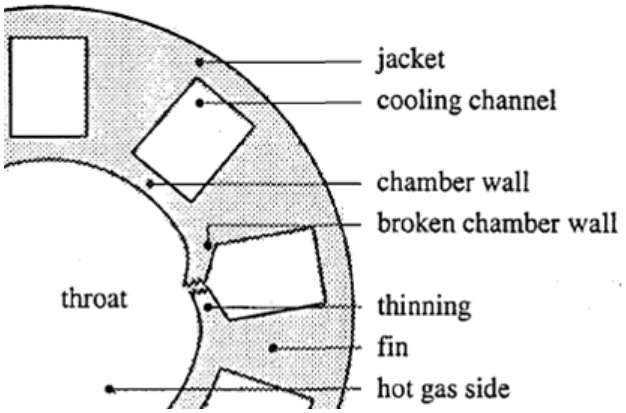

Figure 1-8: Cyclic thinning damage and failure due to material fatigue at the bottom of the channel. Adapted from [5].

The use of methane is attractive as the fuel for deep space missions because of its abundance on terrestrial bodies encountered in the exploration path. This abundance also opens the possibility for reduced initial launch weights from Earth, as the full-capacity fuel supply is not required at the launch time. Through a process known as "in-situ resource utilization", the fuel supply can be gained or refurbished during the mission, as mentioned in [7]. A liquid propellant engine designed to the properties of methane as the fuel are thus required. As shown in Figure 1-9 however, the typical operating conditions for methane are much closer to the critical point where phase change is a likely possibility, in contrast to the conditions of a more typical fuel such as hydrogen. The likelihood of phase change adds to the difficulty in modeling and using methane.

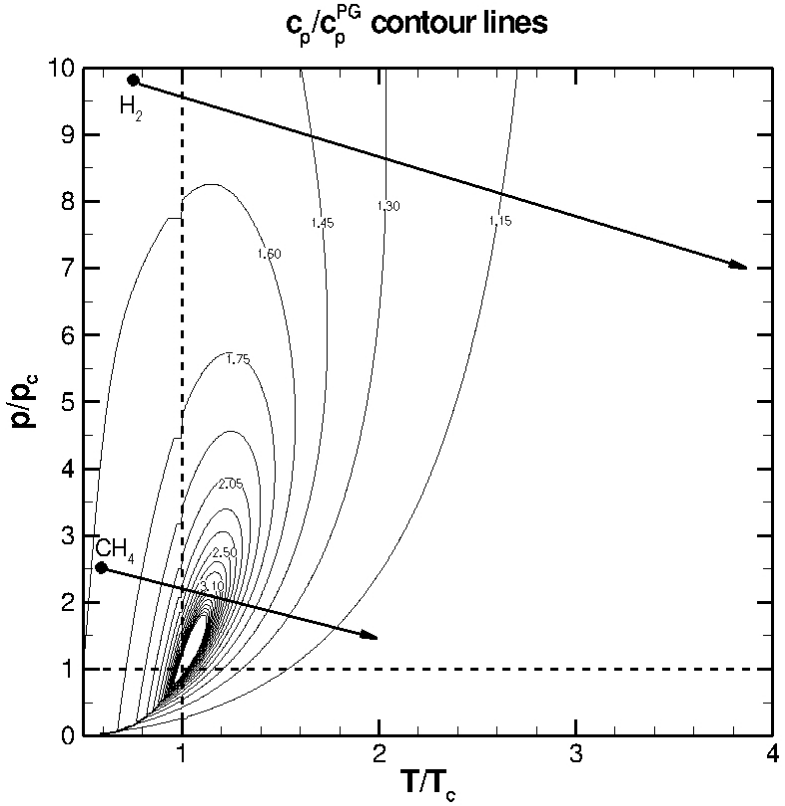

Figure 1-9: Typical hydrogen and methane channel operational conditions, with reduced constant pressure specific heat contours. Obtained from [8].

Various modeling options are available to represent the behavior of fluid materials. The use of computational methods not only reduces the time and expense required in a design, but also allows for multiple design iterations to be performed before a finalized "best" design is determined. Luckily computational fluid dynamics (CFD) software is available with the desired features, but challenges remain. As with any commercially available modeling software, or software that the user does not create themselves, it is essential to research the software functionality and limitations in detail before attempting to model any process with the desire to achieve useful results.

The objective of the present research is to design the regenerative cooling channels for the current 50 pound force (lbf) thrust engine designed and studied by the Center for Space

Exploration Technology Research (cSETR), per [9]. The engine design as shown in Figure 1-10 has the purpose of using methane as the fuel and coolant, with liquid oxygen as the oxidizer. Methane is thus used as the working fluid for the channels in the present research. A comprehensive literature review is performed to account for the limited sources of directly applicable design information relevant to the specifics of using methane as the fuel for this thrust class of engine. Taking only the inner shape of the engine, a preliminary stress analysis is performed to obtain certain material geometric features. A preliminary thermal and flow analysis is then performed to obtain additional geometric and flow details. These features are then built into computational models to obtain a baseline design set. The CFD software ANSYS FLUENT, version 12.1.4, is next used to determine the optimal configuration for the first iteration of the channel design, and an analysis of the results given. Finally, improvements and suggestions for future researchers are given.

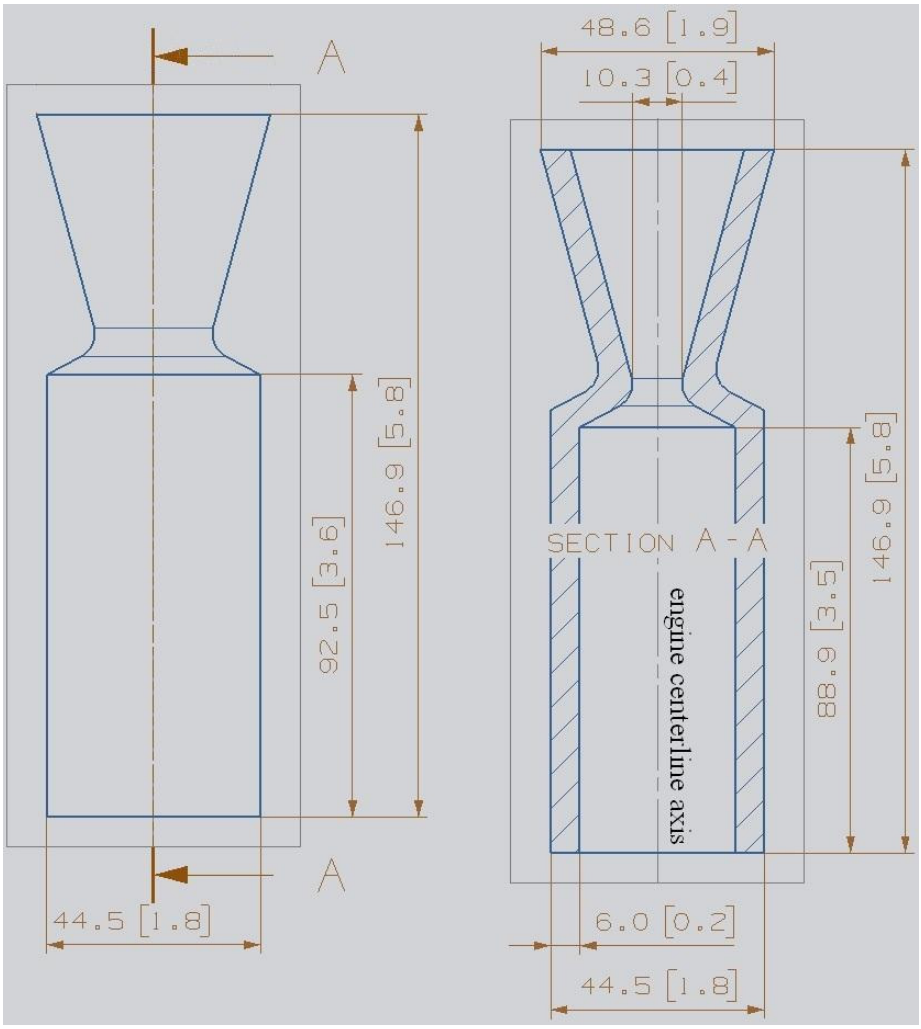

Figure 1-10: cSETR designed 50lbf thrust rocket engine, units of "mm [in]". Obtained from [9].

CHAPTER 2

LITERATURE REVIEW CONCERNING REGENERATIVE COOLING

In this chapter, a review of past work in the field of regenerative cooling of liquid rocket engines and the use of methane as both the coolant and the fuel is presented. The importance of an integrated engine cooling system (rather than an added-on feature) necessitates the consideration of multiple engine design aspects. General information obtained from the references is given, with specific mathematical equations placed in the subsequent chapter on mathematical theory. Units have been converted to usable values.

2.1 Cooling System Construction and Geometric Considerations

The construction of liquid propellant rocket engines with the purpose of utilizing regenerative cooling can be carried out using two main methods, both depending on the application. The choice of method depends on many factors.

The first method is tubular wall thrust chamber design, detailed in [10], and involves forming the combustion chamber and nozzle using individual tubes which are joined together and held in place with outer rings. The tubes carry the fuel to act as the coolant. Experience and assumption are used for some sample calculations of [10] to state that the tube wall thicknesses for one hypothetical case study design using the Inconel X material is sufficient for the throat at 0.508 millimeters (mm). A value of 0.2032 mm is also given "from experience" for a separate sample calculation.

The second construction method, coaxial shell thrust chamber design, is only briefly described in [10]. This method involves the combustion chamber, throat, and nozzle created out

of one piece of metal, forming the *inner shell*. Other terms used in literature for the inner shell are: "inner liner", "combustion chamber liner", "inner wall", or similar. Material is either cut or otherwise extracted from the inner shell material to leave the cooling channel voids; also known as the "slots". The voids are enclosed by an additional outer piece called the *outer shell*. Other terms for the outer shell are: "outer wall", "outer jacket", "external jacket", "liner closeout", "closeout", "ligament", or similar. This coaxial shell method is seen in Figures 1-2, 1-3, and 1-4. As explained in [11], this channel construction method has become the preferred for regions of the engine requiring critical cooling capability. The size of the cSETR 50lbf engine of Figure 1-10 indicates that coaxial shell construction is the best method.

When the channels are created in the inner shell, the cross sectional distance between the bottom of the channels and the opposite surface adjacent to the hot combustion chamber gasses becomes the thinnest portion, termed the *chamber wall*. This is a critical design thickness deserving special attention. Other terms found in literature are: "liner", "inner shell thickness", "combustion chamber wall", "inner wall", "chamber inner wall" (sometimes a term for the combustion chamber wall surface adjacent to the hot gasses), "wall thickness", or similar.

The remaining material adjacent to the channel voids also becomes a critical design component for structural and thermal considerations, termed the *fins*. Other terms found in literature are: "web", "side wall", "channel side wall", "land", "landwidth", "fin width", "fin thickness", "rib", or similar. Furthermore, the terms "fin height", "channel height", "depth", or "channel depth" are equivalent.

Additional detail can be built into the channel geometry as important features affecting the cooling system performance. For tubular construction, [10] shows that the tubes can either be circular in cross section, elongated, or vary from circular to nearly square elongated as the

channel progresses along the axial length of the engine. One purpose for the cross sectional area variation is to adjust the coolant velocity as required for adequate heat transfer at any particular location, which has implications for the local and overall channel coolant pressure. Avoiding sudden changes in the flow direction or cross sectional area was mentioned. The coaxial shell construction used in [6] allows the channel geometries seen in Figure 1-7 with the same effect.

At the entrance of the channels, [11] shows that a circumferential manifold is required to inject the coolant and distribute it evenly to all channels, requiring flow direction and area changes. At the exit, a coolant-return manifold is required to capture the coolant for placement into the mixing head and injector plate. The cooling channel design can be performed without considering the manifold heat transfer effects, but should consider some flow effects.

The "Thermal Skin^{TM}" fabrication concept of [12] is similar to the coaxial shell design when seen in cross section. For a rectangular shape, the "based on past experience" and 1968 state-of-the-art channel fabrication limits are given as:

a) maximum AR = 1.33

b) minimum channel width possible, w = 0.3048 mm

c) minimum fin width possible, $\delta_f = 0.381$ mm

d) minimum chamber wall thickness possible, t = 0.635 mm

e) fin width to channel width ratio, $(\delta_f / w) = 1$

An unexplained analysis is referenced to suggest that these dimensions maximize the fin efficiency. The efficiency concept is found in [6] and [13], and used with more detail in [7] and [14].

The modern Space Shuttle Main Engine (SSME) also utilizes the coaxial shell construction method, but as explained in [15] there are three shells: inner, middle, and outer. A comparison

to tubular construction is made, showing that for temperature considerations the coaxial shell channels are preferred over tubes. From a pressure stress consideration, a thinner wall is achievable using tubes with the manufacturing limits of the time for channels. The discussion of channel geometry suggests that the SSME channels are manufactured using the 1973 state-of-the-art milling fabrication limits. For a rectangular cross section, the SSME channel geometry is given as:

a) channel width, w = 1.016 mm
b) channel height, h = 2.54 mm
c) closeout (middle shell layer) thickness, t_m = ~1.27 mm
d) unspecified chamber wall thickness; range analyzed = 0.508 mm to 0.7112 mm

The effect of combustion chamber wall thickness in relation to the maximum thermal benefit is discussed and shown in a figure with some ambiguity. The construction at the throat region of the SSME is detailed in [11] and shows that the throat can be considered comprised of only the inner and middle shells. Channel geometry is given there as:

a) throat channel width, w = 1.016 mm
b) throat chamber wall thickness, t = 0.7112 mm
c) non-throat channel width, w = 1.5748 mm
d) non-throat chamber wall thickness, t = 0.889 mm

The work of [16] focuses on engines producing thrusts at levels near the cSETR 50lbf engine. Dimensional limits are given of previous studies for non-tubular coaxial shell construction using the 1982 state-of-the-art fabrication as:

a) minimum channel width, w = 0.762 mm
b) maximum AR = 4

c) minimum fin width, $\delta_f = 0.762$ mm

d) minimum chamber wall thickness, t = 0.635 mm

It is explained that in low thrust engines, regenerative cooling requires very small channels with the maximum possible coolant surface area. To achieve this, narrow and tall channels are suggested instead of the wide and shallow ones of larger engines. This results in AR values which are large, termed "high aspect ratio". In consideration of the thrust and pressure class of the cSETR 50lbf engine, channels thinner than the given 0.760 mm minimum standard are suggested. Graphical placement of the thrust and chamber pressure of the cSETR 50lbf engine gives a range of minimum channel widths required for cooling using methane of: 0.127 mm < w < 0.254 mm for a mixture ratio of oxidizer to fuel of 3.5. These minimums are suggested based on channel plugging potential and limits of coolant filtration. Later in [16], the minimum channel width for LO_2/LCH_4 at 100lbf thrust is stated as calculated, for design points which are not clearly determined on figures in the electronic copy of the reference, to be 0.0760 mm. The minimum widths possible would actually be limited to the fabrication capabilities, and cooling is possible in general if the calculated minimums are smaller than the fabrication minimums.

The potential for formulating important design ratios using detailed tabular data for the throats of the experimental geometries considered in [16] will need to be determined. The information in Table 2-1 is the most useful for this purpose. Multiple figures which may show the ratio values graphically and in general are not presented clearly in the electronic copy of this reference. One figure in particular causes confusion when attempting to calculate a ratio based on the pressure differential between channel and chamber for the zirconium copper material, which shows a range not typical of other values given. A partial equation is also depicted which, upon reformulating the equations of [17] for the analysis of a statically indeterminate beam,

results in a fully defined equation with the same terms and in the same form. However, confidence in [16] is not allowed due to the lack of information.

Table 2-1: Geometric values for channels tested in [16].

Throat Radius, r_t , [mm]	Channel Width, w, [mm]	Number of Channels, n_c	Channel Height, h, [mm]	Chamber Wall Thickness, t_{wall} , [mm]
5.28	0.301	86	3.08	7.6
5.28	0.338	83	1.69	7.6
5.28	0.335	83	3.36	7.6
10.52	0.663	88	13.25	7.6
16.64	0.442	142	8.81	7.6
10.52	0.373	70	7.47	0.635
20.35	0.963	110	19.23	7.6
10.11	0.427	105	8.53	7.6
15.98	0.564	124	11.28	7.6
20.27	0.919	171	18.41	7.6
20.27	1.016	106	7.10	7.6
10.01	0.442	103	8.86	7.6
10.01	0.411	106	8.25	7.6
31.88	2.169	89	10.84	7.6
15.80	0.569	122	11.37	7.6

The benefits of high aspect ratio cooling channels (the HARCC concept) for coaxial shell construction are discussed and investigated in [18], with particular note of manufacturing improvements capable of achieving such geometries. The 1992 definition of "high AR" is given at greater than 4.0, with improvements to conventional fabrication methods allowing up to 8, and platelet technology providing up to 15. The three configurations tested and shown in Table 2-2 all used a chamber wall thickness of 0.89 mm, combustion chamber pressure of 4.136×10^6 N/m^2, and OFHC Copper.

Table 2-2: Geometric values for channels tested in [18].

Configuration Number	AR at Throat	Channel Width at Throat, [mm]
1	0.75	1.70
2	1.50	1.02
3	5.00	0.254

The works of [3] and [19] reference the AR fabrication capabilities stated in [18], adding that a current fabrication engine uses an AR of up to 9, and by referencing the fabrication supplier catalog [20] an AR = 16 is possible with height = 8 mm and width = 0.5 mm. The details of which cutter was found to create these dimensions was not given nor could be confirmed in [20] or [21].

The benefits of HARCC are also investigated in [6] with the goal of determining a design which gives optimal performance both without and with the limits of fabrication. Coaxial shell construction is considered, and the 1998 state-of-the-art milling capabilities are given as:

a) AR $\leq$ 8

b) channel height $\leq$ 5.08 mm

c) channel width $\geq$ 0.508 mm

d) fin width $\geq$ 0.508 mm

e) no sharp changes in channel width or height

This information is both reported and used in [7], which is a chore to read, but also uses the minimum chamber wall thickness from [16]. Seven channel designs with various combinations of channel geometries were studied in [6], with the shapes shown in Figure 1-7. Channel AR's and performance are determined without the limits of fabrication, then the limits are imposed and the channels reanalyzed, and finally an optimal design is determined. The results show that the

use of HARCC is beneficial independent of channel shape, but manufacturing techniques are least complicated with the "continuous" shape. The analysis obtained AR's in the range of 5.0 to 40.0 in the throat region for the designs without fabrication considerations, and from 5.0 to 7.561 with consideration. The detailed geometry tables provide the values given in Tables 2-3 and 2-4 which are useful for later determining important design ratios at the throat. A chamber wall thickness is not given for the engine analyzed, but can be estimated using the given combustion chamber pressure of 11 x 10^6 N/m^2, material, and maximum chamber radius of 0.06 m. The radius is from a figure suspected to be mislabeled as "diameter" based on the representation of the curvature in the figure, and the large thrust class of the engine. A picture showing a scale also suggests the error.

Table 2-3: Select geometric values for channels which consider fabrication from [6]. Note: values are not for the same axial location.

Design Number	Maximum Channel Height, [mm]	Maximum Channel Width, [mm]	Minimum Channel Width, [mm]	Minimum Fin Width, [mm]
1	5.08	0.889	0.5842	1.5494
2	3.175	0.635	0.508	0.5588
3	5.08	1.27	0.5842	1.5494
4	2.54	0.889	0.508	0.508
5	3.4798	1.905	0.508	0.508

Table 2-4: Select channel geometric information from [6].

Reference Table; Design	Maximum Channel Width, [mm]	Throat Fin Width, δ_f , [mm]	Throat Channel Width, w, [mm]	Throat Fin Height, h, [mm]	Fabrication Considered
A-I; 1	0.889	1.8796	0.254	10.16	no
A-II; 2	0.635	0.5588	0.508	2.54	no
A-III; 3	1.27	1.8796	0.254	10.16	no
A-IV; 4	0.889	0.5588	0.508	2.54	no
A-VIII; 1	0.889	1.5494	0.5842	4.4196	yes
A-IX; 2	0.635	0.5588	0.508	2.54	yes; "good" design
A-X; 3	1.27	1.5494	0.5842	4.4196	yes
A-XI; 4	0.889	0.5588	0.508	2.54	yes; "better" design
A-XV; 5	1.905	0.5588	0.508	2.54	yes; "optimal" design

Many of the above mentioned references concerning HARCC are also used by [14] in an attempt to build upon their results with a numerical and experimental correlation. The experimental apparatus used is a large-scale rectangular channel with the following dimensions obtained through the numerical model:

a) AR = 8

b) length of unheated section = 0.254 m

c) length of heated section = 0.508 m

d) channel width = 2.54 mm

e) fin width = 2.54 mm

The computational models of [8] also consider a maximum AR of 8.

It is interesting to note the predominance in the literature of the geometric number combinations 2-5-4 and 5-0-8, either directly reported or as converted from the English unit system to the metric system. The trend began historically in 1967 with [10], where "experience"

and "assumption" were used to determine a "sufficient" value for the wall thickness of a tube using a particular material. The 1973 analysis of the SSME in [15] focuses on a range of values including the 5-0-8 combination, while listing a 2-5-4 built geometry measurement. Next, in the 1982 study of [16], which combines aspects of previous work in the field of low thrust class engines, the 2-5-4 value is marked graphically to designate its relationship to and requirement for specific chamber pressure and thrust levels, but the value itself falling outside the range of then possible fabrication capabilities. Detail is not given which explains the relationship in that work. The 1992 work of [18] actually uses the 2-5-4 value in an experimental apparatus geometry from an unspecified "extensively used" testing unit, and would require a reference investigation into that unit which would diverge from the current research. Then, the 1998 work of [6] lists unconfirmed and unreferenced "current milling capabilities" using the 5-0-8 values. The 2005 work of [14] attempts to build upon many of the previous works found, but quickly states that these number combinations found in their experimental apparatus geometry are obtained through an unspecified calculation process, without adequate explanation to give validity to the values. Finally, the 2006 work of [7] uses many of the same references discovered independently by the current researcher, and actually lists the fabrication criteria found in [6] and [16] but missed the additional information from [19].

It is seen in the literature that the field of rocket engine design has historically been pursued using the English unit "inches", and when the number trend is viewed in this way the values are interestingly only tenth divisions or multiples of inches: 20, 10, 0.20, 0.10, 0.05, 0.005, etc. The explanation for this could be assumed due to easily available length scales, however when designing a part using equations these values are not usually calculated as such, nor found with the increased use of the metric system. Nothing has been discovered in the literature to indicate

the use of rounding of calculated values.

The focus in the present research is on calculating the required values from referenced design ratios, mathematical theory, and computational modeling. Manufacturability requirements are also used as discovered in the literature, but not "historical" numbers which may not be valid with the latest technology. Current manufacturing capabilities are able to accommodate both English and metric units per [21], so the values calculated in the present research should be near values capable of being manufactured from either unit system. Finding the cutting tools which are closest to the values calculated is the responsibility of the manufacturing team, and goes beyond the focus of the current research.

2.2 Standard Materials Used in Engine Construction

The solid materials used for rocket engine construction must be selected based upon the various requirements of the initial design, engine mission, desired thermal and structural performance, and point location on the unit. Only specific metals and metal alloys are accepted for use in the field of rocket engine design.

The application based design book [10] gives a generalized section on proper selection of suitable materials, with many important points of consideration. Because the work was early in rocket engine development, the included groups of metals can only provide a holistic property evaluation to assist the engineer with an adequate material group selection for any particular generalized area of the engine system. However, multiple actual and hypothetical case study designs are presented for sample calculations using specific materials. Low-alloy AISI 4130 steel is mentioned for the tension bands and stiffening rings placed on the outer surface of a nickel nozzle and combustion chamber (termed the "thrust chamber" as one unit). The high

temperature, high strength nickel-base alloy Inconel X is also suggested for a regeneratively cooled thrust chamber of tubular wall construction. Materials suggested for the nozzle extensions which are radiation cooled include: molybdenum-titanium alloy, tantalum-tungsten alloy, titanium alloys, and the commercially alloy Haynes 25. An ablatively cooled thrust chamber may use the materials: ablative composites and resins, structural composite fiber glass, structural aluminum alloy, structural stainless steel, tungsten-molybdenum alloy, graphite, silicon carbide, and various bonding agents. Experiments conducted by [12] actually used Haynes 25 thrust chambers, as well as the nickel 200 alloy and the 347 stainless steel.

As discovered in [3], [11], [15], [16], [22], and [23], a high-strength copper base alloy containing zirconia and silver, such as NARloy-Z, is common for the inner shell. A limiting maximum temperature of 811 K is given, as well as the explanation that HARCC with relatively tall fins is only useful for a high thermal conductivity alloy which provides very effective heat transfer into the fins, such as alloys of copper. The essentially pure Oxygen Free High Conductivity (OFHC) Copper is considered by [3], [7], and [18]. However, [6] uses "oxygen free electrical" (OFE) copper, assumed similar to OFHC Copper, with a limit fatigue maximum temperature of 667 K. An intermediate middle shell would use layers of copper and nickel. The outer shell is commonly made with alloys of nickel for the purpose of handling expected loads. One in widespread application is the high-strength super-alloy Special Metals INCONEL® Alloy 718, detailed in [24] to be nickel based and containing chromium with a mixture of other metals.

An engine operating life definition is required to obtain the correct material property data to allow for a minimal failure design. For example, [15] states that the coaxial shell SSME is designed for an operating life of approximately 32 hours, with a NARloy-Z inner shell duty life of 100 cycles. An empirical life prediction is suggested for new engines. In the case of the

present research the expected operating life of the cSETR 50lbf engine is not currently known, but a preliminary analysis rupture life can be chosen at 100 hours with a duty life of 100 cycles.

Material property data is found directly or graphically in [6], [7], [15], [16], [23], [24], and [25], for NARloy-Z, various coppers including UNS C10200 OFHC Coppers, and Inconel 718. An endurance limit rupture stress, per the suggestion of [10], can be obtained for NARloy-Z from Figure 2-1, a yield stress from Figure 2-2, and a cyclic limit stress from Figure 2-3. Strain data useful for [15] and [22] found in [26] and [27] goes beyond the preliminary stress analysis of the present research. A yield stress for OFHC Copper Annealed can be found from Figure 2-4. All of the useful material property data obtained is collected in Tables 2-5, 2-6, and 2-7.

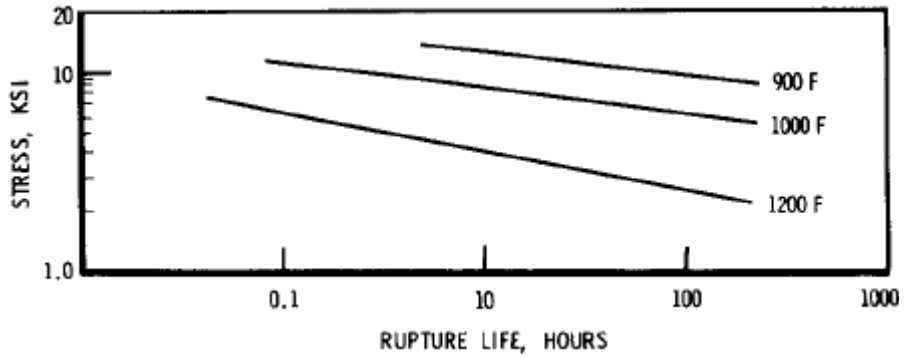

Figure 2-1: Rupture life of NARloy-Z at elevated temperatures. Obtained from [15].

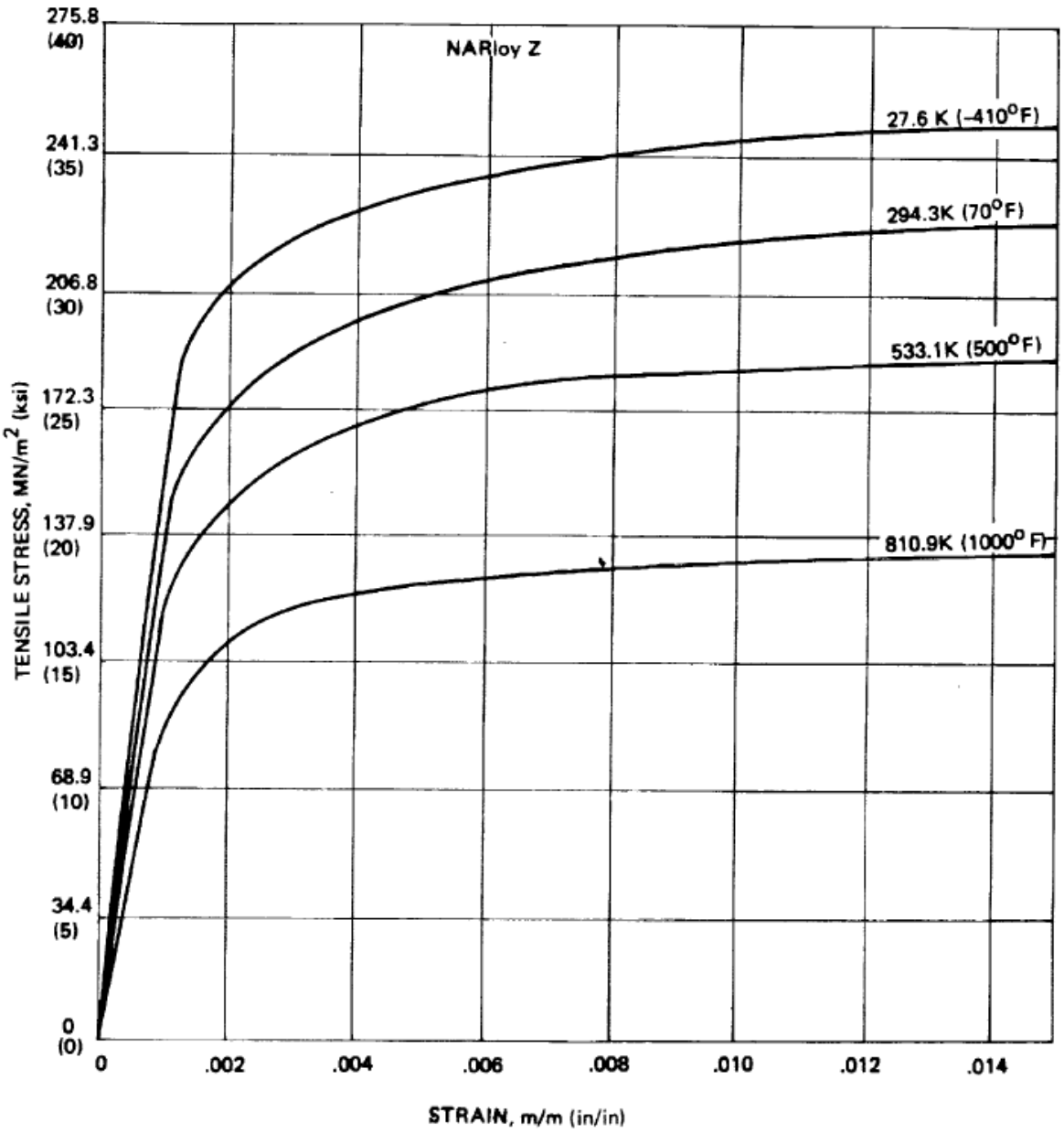

Figure 2-2: Stress-strain curves for NARloy-Z at various temperatures. Obtained from [25].

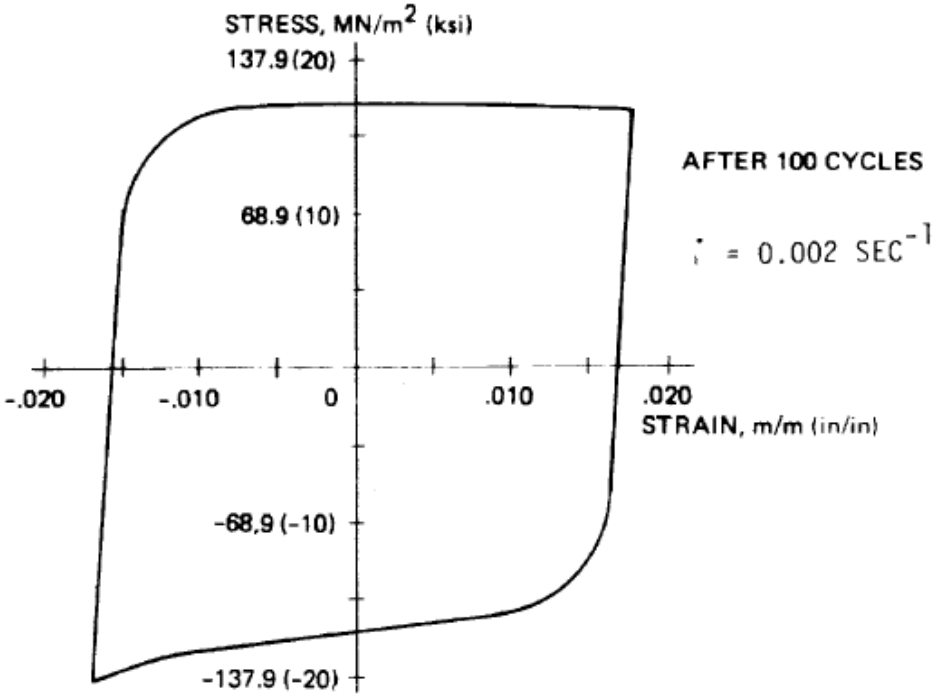

Figure 2-3: Cyclic stress-strain curve for NARloy-Z at 810.9 K. Obtained from [25].

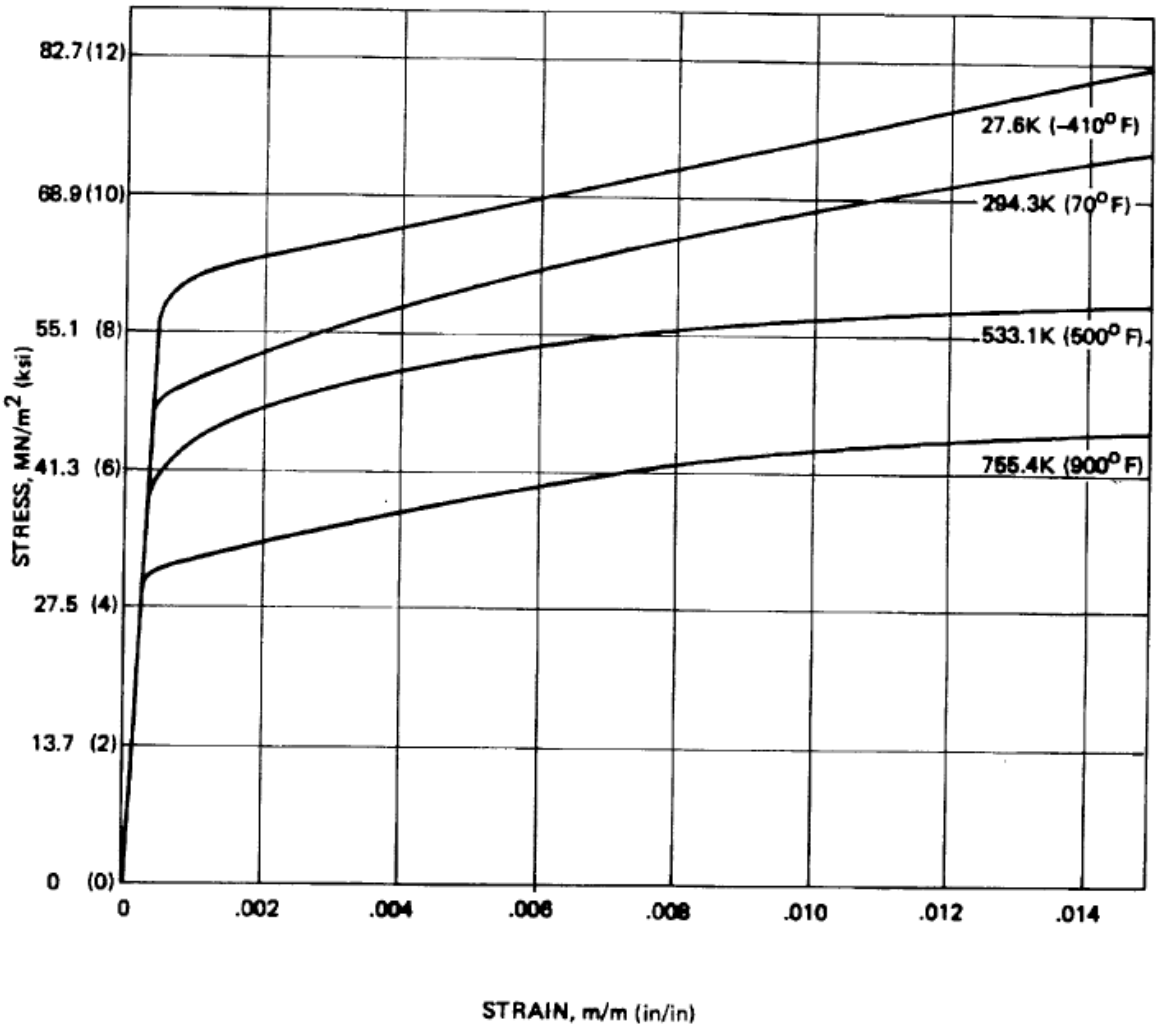

Figure 2-4: Stress-strain curves for OFHC Copper Annealed at various temperatures. Obtained from [25].

Table 2-5: Useful NARloy-Z material property data at the elevated temperatures expected, from various sources.

Property	Value	Source
Yield Tensile Stress, σ_Y , [N/m^2]	78.3875 x 10^6 at 810.9 K	[25], Figure 2-2
Ultimate Tensile Stress, σ_U , [N/m^2]	not required	[10]
Endurance Limit Rupture Stress, 100 hours, σ_R , [N/m^2]	20,684,271.8795 at 922.039 K	[15], Figure 2-1
Endurance Limit Cyclic Stress, 100 cycles, σ_E , [N/m^2]	137.9 x 10^6 at 810.9 K	[25], Figure 2-3
Modulus of Elasticity, E, [N/m^2]	127 x 10^9	[25]
Density, ρ , [kg/m^3]	9134	[25]
Specific Heat, Cp, [J/kg-K]	373	[25]
Thermal Conductivity, λ, [W/m-K]	295	[25]
Coefficient of Thermal Expansion, α , [(m/m) K^{-1}]	17.2 x 10^{-6} for 294 to 533 K	[25]
Limiting Maximum Temperature, [K]	811	[16], 1982
Limiting Maximum Temperature, [K]	867	[23], 2006

Table 2-6: Useful Copper material property data at the elevated temperatures expected, from various sources.

Type of Copper	Yield Tensile Stress, σ_Y , [N/m^2]	Ultimate Tensile Stress, σ_U , [N/m^2]	Melting Point, T_m , [K]	Source
Copper, Annealed	33.3 x 10^6	210 x 10^6	1356.35 to 1356.75	[24]
Copper, OFHC Soft	49.0 to 78.0 x 10^6	215 x 10^6	1356.15	[24]
Copper, OFHC Hard	88.0 to 324 x 10^6	261 x 10^6	1356.15	[24]
Copper, Annealed OFHC	29.915 x 10^6 at 755.4 K	202 x 10^6		[25], Figure 2-4
Copper, OFHC 1/4 Hard	310 x 10^6	330 x 10^6		[25]
Copper, OFHC 1/2 Hard	317 x 10^6	344 x 10^6		[25]
OFHC Copper			1355.56	[7]
OFE Copper			667, as limit fatigue max.	[6]

Table 2-7: Useful Inconel 718 material property data at the elevated temperatures expected, from [24].

Property	Value	Note
Yield Tensile Stress, σ_Y , [N/m^2]	980 x 10^6	at 923.15 K
Ultimate Tensile Stress, σ_U , [N/m^2]	1100 x 10^6	at 923.15 K
Density, ρ , [kg/m^3]	8190	
Specific Heat, Cp, [J/kg-K]	435	
Thermal Conductivity, λ, [W/m-K]	11.4	

2.3 Cooling Channel Pressure Requirements

The presence of the enclosed passage walls affects the pressure of a moving fluid between the inlet and the outlet, and thus the velocity and cooling performance, as explained in [12]. The difference between the inlet and the outlet pressures is what drives the fluid to move in the

passage, but [10] states that a minimum difference is desirable and suggests a "smooth and clean" inner surface. Various equations are given by [7], [10], and [14] for the hydraulic conduit pressure drop with terms that are not easily determined, such as those involving surface roughness. The influence of surface roughness as explained in [15] is that a more rough surface increases the heat transfer coefficient but also increases the channel pressure drop, thus negating any benefit.

The expander (or "topping") cycle engine is detailed in [10], [11], and [28], as one which uses the heated and thus expanded coolant gasses exiting the cooling channels to drive turbine pump machinery before being piped to the injector plate. The coolant path is shown in [7] as first exiting the storage tank, then piped through a pump, then sent through a feed line, and finally to the cooling channel inlet; incurring a 2.5% pressure loss in the feed line. At the outlet of the channel for a non-expander cycle engine, the coolant/fuel is piped directly to the injector plate before entering the combustion chamber.

Per [6], in order to prevent backflow into the channels from the combustion chamber, the pressure at the exit of the channel must be greater than the combustion pressure. The combustion pressure thus represents the minimum pressure allowed at the exit of the channel. Also, the pressure loss in the channel must be accounted for such that the channel inlet pressure is above the required exit pressure. Varying the cross sectional area along the length of the channel, such as with the "continuous" shape of Figure 1-7, has a major impact on designing for an optimal pressure drop from the inlet to the outlet.

Since the injector contributes an additional pressure drop for the coolant, the combustion pressure actually represents the minimum pressure allowed at the exit of the injector, per [10]. A rule-of-thumb value given for the injector pressure drop is 15% to 20% of the combustion

stagnation pressure. An alternative channel outlet pressure to chamber pressure ratio is assumed by [12], without specifying the source of this pressure drop. Other criteria used in the past is given in [16]:

a) minimum regenerative-coolant discharge pressure:
    1) for liquid, p = 1.176 x chamber pressure
    2) for gas, p = 1.087 x chamber pressure
b) maximum coolant velocity:
    1) for liquid, v = 61 m/s
    2) for supercritical gas, v = Mach 0.3

The criteria actually used in the analysis of [16] include a minimum channel outlet pressure based on an allowable injector pressure drop, related to the chamber pressure. The minimum allowable channel pressure drop from inlet to outlet is also a function of chamber pressure, and values are given graphically.

The desired effect of maximizing the coolant temperature rise with an associated minimization of channel pressure drop is studied in [6], [7], and [8]. The pressure drop is determined in [6] with weakly defined equations written into a computer code. The results indicated that for a "continuous" channel length shape, designing the HARCC to accommodate the throat region always provides the highest benefit for temperature reduction. Unfortunately the same channel cross section used along the length of the engine causes an undesirable high pressure drop, but the continuous shape manufacturing method allows for later width increase determination in the non-throat regions to give a beneficial low pressure drop. Optimizing the uniform cross section channel for temperature reduction at the throat can thus be performed first, and later the optimal cross sectional variation for pressure drop reduction can be determined.

The results also indicated that the optimal channel design used the "bifurcated" shape, but the pressure drop was slightly higher than by not using that shape. The results of the "continuous" shape showed a maximum coolant channel pressure drop of 5.0×10^6 N/m^2 for an engine much larger than the cSETR 50lbf engine.

2.4 Aspects of Heat Transfer

The heat transfer in a regeneratively cooled rocket engine is based on the fundamentals of heat transfer theory. The system can be divided into four control volumes for consideration of heat transfer analysis, based upon the geometry of the cross section of coaxial shell designs. The first: the heat transferred from the hot reacting combustion gasses comprised of the fuel and the oxidizer components as they interact thermally with the combustion chamber wall. The second: the heat transferred from the chamber-wall/inner-shell-structure to the cooling fluid inside the channels. The third: the heat transferred from the inner shell to the adjoining portion of the outer shell. The forth: the heat transferred from the outer shell to the external surroundings.

2.4.1 Basic Heat Transfer Theory

The basic fundamentals and theory of heat transfer are covered in detail within [13] and [29], and specifically as related to rocket engines per [10], [14], [28], and [30]. The equations required for the field of regenerative cooling are the same as those required for any heat transfer application. Beginning from Fourier's Law, the generalized steady-state one-dimensional (1D) equation for heat flux per unit area, $\dot{q}$, is obtained with a coefficient term that gives its generality. The coefficient term takes different definitions depending on which mode of heat

transfer is being modeled. For convective heat transfer between adjacent solid and liquid zones, the coefficient is termed the "heat transfer coefficient" or "film coefficient", α_g. For conductive heat transfer through solids, the coefficient involves the material thermal conductivity and a material thickness. The basic equations can also be rearranging for laminar or turbulent flow considerations.

Special groupings of terms are often used to describe the degree of heat transfer, described in [13] and [29]. For a fluid, the Nusselt number is the ratio of convection heat transfer to conduction, and itself contains the heat transfer coefficient. For a solid/fluid interface, the Biot number is the ratio of the internal thermal resistance of a solid to the external convective resistance at the surface. The graphical explanation of the Biot number is informative for cooling channel heat transfer if the contained terms can be directly manipulated.

2.4.2 Gas Side Heat Transfer

The heat transferred from the hot reacting combustion gasses to the chamber *hot-wall* is termed the "Gas-Side Heat Transfer" in [10]. This combustion chamber wall surface area adjacent to and facing the hot combustion gasses is equivalently termed in the literature as: "hot-gas-side", "hot-gas-side wall", "hot gas wall", "chamber wall", "chamber inner wall" (sometimes a term for the thinnest part of the inner shell), or similar.

The main mode of heat transfer is described by [10] as forced convection, since the combustion gasses are traveling at a high velocity adjacent to the hot-wall. Three correlations are given for the determination of the heat transfer coefficient, one is a "rough approximation", the second is "a much used" equation of Colburn, and the third is the equation of Bartz. The choice of which correlation to use is based on the available formulation. The "rough

approximation" equation contains terms which are not easily obtained without extensive experimental data. The equation of Colburn takes the form of a Nusselt number, but the dimensionless constant is not specified in [10] and the equation may therefore be unusable. Finally, the equation of Bartz appears most complicated, but contains easily obtainable geometric terms. Other terms can be obtained approximately through the use of other correlations given in [10] or should be known for the particular engine.

For example, the ratio of specific heats is needed for the combustion mixture of O_2 and CH_4, which are given individually by [31] at 300 K as: $\gamma_{O2} = 1.395$, $\gamma_{CH4} = 1.299$. The mixture specific heat ratio can be found using a weighted sum of the partial molar fraction of individual ratios, per [32]. Next, the specific heat of the mixture can be found using an equation given by [10] and [31].

There is one temperature variable which is not specified in [10] for the Bartz equation, the unknown inner wall temperature on the hot gas side. This temperature is both a design value to be optimized and contained in the standard heat flux equation, causing some confusion. The Bartz correction factor term contained in the Bartz equation is easily determined using the provided graphs, seen in Figure 2-5, rather than a direct calculation. The Bartz equation seems the preferred method of [10] to determine an approximate value for the heat transfer coefficient along the chamber wall, with an unspecified "short form" used in [12].

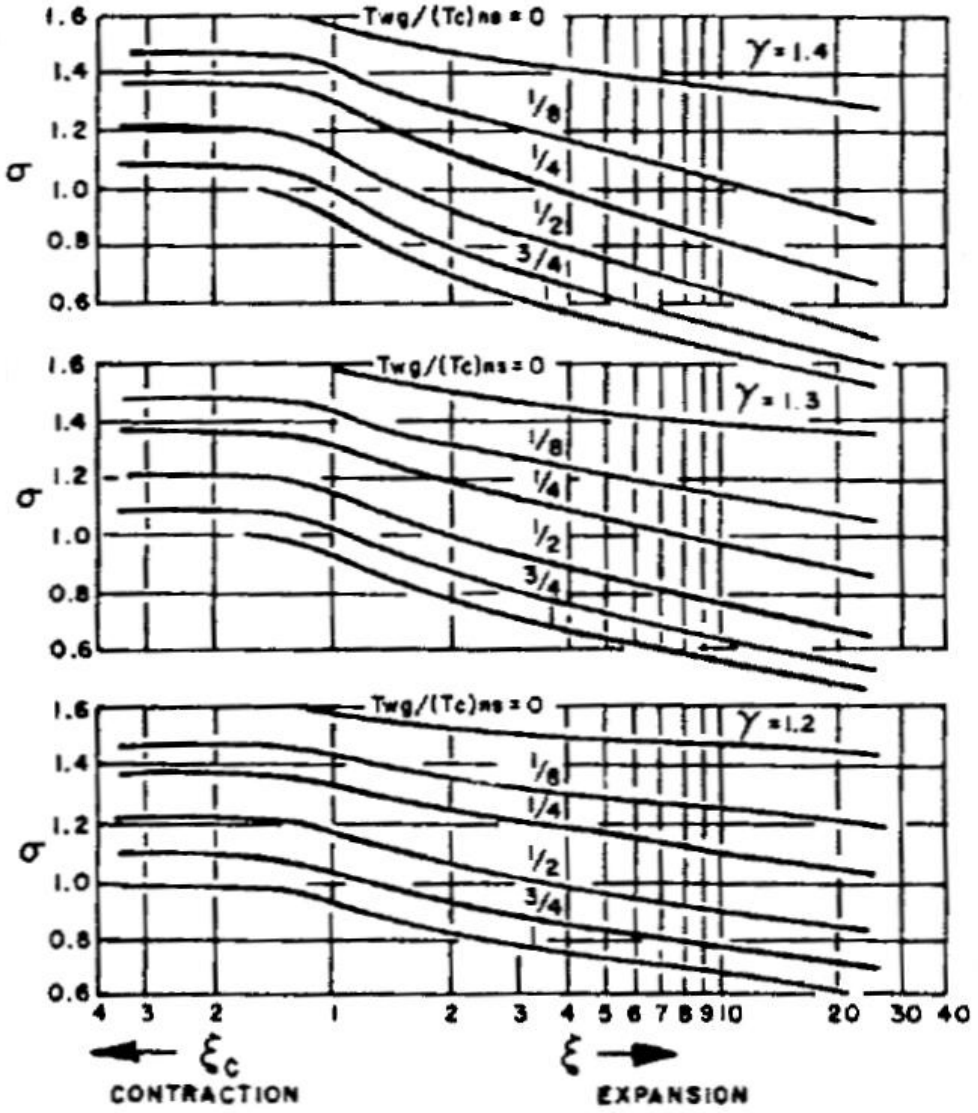

Figure 2-5: Bartz equation correction factor values (σ) for various temperature and specific heat (γ) ratios at axial locations of ξ. ξ is the ratio of the local area to the throat area. ξ_C is in the chamber, one indicates the throat, ξ is in the nozzle. Obtained from [10].

The area ratio term in the Bartz equation indicates that the heat transfer coefficient will be maximum at the throat region, and when applied in the heat flux equation suggests the maximum temperature will also be experienced at the throat. The throat thus becomes the critical cooling region where the heat flux will be highest, and where the number of cooling passages required for a particular coolant flow rate should be determined. This is confirmed by [3], [6], [10], [12],

[18], [23], [28], [33], and [34].

The work of [28] gives valuable points of information which are essential to understanding the heat transfer coefficient equations presented in other works. Specific terms are depicted in the most basic dimensional analysis form for easy correlation. The calculation of the gas-side heat transfer coefficient is by the Bartz equation, giving essential details about the equation that are left out of other literary works. A figure plots experimental data and the Bartz equation to confirm that the equation in the given form accurately predicts the heat flux along the combustion chamber contour, peaking at the throat. With engine contour geometric terms known and contained in the Bartz equation directly, the equation can be used to give the heat transfer coefficient variation required if using a computational model of straight channels with no curvature. The work of [30] notes that the Bartz equation is only valid in the region near the nozzle throat.

A "modified" version of the Bartz equation presented in [7] and [14] more closely resembles the Sieder-Tate or Dittus-Boelter relationships applicable to flow inside a tube or channel when found in [13] or [29], and may not accurately represent the axial variation of hot-wall heat transfer coefficient. A similar correlation used for the coolant side is mentioned by [14] but not detailed. The validity of using this modified version can not be verified.

Carbon solids deposited on the interior combustion chamber walls by the combustion gas products are also considered in [10] and [12] as a form of resistance to heat transfer, reducing the effective coefficient value. The explanation as to whether this is a positive or negative condition is not given in either work.

In consideration of the channel geometry cross section, [15] states that the influence of the fin width to channel width ratio on the chamber wall temperature, for a constant coolant pressure

drop, is negligible for $(2/3) \leq (\delta_f / w) < 2$.

2.4.3 Regenerative Cooling and Coolant Side Heat Transfer

The heat transferred from the chamber-wall/inner-shell-structure to the cooling fluid inside the channels falls under two headings in [10], "Regenerative Cooling" and "Coolant Side Heat Transfer", with aspects of the previously mentioned heat transfer from the combustion gasses to the chamber wall. The heat transfer mechanism is described as a generalized heat flow between two fluid regions separated by a multilayer partition, utilizing multiple heat flux equations. This is the same mathematical approach taken by [7], detailed in [13], and shown schematically in Figure 2-6, where T_{aw} represents the adiabatic wall temperature caused by the combustion gasses, T_{wg} represents the actual hot-wall temperature on the combustion gas side, T_{wc} represents the actual wall temperature on the coolant side, and T_{co} represents the bulk temperature of the coolant inside the channel. The effects of the boundary layers, caused by the two moving fluids, are shown to depict the change in temperature due to the heat transfer coefficients on the walls. The heat transfer from the side wall of the coolant passage and not just the bottom wall, the "fin effect", is not given with this description. The extended surface fin effect is derived in detail in [13] and [29], which give equations for determining the material conductive height necessary for efficient heat extraction through convection to the surrounding fluid. The theory required to obtain the fin height is based upon longitudinal heat conduction in a rod, with corrections to account for a non-adiabatic tip. The concept is utilized with lack of detail in [7], [12], and [14].

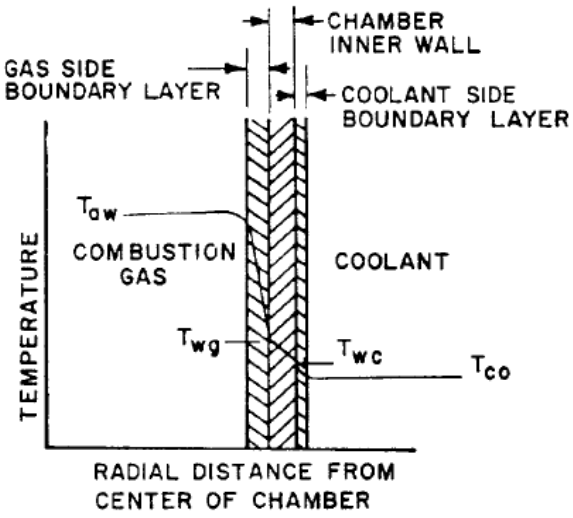

Figure 2-6: 1D heat transfer schematic representation of regenerative cooling. Obtained from [10].

When analyzed separately from the combustion gas region, the heat transfer from the channel wall into the adjacent coolant falls under the category of "Coolant Side Heat Transfer" in [10]. Equations are given which describe the heat transfer coefficient for two cases of coolant state properties, important when considering non-ideal fluid behavior. The Sieder-Tate equation for turbulent heat transfer to liquids flowing in channels is for the case of nonboiling subcritical temperature, and subcritical to supercritical coolant pressures. This equation takes the form of a Nusselt number, and contains an unknown constant which is specific to the coolant being analyzed. One sample calculation in [10] suggests the use of this equation for the propellant RP-1 and uses unspecified experimental data to give the constant as $C_1 = 0.0214$. The generalized presentations of the equation in [13], [29], and a partial form in [35], give the constant as $C_1 = 0.023$. The work of [7] is concerned with methane directly and gives the constant as $C_1 = 0.027$, but the source used for the equation is extremely old and the equation has slightly different exponent values. The second equation given by [10] is for the case of a vapor-film boundary layer where the coolant is at supercritical pressure and temperature, suited for hydrogen per

Figure 1-9 which shows the supercritical operating conditions. The choice of which of the two equations to use for methane is not clear since a boiling phase change could occur. An equation to estimate the coolant system capacity is also given.

The work of [16] gives an equation for the heat transfer to the homologous propane as assumed characterizing that for methane, in the form of a Nusselt number. The equation is not fully explained and given by a reference which at times gives unclear information and mathematical relations, thus the equation is not considered useful.

The text [28] gives an equation based on theory and other researcher formulations to directly predict the coolant side film heat transfer coefficient in cooling tubes, in a form which allows application to non-circular channels. With this form, comparisons and proper utilization can be achieved with equations presented in other literary works lacking detail.

2.4.4 Solid to Solid Heat Transfer

The heat transferred from the inner shell to the adjoining portion of the outer shell by direct contact conduction between two solid regions is described in [13] and [29]. The fin effect is linked to the solid-to-solid heat transfer since the bottoms of the fins mathematically touch and physically join the chamber wall at a control volume boundary, and the tops of the fins are what is touching the outer shell at a physical boundary. The typical assumption of an adiabatic fin tip per [7] is not valid as a proper boundary condition in a CFD simulation since heat can be transferred, and [13] gives the required mathematical adjustment for a non-adiabatic tip.

2.4.5 Outer Shell Heat Transfer

The heat transferred from the outer shell to the external surroundings can be considered as the final form of heat removal for the coaxial shell engine design. Taking this form into consideration is important for proper definition of numerical boundary conditions. Radiation cooling is only discussed in [10] in relation to nozzle extensions, but is detailed in general by [13] and [29]. The heat flux equation requires a coefficient value depending on the material and surface finish. The emissivity of a wall surface made with oxidized (or rough surfaced) nickel is given as $\varepsilon_{ext} = 0.41$ at 373 K by [29].

The work of [11] discusses the topic of engine testing. Static ground testing at sea-level conditions is one method mentioned, even used in [18], which involves natural or forced convective cooling in atmosphere. Equations to determine the required mean heat transfer coefficient over a flat plate from [13] can be used for an idealized flat outer portion of an engine.

Testing in an altitude chamber for engines designed to operate in thinner atmospheres is also mentioned in [11]. Thus considering the operating conditions of an engine being utilized for interplanetary travel in the vacuum of space, as in the current research, it is practical to consider radiation cooling as important on the outer shell. The work of [7] considers this, but makes the assumption of an external temperature of absolute zero as well as an over simplified heat flux balance.

2.5 Material Loading, Stress, and Failure

Sufficient structural strength is necessary in the design of a regenerative cooling system, as the system is also integrated with the design of the engine itself. The focus of the present

research is on the cooling performance, but a structural design is required to possess at least the minimum strength necessary in terms of mechanical and thermal loads.

An analysis of the expected working loads on the engine due to the cooling system is required and discussed in [10]. Typical recommended safety factor criteria are given for the design limit load, yield load, ultimate load, and endurance limit. As explained, the endurance strength limit of a material should be used in place of the ultimate strength value in cases of cyclic loading operation, typical of the multiple starts and stops of a rocket engine. Many failure modes are evaluated and discussed, the complexity of which suggests that a detailed analysis is required for proper final designs. For a preliminary stress analysis though, only static and some cyclic failures can be considered to determine a baseline structure for an engine.

The design loading criteria of [10] is contradicted in [15], which states that some components are designed within a yield strength criterion of an increased multiple of the yield stress for the material, $1.1 \times \sigma_y$. Designing a part by artificially increasing (rather than decreasing) the material limits would decrease the ability of the part to handle loading, resulting in a weaker design. The criteria of [10] increases the expected loading for a consistent material property, resulting in a stronger and thus more desirable conservative design.

In structural terms, [10], [15], and [18] describe the throat as the critical design location where maximum stress will occur, and at the inner chamber wall surface of the inner shell. The throat is thus in the area with the shortest life expectancy, and where material damage will likely begin. An equation given for the coaxial shell stress goes beyond the scope of a preliminary analysis, and furthermore includes terms that are unknown before a numerical analysis is performed. Other equations found in [10] are not sourced but are discovered to be the same as the basic mechanics of materials theory of [17], which itself states that the same theory be used

in many other areas of rocket engine stress design.

In a more general sense, [10] continues by explicitly stating that the coolant pressure causes only a circumferential hoop stress in the outer shell. Also, the inner shell experiences both a compressive stress and a thermal stress. The compressive stress is caused by the pressure differential between the coolant and combustion chamber, whereas the thermal stress is caused by the temperature gradient across the chamber wall. These stresses can also be analyzed using the methods of [17].

Since the chamber wall represents the thinnest portion of the inner shell, [15] and [7] describe the minimum allowable thickness as directly related to the channel width when considering pressure stresses and failure. The generalized failure mode descriptions of [10] are expanded upon in [15] to a more detailed duty cycle equipment life analysis with focus on this thinnest location. For a preliminary stress analysis, the accumulation of stress rupture creep damage and low cycle fatigue damage are important. These damages are ignored by [7].

For the consideration of stress rupture creep damage, the endurance limit determination using [15] and Figure 2-1 for the NARloy-Z material at a chosen rupture life allows a design of the channel width and chamber wall thickness which minimizes failure in this manner. Fatigue specimen data showed that this damage is minimized by using the narrow channel width of 1.016 mm reported, with a resulting increase in the number of possible life cycles.

For the consideration of low cycle fatigue damage, an equation is given by [15] which allows for the calculation of the bending pressure stress over the mid-channel due to the pressure difference between the coolant and combustion chamber; the stress being highest at the mid-channel. Rearrangement of this equation allows for a design of the channel width and chamber wall thickness which minimizes failure in this manner, with proper selection of material stress

limits. An equation is also given for the calculation of the shear pressure stress, which is maximum near the interface of the channel and side wall due to the sudden change in wall thickness. Both equations are similar; the difference being a second order effect of channel width to chamber wall thickness ratio for the bending equation, and a first order effect for the shear equation. When this ratio is greater than one, the maximum pressure stress is thus in bending. When the ratio is less than one, the maximum pressure stress is in shear. Angular shear strain data is not given in [15] to use the shear equation directly.

The experiments conducted in [18] were performed with the purpose of determining the cyclic loading fatigue damage and life at the throat of three AR channel geometries, with results shown in Table 2-8. These results and the associated geometries from Table 2-2 allow optimal design ratios to be determined and selected for other engine designs.

Table 2-8: Structural results for channels tested in [18].

Configuration Number	AR at Throat	Structural Result
1	0.75	average life design; eventual material failure
2	1.50	long life design; eventual material failure
3	5.00	no failure design

Thermal loads are also a major concern for rocket engines. The scope of [16] is on the unique requirements for regeneratively cooled chambers operating at low thrusts and high chamber pressures, giving the following expected temperatures for an engine of slightly higher performance than the cSETR 50lbf engine:

a) differential between hot-wall and outer shell; strain considerations: 700 K

b) range for hot-wall, O_2 cooled: 728 K to 806 K

c) range for channel lower wall, O_2 cooled: 478 K to 533 K

The works of [15] and [22] explain that the temperature gradients caused by hot combustion gasses and cold coolant on opposite sides of the same wall, as well as between the hot-wall and outer shell, lead to shorter material life from strain effects even if the regenerative cooling process can reduce the hot-wall temperature below that of melting.

The validity of the approach of [7] to determine the thermal stress for the coaxial shell construction can not be verified with the information presented, nor using the cited equation sources of [10] and [15] as suggested. Many material and engine parameters are required with the equations of [10], basically identical for coaxial shell as well as tubular stress, and interestingly do not involve the channel width parameter reported by [7] as the result of the approach. A maximum channel width of 2.54 mm is given, but is questionable.

The results of [18] show that increasing channel AR has an effect of decreasing the hot-wall temperature significantly. The highest temperature was found to be located on the hot-wall adjacent to the channel centerline, with a temperature minimum underneath the fin structure. This 2D phenomena is confirmed by [13] and [28]. Additionally, [18] states that a further reduction of the temperature can be achieved if AR's higher than 5.0 are used. The explanation, explained in [13] and later confirmed by [8], is that the cooling channel surface area is much larger than the combustion chamber hot-wall surface area for HARCC applications, which acts to expel a higher quantity of the absorbed heat. Moreover, using HARCC to cause lower material temperatures can reduce the possibility of thermally induced plastic ratcheting. Thinning of the chamber wall adjacent to the channels, as well as the through crack failure depicted in Figure 1-8, are indicative. A doubling of the thermal cycle life was found by [6] as possible by reducing the throat hot-wall temperature from the conventional maximum of 778 K to below 667 K.

Further insight into the criteria with which to judge material failure can be gained using the limit analysis of engineering structures and indeterminate beams presented in [36]. In limit analysis, an acceptable maximum load can be ascertained for a structure which is permitted to develop a reasonable plastic deformation with only the minimum number of plastic hinges allowed before a mechanism is formed. Despite the deformation, the structure may be able to withstand greater loads before complete failure is achieved, and can be designed using those greater loads. Utilizing limit analysis allows for an elastic-limit criterion to be easily set for a preliminary stress analysis with the methods of mechanics of materials for indeterminate beams per [17]. The more difficult and involved analysis of elastic-plastic material behavior, as done by [5] and [18], can be avoided. The criterion is either the actual limit load or a bracket of it.

2.6 Using Methane as the Coolant and Fuel

The use of methane as the coolant and the fuel, with liquid oxygen as the oxidizer, in a bipropellant rocket engine system presents challenges which are not as prevalent when using other coolants, as discussed in the few literary works which actually consider methane. Furthermore, most literary works such as [6], [7], and [12] are concerned with engines with much higher thrust and chamber pressures than the cSETR 50lbf engine. Works which consider lower thrusts are [16] and [35], however [35] is a text book with focus on established techniques so does not consider methane, whereas [16] is a research study which does.

The work of [12] studies the cooling capabilities of light hydrocarbon fuels including methane for supercritical high coolant pressure operation, but involves fluorinated oxidizers. Equations and graphs are provided to calculate certain state properties of the coolant system involving enthalpy considerations, also considered in [23], which may require reformulation to

consider non-fluorinated liquid oxygen. Some conclusions as given may not fully apply to simple methane/oxygen. The cooling capabilities for methane are shown to be good for high engine thrust levels and high combustion chamber pressures, but not for low chamber pressures due to the small range of liquid operating conditions before phase change occurs. In the subcritical low pressure operation, [8] confirms that boiling phase change must be allowed for methane. For a low thrust and low chamber pressure engine such as the cSETR 50lbf engine, the phase change phenomena presents a design challenge for the typical cooling operation near the critical point seen in Figure 1-9.

Additionally, [16] determined that only a limited number of specific impulse, chamber pressure, and thrust operating points are possible with methane and oxygen. Methane as a coolant operating in the supercritical single-phase state was considered to have the following qualities in comparison to using oxygen as the coolant:

a) for thrust levels lower than 100lbf: not recommended, but oxygen capability is low
b) for combustion chamber pressures lower than 3.45×10^6 N/m^2: allowed
c) does not cause copper oxidation, in contrast to oxygen above 589 K
d) peak engine performance at oxidizer to fuel mixture ratio of 3.5 ± 0.5

The minimum allowable channel pressure drop from inlet to outlet is also given, and can be read from Figure 2-7 at the chamber pressure of the cSETR 50lbf engine as $\Delta P = 600{,}000$ N/m^2.

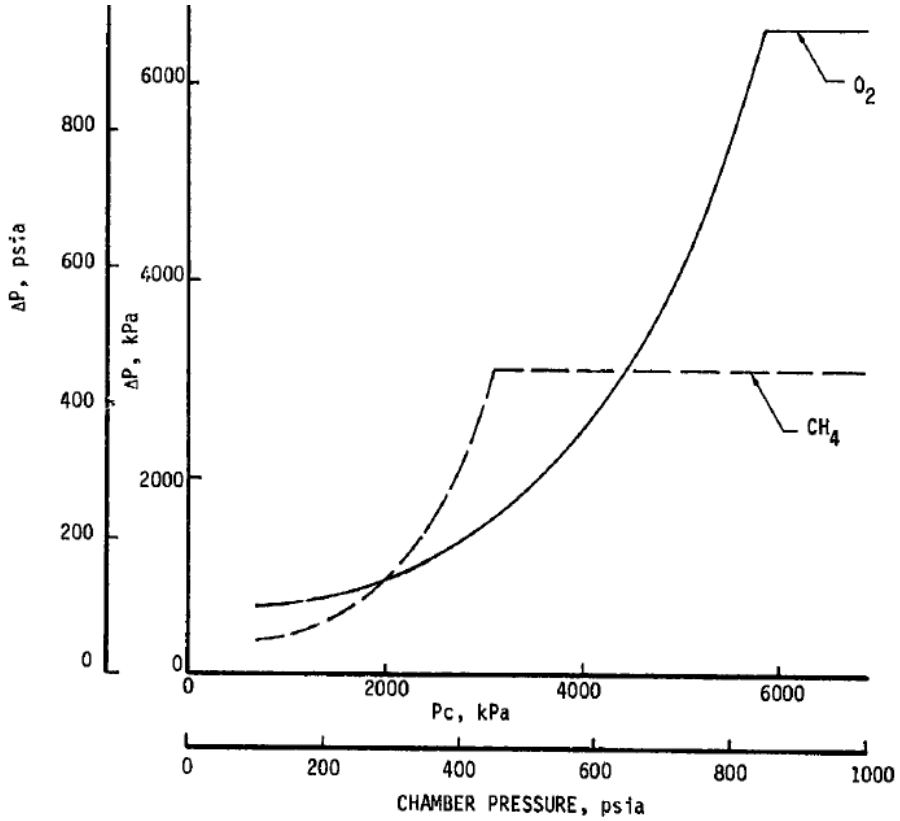

Figure 2-7: Allowable cooling channel pressure drop for O_2/CH_4 systems as a function of chamber pressure. Obtained from [16].

Decomposition of hydrocarbon fuels and the depositing of carbon atoms on the engine surfaces, "coking", is a concern at high temperatures and investigated by [12], [16], [23], and [37]. Methane in particular is not subject to decomposition, and temperature limits are usually given based on approximate failure limits for structural engine components. Values include: a range of 873.15 K to 1173.15 K (for pure methane, reducing with impurities), 978 K, and a range of 1033 K to 1367 K.

An additional limiting temperature is placed by [12] in consideration of coolant film effects, of 1036 K. Restrictions on the optimal operating pressures for methane are also given, but the values are for a much higher thrust than the cSETR 50lbf engine. A coolant inlet temperature to the channel is also suggested to be at 5.6 K above the normal freezing point for any fuel. For

methane in particular, [16] gives a typical inlet temperature of 112 K, and [7] gives the pressure and temperature conditions of Table 2-9 for an application with a feed line connecting the turbopump exit to the channel inlet. The computational models of [8], however, attempt to reproduce actual methane working conditions by using the values in Table 2-10.

Table 2-9: Pressure and temperature conditions of methane found from the analysis of [7].

Location	Pressure, [N/m^2]	Temperature, [K]
Turbopump Exit	12,996,617.4976	118.0556
Channel Inlet	12,672,563.9048	116.6667
Channel Outlet	11,514,244.6796	526.2222

Table 2-10: Pressure and temperature conditions of methane used by [8].

Property	Value
Channel Inlet Stagnation Temperature, T_0 , [K]	130
Channel Inlet Stagnation Pressure, P_0 , [N/m^2]	9×10^6
Channel Outlet Static Pressure, P, [N/m^2]	7×10^6

More temperature limits and values for methane are found in [10], [38], and [16]. An upper temperature limit of 450 K is imposed on methane for using the expander cycle to drive turbine pumps. The methane channel outlet temperature range is reported to be 328 K to 478 K, with maximum allowable bulk temperature limit of 478 K to 533 K due to rapid decrease in density. Given point property values are shown in Table 2-11.

Table 2-11: Various point property values for methane.

Property	Value	Source
Freezing Point, [K]	88.706	[10]
Boiling Point, [K]	110.928	[10], 1967
Boiling Point, [K]	112	[16], 1982
Critical Pressure, [N/m^2]	4.598×10^6	[16]
Critical Temperature, [K]	191	[16]
Dynamic Viscosity, μ, [kg/m-s]	16×10^{-6}, 473.15 K	[38]
Dynamic Viscosity, μ, [kg/m-s]	18.5×10^{-6}, 573.15 K	[38]

Knowledge of the expected combustion temperature for oxygen and methane (O_2/CH_4) at the proper mixture ratio is essential to define an important boundary condition and directly effects the design of the cooling system, but a value is not readily found in literature. To give an estimate of the typical temperatures found in combustion, although not necessarily representative of the value for O_2/CH_4, [10] and [15] provide the values for fluorine-oxygen (OF_2) oxidizer with methane fuel burning at 3977.59 K, and oxygen with hydrogen burning at 3611.11 K. An exact value is still required, which can be obtained with the suggestion of [6]. The analysis employed an ideal combustion condition with no losses, resulting in the hottest combustion gas temperature possible and a more conservative approach to the definition of cooling requirements. This suggests that the maximum adiabatic, or a suitable equilibrium, flame temperature be calculated using the methods of advanced thermodynamics based on [32] and [39]. Needed reference information found in [28] and [40] is shown in Table 2-12. Equations to calculate the needed ideal gas specific heats are in [28].

Table 2-12: Useful heats (enthalpies) of formation at 298.15 K from [28], and compound molar masses (molecular weights) from [40].

Compound	Formula	$\bar{h}°_f$, [kJ/kmol]	MM (MW), [kg/kmol]
Methane (g)	CH_4	-74,873	16.0426
Oxygen (g)	O_2	0 (diatomic molecule)	31.998
Carbon Dioxide (g)	CO_2	-393,522	44.009
Water (g)	H_2O	-241,827	18.0148
Carbon Monoxide (g)	CO	-110,530	28.01

2.7 Computational Modeling and CFD

The complex nature of three dimensional (3D) fluid flow can be modeled mathematically using low order 1D methods to gain approximate results which are often suitable for a simple flow application. As described in [41], fluid dynamics theory is based upon a combination of mathematics and experimental refinement. For regenerative cooling in particular, [42] additionally notes that a 1D analysis using Nusselt type empirical correlations is typical which provides about ±20% error. The universal character of CFD to directly model physical phenomena without adjustment correlations from experimental data is promoted.

When fluid dynamics theory is combined with computers, larger and more complex flow applications can be solved with a faster turnaround, with the added possibility of more accurate results. Before a computational fluid dynamics (CFD) computer model is built however, an understanding and application of the basic theory is required to ensure that the CFD results obtained will be reasonable.

The fundamental conservation laws of physics used to describe generalized fluid motion can be found in [41] and [43], and are very complex in their 3D form. They include conserving: mass, termed the continuity equation; linear momentum, beginning as Newton's second law of

motion; and energy, termed the first law of thermodynamics. Of particular interest are the momentum and energy equations when formulated in the proper manner. The momentum equations lead to the complex Navier-Stokes equations, which are important to describe 3D fluid flow. The energy equation gives the ability to describe heat transfer, boundary layers, and fluid turbulence. The complexity of these equations often requires many discretizations in order to obtain analytical solutions. Applying additional flow theory and equations then allows for the proper use of CFD.

An important definition when describing fluid boundary layers adjacent to solid walls is the non-dimensional distance y^+, derived and discussed in [13], [41], and [43]. The distance is sometimes termed as part of the "law of the wall" when surface roughness effects are involved, and applied to the channel fluid domain in a computational model.

As explained in [41], applying the y^+ concept to CFD allows a computationally efficient method to discretize a fluid domain next to a wall boundary into a computational mesh. A formula in terms of y^+ is given to calculate the nearest mesh grid point actual distance from the wall. Adhering to the absolute minimum criteria that $y^+ > 11.63$ ensures that the mesh is not prohibitively dense, since resolving all the details in a turbulent boundary layer are usually not necessary. The result would be extremely long computational times with little added benefit, as seen in [44]. The discussion of CFD solution stability analysis in [45] from a purely mathematical standpoint leads to the understanding that using excessively small meshes, with y^+ below the absolute minimum criteria, may create the situation of stiff mathematical matrices which are difficult to solve. The usage of y^+ by [8] is not detailed and the value used "of order 1" is questionable.

Various references give preferred ranges for designing the near-wall mesh such that the y^+

value falls within the fully turbulent region of the boundary layer on a smooth wall, shown in Table 2-13. Still adhering to the absolute minimum y^+ criteria, [3], [33], [41], [44], and [46] describe a grid refinement mesh sensitivity investigation for improving the accuracy of any particular CFD application.

Table 2-13: Preferred smooth wall y^+ ranges of various references.

Reference	Ranges	Reference Note
[41]	$30 < y^+ < 500$	
[44]	$22 < y^+ < 100$	gives best results
[43]	$70 < y^+ < 400$	
[47] and [48]	$30 < y^+ < 300$	preferably near the lower bound
[13]	$y^+ > 60$	fully turbulent region
[49]	$y^+ > 30$	fully turbulent region

With the adherence to the y^+ criteria and ranges, the "wall function approach" is then used to represent the effect of the wall boundaries with additional "wall function" equations. Details and various treatments are given in [41], [47], and [48]. The "standard wall functions" are applicable to the y^+ ranges of Table 2-13. The handling of near-wall bounded turbulent flows is linked to the manner by which the flow turbulent viscosity is modeled.

Changes in the turbulent kinetic energy, "k", and turbulent dissipation rate, "ε", of fluid and computational flows is explained in [41] and [47] through the use of mathematical turbulence models. Minor variations on the classic two equation realizable "k-ε model" with standard wall functions are widely used in literature and only valid for the fully turbulent region, per [3], [44], and [49]. However, the more complex seven equation linear pressure-strain "Reynolds Stress Model" is explained as more general and potentially very accurate. The choice between the two is not clear and must be investigated through a turbulence sensitivity study.

The work of [41] states that distributions of the k and ε values must be defined as boundary

conditions to the turbulence models at the inlet of internal flows. Equations to calculate crude approximations of these values are given, equivalent to those in [47], and require a length scale and turbulence intensity factor. Suggested values for intensity are given by various references, shown in Table 2-14. Rough-guess inlet values for k and ε are shown by [46] which can be used for comparison purposes only: $k = 0.09\ m^2/s^2$, $\varepsilon = 16\ m^2/s^3$. But, the results should not be sensitive to these inlet values because most of the turbulence is generated in the internal flow boundary layers downstream.

Table 2-14: Suggestions for turbulence intensity factor of various references.

Reference	T_i , or as I	Reference Note
[41]	1% to 6 %	typical values
[44]	5%	for a combustion chamber
[47]	I < 1%	"low", used if the upstream flow is under-developed and undisturbed
[47]	1% < I < 10%	"medium", used if the upstream flow is fully developed
[47]	I > 10%	"high"

The use of the Bartz equation for the combustion gas side heat transfer coefficient has been explained to give the variation required along the hot-wall when using a computational model of straight channels with no curvature. A computational model can thus relate to the experimental method of [18] which uses straight channels in a plug-nozzle engine design where the combustion chamber is formed from a cylinder, with a water cooled center body inserted which has the curvature. The location of minimum distance between the cylinder and the center body as seen in cross section creates the throat. Viewing the Bartz equation, the mathematical representation of this chamber geometry is the same as a typical cone nozzle. Flow curvature

effects in the HARCC were not determined in [18] or the computational models of [8], suggesting that temperature effects can be investigated before curvature effects are included.

For physical internal channel flow, [13], [29], and [31] describe a non-steady-state entrance length upstream of the thermally and hydrodynamically fully developed region. For computational internal channel flow, [22] and [41] describe an adiabatic flow entrance length upstream of the heated channel section to be investigated. A length of ten times the heat transfer section length is found, but the equations are more useful. The work of [14] prefers unspecified "sufficient" entry lengths instead of a calculation.

The entrance length concept involves the addition of extra channel length upstream of the inlet to the flow area of interest, for the purpose of allowing the flow to become hydrodynamically fully developed in an adiabatic manner prior to the flow area of interest. A new inlet is created upstream of the original inlet for experimental work. In CFD simulations, the new inlet is the CFD inlet, and the original inlet becomes a simple measured distance downstream of the CFD inlet to denote the location of the beginning to the flow area of interest. Adding the entrance length to a CFD model allows for a numerically pre-developed flow. Related to the regenerative cooling channel concept, the CFD inlet can be thought of as the inlet to the feedline which pipes the coolant to the cooling channel inlet. The cooling channel inlet is thus the beginning to the flow area of interest, and where the adiabatic portion ends and heat addition begins.

Various computer codes are available to model fluid dynamics and heat transfer. The work of [16] modifies the ALRC SCALER thermal design computer program into the 1981 form called SCALEF, and gives some of the program details. The program uses 1D heat transfer theory involving a form of the Dittus-Boelter equation to calculate the hot-gas side heat transfer

coefficient. The equation is given in generalized form by [13] and [29], but for applying on the coolant side.

Many researchers use the two related computer codes RTE and TDK, for example [3], [6], and [23]. RTE is a 3D thermal evaluation code for rocket combustion chambers, while TDK is a 2D non-equilibrium nozzle analysis and performance code. Other codes and subroutines, like the ROCCID rocket combustion injector analysis code, are possible for implementation. Despite being specific to cooling channels and rocket engines, the codes as written have limitations like assuming a uniform cross sectional temperature in the HARCC in contrast to references in [6] and the results of [8], [33], and [50]. Still, the theory used in the codes relevant to rocket engines can be a valuable resource for comparing or beginning a more generalized CFD software simulation that overcomes the limitations.

Many researchers, for instance [7], [8], [14], [49], and [50], chose to write their own computer codes based on 1D heat transfer theory. Some implement other resources for fluid and combustion properties, like the NIST chemistry web-book, the NASA Thermochemistry code, or the NASA Chemical Equilibrium Analysis (CEA) program. Then, the computational results obtained in that manner may be compared to multiple ANSYS CFD computer models in 2D for separate solid and fluid regions, but not in a 3D integrated manner.

At the beginning of a design, it may be sufficient to consider only steady-state effects and conditions. This was the focus of the experimental work of [18] and the computational work of [3]. To add flexibility, generalized CFD software can also be used to obtain transient results if needed at a later time.

The commercially available CFD software ANSYS FLUENT, now up to version 12.1, has been widely used for many applications. It is mentioned in [41] and used by [3], [33], [42], [44],

and [46]. Additionally, [42] uses two separate software, Advance/FrontFlow/red and CRUNCH CFD, for comparison of results. The extensive details of the FLUENT software are given in the documentation of [47], [48], and [51] showing that the underlying theories of heat transfer and fluid flow from many other references are implemented using the finite volume approach. Information is given in terms of proper utilization of CFD discretizations, as well as solution strategies for complex models. One particular strategy is to start the simulation at a low order discretization, then switch to a higher order for increased solution accuracy. With the proper application of boundary conditions and settings, the FLUENT software can be used for generalized problems involving ideal or real gasses, steady state or transient solutions, fluid flow, heat transfer, turbulence, solids, and with the "interface" method a coupled simulation involving fluids together with solids using the additional information from [52]. A thorough understanding of the governing equations is necessary for proper utilization of the software and confidence in the results. Some limitations of FLUENT are found through experience: certain licenses are limited to the use of 512,000 total mesh cells which limits mesh density, and the software prefers flows in the positive x axis direction though not required. Of particular interest in [48] is the statement that the value of y^+ is not a fixed geometric quantity but is solution dependent, and therefore should be adjusted by performing a mesh & turbulence sensitivity study prior to the main simulations. Using the methods above for determining y^+ does however allow an initial mesh to be determined.

Turbulence model application in FLUENT is given detail in the documentation, noting that the "realizable" k-ε model has substantially better performance than the "standard" version. There is a slight disparity between the documentation and the software with which of the default model constants of Table 2-15 are used and able to be adjusted, noted in the table. Default

solution control factors, as well as under- and explicit-relaxation factors, as used in FLUENT are given in Table 2-16.

FLUENT also supplies an extensive built-in Material Property Database which can be adjusted to the user's specific application. The useful quantities are given in Table 2-17.

Table 2-15: FLUENT turbulence model default constants and suggestions, per [47], [48], [51]. Note: values include standard wall functions and viscous heating.

Parameter	realizable k-ε model	Note for k-ε	linear pressure-strain Reynolds Stress Model	Note for RSM
C_μ			0.09	
$C_{1\varepsilon}$	1.44	shown in equations in [47] and [51] but not in software	1.44	
$C_{2\varepsilon}$	1.9	given as "C_2" in [47] and [51]	1.92	
Pressure Strain C_1-PS			1.8	
Pressure Strain C_2-PS			0.6	
Pressure Strain C'_1-PS			0.5	
Pressure Strain C'_2-PS			0.3	
TKE Prandtl Number, σ_k	1.0		1.0	value is 0.82 in [47] and [51] but 1.0 in software
TDE Prandtl Number, σ_ε	1.2		1.3	value is 1.0 in [47] and [51] but 1.3 in software
Energy Prandtl Number, Pr_t	0.85		0.85	
Wall Prandtl Number	0.85		0.85	
Full Convergence Criteria Required	10^{-6}		10^{-4}	

Table 2-16: FLUENT default solution control, under-, and explicit-relaxation factors, per [47], [48], and [51].

Factor	Value	Reference Note
Courant (CFL) Number	200	may need 20 to 50 for complex 3D cases, per [51]
Momentum	0.75	may need ~0.5, per [48]
Pressure	0.75	may need ~0.2, per [48]
Density	1	may need <1.0, per [48]
Body Forces	1	
Turbulent Kinetic Energy, k	0.8	may need ~0.5, per [48]
Turbulent Dissipation Rate, ε	0.8	may need ~0.5, per [48]
Turbulent Viscosity	1	
Reynolds Stresses (RSM only)	0.5	
Energy	1	may need <1.0, per [48]

Table 2-17: Useful FLUENT Material Property Database values, from the software interface and through [48] referenced files.

Property	Methane, CH_4	Nickel, Ni	Copper, Cu	Air
Density, ρ , [kg/m^3]	0.6679	8900	8978	1.225
Specific Heat, Cp, [J/kg-K]	2222	460.6	381	1006.43
Thermal Conductivity, λ, [W/m-K]	0.0332	91.74	387.6	0.0242
Dynamic Viscosity, μ, [kg/m-s]	1.087×10^{-5}			
Molar Mass / Molecular Weight, MM, [kg/kgmol]	16.04303			
Reference Temperature, [K]	298.15			~298.15
Critical Temperature, [K]	190.56	9460		
Critical Pressure, [Pascal = N/m^2]	4599000	1.08×10^9		
Critical Specific Volume, [m^3/kg]	0.006146	0.000391		

Prior to using the FLUENT CFD software, an additional piece of software is required to create the geometry and mesh. The software GAMBIT has been used, particularly by [3], mainly because it was packaged with older versions of FLUENT. The software Altair HyperMesh is a useful choice as it provides the functionality to organize 3D features in specific ways which are required by FLUENT. Some important limitations of HyperMesh are found through experience: can only handle three decimal places, can only allow eleven characters total in a type-in box, and can not handle placement of nodes closer than about one half millimeter. Due to the values possible for insertion, this limits the overall significant figures to a maximum of six.

2.8 Ideal Versus Real Gas Modeling

The wide variation possible in the state properties of a fluid presents challenges in the calculation of property behavior undergoing any process. Simplifications are often made and utilized for approximate results from the real gas behavior toward an ideal gas solution. For the most accurate results, a real gas solution is desired but is not always available. In the field of computational fluid modeling, additional challenges arise from the implementation of the real gas models.

The complex real gas fluid behavior is introduced in [10], [12], and [13] as it relates to heat transfer. The process of nucleate and film boiling phase change, and its effect on the heat transfer behavior of a coolant, is examined mainly from an experimental standpoint. Little information is given for the calculation of the behavior without requiring experimental data. Such experimental data is not typically available prior to a numerical simulation as the purpose of numerical simulations is to obtain the preliminary results. Multiple numerical simulations are thus required with a range of adjustments to the mathematical model, for experimental validation

later. The two heat transfer coefficient equations mentioned previously, the Sieder-Tate and vapor-film equations, are the only tools available in [10] to model the real behavior of a coolant. These equations require the user to assume or otherwise determine the fluid behavior beforehand with the purpose of choosing which equation to use, or require both equations to be used for later validation.

Cryogenic hydrogen is a typical fuel used in bipropellant rocket engines due to its well behaved thermodynamic behavior during engine operation, and investigated in many works including [8], [10], [12], [14], [15], [18], [23], [33], and [49]. The state property transition for hydrogen is solely in the supercritical region where the pressure is far from the critical point on a pressure-temperature state diagram, as explained in [8]. Figure 1-9 shows that the state property transition for methane during typical regenerative cooling operation is much closer to its critical point in the transcritical region where phase change is a likely possibility. This adds to the complexity involved in the design, use, and optimization of the channels, as well as the computational modeling of the methane coolant behavior. The work of [8] goes as far as utilizing a specialty made CFD code in an attempt to overcome the real behavior limitations of more general software.

Various modeling options are available in the generalized FLUENT CFD software to represent the behavior of both ideal and real gasses, described in [47], [48], and [51]. The computational complexity and expense increases when moving from the relatively simple ideal gas model to other more complicated models, noted by [49], peaking at any real gas model due to the increased number of terms in the equations. The real gas behavior is desired for optimizing a channel design, however one may not be easily available for implementation in the computational model chosen. For instance, the phase change which is likely to occur with

methane, as seen in Figure 1-9 and suggested by [34], does not allow the use of the standard built-in FLUENT real gas modeling techniques and would require a user-defined model.

Despite the real gas software limitation of FLUENT, the well known ideal gas equation can be used to give preliminary and estimated results of the real gas behavior for later comparison. Ideal versus real behavior was investigated by [50] for instance, showing that the real behavior dominates along much of the channel and should not be ignored. This is particularly true for methane based on the analyses of [12] and [23], and enthalpy/energy techniques have been used.

2.9 The cSETR 50lbf Thrust Engine

Geometry and operating parameters for the cSETR designed 50lbf engine of Figure 1-10 were obtained from [9], described by [11] as a conical type nozzle engine integrated with the combustion chamber as one piece. The effects of the wall contour on the cooling properties or channel flow characteristics may be strong due to the small radius of curvature and sharp angle of attachment with the chamber. Modeling straight channels with no curvature or angle is possible with the Bartz equation, mentioned previously, if the true cooling channel length along the curved surface of the combustion chamber wall, a "corrected" length rather than the axially projected length, is used.

The fuel feed system for the cSETR 50lbf engine is not currently finalized, but [11] suggests pump instead of pressure feeding for regenerative cooling due to the increased propellant tank pressure required to overcome the channel pressure drop in a pressure fed system. The increased pressure requirement also increases the structural weight of the tank, which is not favored. The work of [16] examines various engine cycles and feeding system methods, which should be analyzed for the proper choice involving methane with the help of [35]. The expander cycle

using pump feeding is possible with the chamber pressure of the cSETR 50lbf engine.

Geometric and operating parameters required for designing the regenerative cooling system of the cSETR 50lbf engine are given in Table 2-18.

Table 2-18: Various cSETR 50lbf thrust engine geometric and operating parameters, from [9] and using Figure 1-10.

Parameter	Value
total mass flow rate of coolant/fuel methane, $\dot{m}_f$, [kg/s]	0.018
total mass flow rate of oxidizer oxygen, $\dot{m}_o$, [kg/s]	0.0575
combustion chamber pressure, p_c , [N/m^2]	1.5 x 10^6
diameter of combustion chamber, d_c , [mm]	32.5
radius of combustion chamber, r_{cc} , [m]	0.01625
diameter of throat on inner surface, d_t , [mm]	10.3
radius of throat on inner surface, r_t , [m]	0.00515
radius of curvature at throat, r_{ct} , [m]	0.0051
approximate mixture ratio of oxygen to fuel	3.2
combustion flame temperature, [K]	3533.15
true cooling channel length along curved surface, [m]	0.1562488

CHAPTER 3

MATHEMATICAL THEORY OF REGENERATIVE COOLING

This chapter presents the mathematical theory required for the design and optimization of regenerative cooling passages to be used for rocket engine applications, as used in the present research. The basic theory behind the required equations is given when available to indicate the origins and limitations. The chapter outline and section layout used previously is closely followed for convenience due to the many theoretical aspects considered. Additional detail for equations and theory which are related but not directly manipulated in the present research may be found in the references discussed in the literature review.

3.1 Cooling Channel Pressure Relationships

Certain pressure limitations must be adhered to for the proper operation of regenerative cooling channels. To prevent backflow into the channels, the pressure of the coolant when it reaches the combustion chamber must be larger than the combustion pressure. The combustion pressure thus represents the minimum allowable coolant pressure.

When the injector pressure drop is considered, the minimum allowable channel outlet pressure can be calculated using:

$$P_{out\,\min} = p_c + P_{drop} \tag{1}$$

where: p_c = combustion chamber pressure, [N/m^2],

P_{drop} = minimum allowable pressure drop across the injector, [N/m^2].

Options for determining the injector pressure drop are given by [10] and [16]:

$$P_{drop} = p_c^{0.75} \ , \tag{2}$$

or,

$$P_{drop} = 0.2\, p_c \ . \tag{3}$$

Alternately, [12] gives a direct equation to calculate the minimum allowable channel outlet pressure:

$$P_{out\,\min} = 2\, p_c \ . \tag{4}$$

Three values for the minimum allowable channel outlet pressure are available for consideration.

The channel itself also contributes a pressure drop to the coolant. Upstream, the minimum allowable channel inlet pressure can be calculated by adding the channel pressure drop, ΔP, to the minimum outlet value in a similar fashion:

$$P_{in\,\min} = P_{out\,\min} + \Delta P \ . \tag{5}$$

Quick estimation of ΔP can be performed without an equation if adequate literature reference information is provided.

3.2 Theory of Cooling System Heat Transfer

The theory used to describe a regenerative cooling system can be divided into separate control volumes of the basic heat transfer theory and discussed separately. This is possible mainly due to the use of CFD software which couples the equations automatically. The separate control volumes allow for various definitions of CFD boundary conditions, and simplifies the task.

3.2.1 Basic Heat Transfer Theory

The basic equations for heat flux form the fundamentals of the heat transfer theory required to describe regenerative cooling. In the equations, the coefficient terms are the most important and usually difficult to define for a generalized system, but take focus for mathematical simulations. Figure 2-6 and the information in [28] can be used to describe the theory.

The convective heat transfer rate at the fluid-solid interface of the combustion chamber gasses and hot-wall is described by the heat flux equation in the form:

$$\dot{q}_{hw} = h_g \left(T_{0g} - T_{wh} \right) \tag{6}$$

where: h_g = hot-gas heat transfer film coefficient on the hot-wall, [W/m^2-K],

T_{0g} = stagnation (total) temperature of the free stream combustion gasses, used with little loss of accuracy from the more accurate adiabatic wall recovery temperature T_{aw} in Figure 2-6, [K],

$T_{wh} = T_{gw}$ of Figure 1-6 = T_{wg} of Figure 2-6 = hot-wall temperature, [K].

Definition of the hot-gas heat transfer film coefficient, h_g , is required to describe the gas side heat transfer.

The conductive heat transfer through a solid wall is given by the 1D heat flux equation in the form:

$$\dot{q}_w = \frac{\lambda_w}{\Delta L} \left(T_{wh} - T_{wc} \right) \tag{7}$$

where: λ_w = thermal conductivity of the wall material, [W/m-K],

ΔL = wall thickness, [m],

T_{wc} = wall temperature of the colder surface, [K].

Knowledge of the material gives the thermal conductivity. The application of this equation can

occur in multiple locations of the cooling channel cross section, as well as with extended fin surfaces. Solid-to-solid heat transfer is accomplished when two solids adjoin at an interface and the heat flux exiting one material equals that entering the other, with an equal temperature value at a firmly joined interface.

The convective heat transfer rate at the solid-fluid interface of the chamber wall, or fin, and cooling fluid is described by an equation of the same form as Equation (6):

$$\dot{q}_c = \alpha_g \left(T_{wc} - T_{co} \right) \tag{8}$$

where: α_g = convective heat transfer coefficient on the channel wall, [W/m^2-K],

T_{co} = temperature of the free stream coolant, as in Figure 2-6, [K].

Definition of the channel heat transfer coefficient, α_g, is essential to design the extended fin surfaces located between each channel passage.

Certain term groupings are often seen and analyzed. Just as the Nusselt number (Nu) describes heat transfer into a fluid enclosed within a passage by relating the heat transfer coefficient α_g with the properties of the passage, [13] describes the heat transfer from a wall into the fluid and relates α_g with the properties of the wall through the use of the Biot number (Bi). Comparing the two numbers, heat transfer can be increased by the adjustment of certain parameters to increase Nu and Bi as much as possible:

a) $Nu = \dfrac{\alpha_g D}{\lambda_b}$

1) increase the heat transfer coefficient
2) increase passage diameter or hydraulic diameter, *D*, which in effect increases the surface area

3) decrease the thermal conductivity of the coolant, λ_b

4) for a specific fluid, λ_b is fixed for ideal conditions, so α_g and *D* should be as large as practical

b) $Bi = \frac{\alpha_g L_o}{\lambda_f}$

1) increase α_g; which is the same α_g value as for Nu

2) increase wall thickness, L_o, to allow for better conduction

3) decrease the thermal conductivity of the wall material, λ_f

4) for a specified wall material, λ_f is fixed, so α_g and L_o should be as large as practical

In effect, the heat transfer coefficient is a function of the wall surface area, and shows the advantage of HARCC. The high value for α_g leads to a thin thermal boundary layer and indicates good heat transfer, while a small α_g leads to a thick layer and bad heat transfer. HARCC increases the surface area over which a thin boundary layer can exist and operate.

The external radiation properties of real bodies are based on the Stefan-Boltzmann Law. The radiation heat flux equation uses terms that are easily defined and do not require extensive sub-calculation as is the case for the convective heat transfer coefficients h_g and α_g. The form of the equation most useful to later CFD application is per [48]:

$$\dot{q}_r = \varepsilon_{ext}\, \sigma_{SB} \left(T_\infty^4 - T_w^4 \right) \tag{9}$$

where: ε_{ext} = emissivity of the external wall surface, a material property,

σ_{SB} = 5.670 x 10^{-8} = Stefan-Boltzmann constant, [W/m^2-K^4],

T_∞ = temperature of the radiation sink on the exterior of the domain, [K],

T_w = surface temperature of the wall, [K].

3.2.2 Gas Side Heat Transfer

The convective coefficient required to describe the heat transfer on the combustion chamber hot-wall must take into account the variation in combustion gas properties as they travel in the combustion chamber, past the throat, and out the nozzle. When combined with Equation (6), a peak in heat flux at the throat must be seen, according to many literature sources. The Bartz equation, mainly a function of the local cross sectional area, accomplishes the required behavior:

$$h_g = \left[\frac{0.026}{(D^*)^{0.2}} \left(\frac{\mu^{0.2} c_p}{\mathrm{Pr}^{0.6}} \right)_0 \left(\frac{p_0}{c^*} \right)^{0.8} \left(\frac{D^*}{r_{ct}} \right)^{0.1} \right] \left(\frac{A^*}{A} \right)^{0.9} \sigma \text{ , [W/m}^2\text{-K].} \qquad (10)$$

The correction factor for property variations across the boundary layer is given by:

$$\sigma = \frac{1}{\left[\frac{1}{2} \frac{T_{wh}}{T_{0g}} \left(1 + \frac{\gamma - 1}{2} M^2 \right) + \frac{1}{2} \right]^{0.8 - 0.2\omega} \left(1 + \frac{\gamma - 1}{2} M^2 \right)^{0.2\omega}} . \qquad (11)$$

The known terms of Equations (10) and (11) are:

D^* = engine throat diameter of the inner surface, [m],

$p_0 = p_c$ = stagnation (total) pressure of the combustion chamber at the location of the nozzle inlet, [N/m^2],

r_{ct} = radius of curvature of nozzle contour at throat along centerline axis, [m],

$A^* = \left(\frac{\pi}{4} \right) (D^*)^2$ = cross sectional flow area at throat, [m^2],

$A = \left(\frac{\pi}{4}\right)(d)^2$ = axial flow chamber inner surface cross sectional area at a local value of the inner diameter *d*; area under consideration along chamber axis; varies with position from the injector, to the combustion chamber, to the throat, to the nozzle exit along the engine centerline axis; the ratio of the local area to the throat area in Figure 2-5 is formed by $\xi = \left(\frac{A}{A^*}\right)$; [$m^2$],

ω = exponent of viscosity-temperature relation; $\omega = 0.6$ for diatomic gasses and gives the values for σ plotted in Figure 2-5, allowing graphical determination of σ rather than direct calculation,

$c^* = \frac{p_0 A^*}{\dot{m}_{sys}}$ = characteristic velocity, [m/s],

$\dot{m}_{sys} = \dot{m}_{fuel} + \dot{m}_{oxidizer}$ = propellant consumption steady mass flow rate, [kg/s],

$T_{wh} = T_{wg}$ of Figure 2-5 = hot-wall temperature, can use an assumed average reference value from literature, [K],

$T_{0g} = (T_c)_{ns}$ of Figure 2-5 = nozzle stagnation inlet temperature, or chamber total temperature, of the free stream, [K],

$\left(\frac{T_{wh}}{T_{0g}}\right) = \left(\frac{T_{wg}}{(T_c)_{ns}}\right)$, knowledge of this ratio allows the graphical determination of σ from Figure 2-5,

γ = specific heat ratio of the combustion mixture prior to the reaction.

Methods of advanced thermodynamics per [31] and [32] can be used to determine some of these quantities. The chamber total temperature, T_{0g}, can be found from a calculation of the adiabatic flame temperature of the combustion components for the particular oxidizer and fuel

used in the engine. The specific heat ratio of the combustion mixture prior to the reaction, γ, is found by taking the average weighted sum of the partial molar fraction of individual reactant specific heat ratios, using the reaction equation coefficients:

$$\gamma_{mixture} = \gamma_{avg} = \frac{\sum_i n_i \gamma_i}{\sum_i n_i} \quad . \tag{12}$$

Interpolation is necessary when extracting values from Figure 2-5 for σ between the plotted curves, performed by the linear equation with terms defined in Figure 3-1:

$$y = y_0 + (x - x_0)\left(\frac{y_1 - y_0}{x_1 - x_0}\right) . \tag{13}$$

For example if the required $\gamma_{mixture}$ is not exactly a value as shown, the subscript 0 terms would be the pair of values from one curve of γ to give the lower bound of σ, while the subscript 1 terms are from an adjacent curve giving the upper bound.

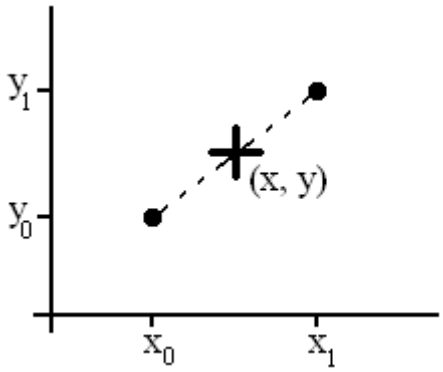

Figure 3-1: Linear interpolation terms of Equation (13).

The unknown terms of Equations (10) and (11) are:

M = local Mach number variation along the nozzle,

Pr_0 = Prandtl number of the combustion gasses, stagnation conditions,

μ_0 = dynamic viscosity of the combustion gasses, stagnation conditions, [kg/m-s],

$c_{p\,0}$ = specific heat of the combustion gasses, stagnation conditions, [J/kg-K].

A reconciliation of the unknown terms can be done using the equations provided in [10] and [31] for approximate results. For the Prandtl number:

$$\mathrm{Pr} = \frac{4\gamma}{9\gamma - 5} \tag{14}$$

where $\gamma = \gamma_{mixture}$ from Equation (12). For the dynamic viscosity, a unit conversion is necessary to evaluate:

$$\mu_0 = \left(46.6\times10^{-10}\right) MW^{0.5}\, T^{0.6} \text{ , [lb/in-sec]} \tag{15}$$

where: MW = molecular weight (molar mass) of combustion products, [lb/mol],

T = temperature of the gas mixture, [R],

the required units are [kg/m-s].

The combustion gas specific heat is obtained with:

$$c_{p\,0} = \frac{\gamma R}{\gamma - 1} \text{ , [J/kg-K]} \tag{16}$$

where the specific gas constant of the combustion gas products is calculated from:

$$R = \frac{R_U}{MW} \tag{17}$$

and: R_U = 8.314 = universal gas constant, [kJ/kmol-K],

MW = molecular weight (molar mass) of combustion products (representative values seen in Table 2-12), [kg/kmol].

All of the terms in the Bartz equation are defined, and the heat transfer coefficient variation along the wall in the centerline axial direction is able to be determined using the contour

variation of an engine cross sectional geometry.

3.2.3 Coolant Side, and Solid to Solid, Heat Transfer

The extended surfaces theory of [13] begins with the 1D steady state heat conduction in a rod that allows heat to be released from the outer surface. The rod tip is assumed insulated, so that it does not allow heat to be released. The rod material is homogeneous, surrounded by a fluid at constant temperature. The heat transfer at the rod surface is assumed constant, though generally not true. A 3D image is formed by adding a depth and a thickness to the rod, but maintaining the 1D effect of the temperature only changing along the length of the rod. With the length of the rod defined as the height, and thickness as the width, a fin of rectangular profile is created. For the most beneficial fin effect, the heat flow released from the fin surface area, excluding the insulated tip, into the surrounding coolant should be as large as possible. The maximized energy balance of heat flow entering the fin at the base and exiting through the surface results in a criteria which determines the optimal fin height based on material and flow conditions:

$$h = 1.4192 \sqrt{\frac{2\alpha_f}{\lambda_f \delta_f}} \tag{18}$$

where: h = fin height from base to tip, [m],

α_f = constant convective heat transfer coefficient at the fin surface, [W/m^2-K],

λ_f = constant thermal conductivity of the fin material, [W/m-K],

δ_f = fin width, constant from base to tip, [m].

As the heat released from the fin tip is required for proper CFD boundary conditions, a mathematical adjustment is necessary. The h in Equation (18) is replaced with a corrected fin

height, which contains the originally defined fin height, and an incremental height that provides the surface area required to release the same amount of heat as would be released at the tip:

$$h_c = h + \Delta h = h + \frac{\delta_f}{2} \tag{19}$$

where: h_c = corrected fin height, [m],

$\Delta h = \frac{\delta_f}{2}$ = incremental height addition, [m].

By assuming that the surface area of the fins is much larger than the surface area of the ground between any two fins, $A_f >> A_g$, then the convective heat transfer coefficient at the fin surface is assumed approximately equal to that at the ground, $\alpha_f \approx \alpha_g$. Combining and rearranging, the equation for the fin height becomes:

$$h = 1.4192\left(\delta_f\right)^{1/2}\left(\frac{2\alpha_g}{\lambda_f}\right)^{-1/2} - \frac{\delta_f}{2} \ . \tag{20}$$

Various options are available for determining the convective heat transfer coefficient required. The first is the film coefficient of [28], applicable to the coolant side heat transfer in a tube or channel:

$$\alpha_{g1} = 0.023\, G\, c_p \left(\frac{G\,D}{\mu_b}\right)^{-0.2}\left(\frac{\mu\, c_p}{\lambda}\right)_b^{-0.67} \text{, [W/m}^2\text{-K]}, \tag{21}$$

where: μ_b = dynamic viscosity of coolant, [kg/m-s],

$c_{p\,b}$ = specific heat of coolant, [J/kg-K],

λ_b = thermal conductivity of coolant, [W/m-K],

subscript b = quantity is evaluated at bulk mean temperature of coolant.

Equation (21) contains the following three relationships. The hydraulic diameter for a

rectangular channel is given by:

$$D = \frac{4A}{P} = \frac{2wh}{w+h} \text{ , [m],} \tag{22}$$

where: A = channel cross sectional area, [m^2],

P = channel perimeter, [m],

w = channel width, [m],

h = channel height, [m].

The average mass flow per unit area is given by:

$$G = \overline{\rho u} = \frac{4\dot{m}_c}{\pi D^2} = \left(\frac{4}{\pi}\right)\dot{m}_c\left(\frac{2wh}{w+h}\right)^{-2} \text{ , [kg/m}^2\text{-s],} \tag{23}$$

where: ρ = coolant density, [kg/m^3],

u = coolant velocity, [m/s],

overbar indicates the average of the quantity over a domain.

The mass flow rate per cooling channel is given by:

$$\dot{m}_c = \frac{\dot{m}_t}{n_c} \text{ , [kg/s],} \tag{24}$$

where: $\dot{m}_t = \dot{m}_{fuel}$ = total coolant mass flow rate of the cooling system, [kg/s],

n_c = total number of cooling channels about the engine circumference.

Also, the circumferential length can be matched to a linear representation of the length used for all of the channels by the relationship:

$$2\pi r_o \approx n_c\left(\delta_f + w\right) \tag{25}$$

where: r_o = throat radius to the outer chamber wall surface (bottom of cooling channel).

The second option for determining the convective heat transfer coefficient required is the

Sieder-Tate relationship version of [10], in the form of a Nusselt number, using suggestions from literature:

$$Nu = C_1 \,\mathrm{Re}^{0.8}\,\mathrm{Pr}^{0.4}\left(\frac{\mu_b}{\mu_w}\right)^{0.14} \tag{26}$$

where: $Nu = \dfrac{\alpha_{g2}\, D}{\lambda_b}$ = Nusselt number,

$C_1 = 0.023$ = constant depending on coolant, per [13], [29], [35],

$\mathrm{Re} = \dfrac{\rho u D}{\mu_b}$ = Reynolds number,

$\mathrm{Pr} = \dfrac{\mu_b c_p}{\lambda_b}$ = Prandtl number,

μ_w = coolant dynamic viscosity at coolant-side wall temperature, [kg/m-s],

equation is valid for: $0.5 < \mathrm{Pr} < 120$, $10^4 < \mathrm{Re} < 10^5$, L/D ~ 60.

The third option for determining the convective heat transfer coefficient required is the Sieder-Tate relationship version of [7]:

$$Nu = \frac{\alpha_{g3}\, D}{\lambda_b} = 0.027\,\mathrm{Re}^{0.8}\,\mathrm{Pr}^{1/3}\left(\frac{\mu_b}{\mu_w}\right)^{0.14}. \tag{27}$$

The forth option is brought to account for the similarity between the second, Equation (26), and the third, Equation (27). The film coefficient from [28] of the first option, Equation (21), can be compared to the vapor-film boundary layer heat transfer coefficient of [10]:

$$\alpha_{g4} = 0.029\, c_p\, \mu_b^{0.2}\,\mathrm{Pr}^{-2/3}\left(\frac{G^{0.8}}{D^{0.2}}\right)\left(\frac{T_{co}}{T_{wc}}\right)^{0.55}, \text{ [W/m}^2\text{-K]}, \tag{28}$$

where: T_{co} = coolant bulk temperature, [K],

T_{wc} = coolant-side wall temperature, [K].

It should not be surprising that four equations were found which determine the convective heat transfer coefficient, as [28] suggests only minor refinements to the same underlying theory result in the various options reported in literature, and all equations are tied together through the Nusselt number. For example, [35] gives an equation that does not contain any refinement/correction terms. The above equations should thus give similar results, but which particular equation gives the most accurate results is not clearly stated in the literature which is why their results must be compared numerically. However, Equation (21) from [28] couples the underlying theory with experimental knowledge involving tubes with an explicitly given hydraulic diameter conversion to rectangular channels. Equation (21) can then be assumed to give the most useful values with the highest degree of certainty over the other equations, due to insufficient information presented in [7], [10], [13], [29], and [35].

The coolant dynamic viscosity at the elevated coolant-side wall temperature can be determined through Sutherland's Equation:

$$\mu = \frac{C_2 T^{3/2}}{T + S} \tag{29}$$

where: μ = dynamic viscosity [kg/m-s] at temperature T [K],

C_2 = Sutherland Equation constant,

S = Sutherland Equation constant.

The constants can be determined using two different dynamic viscosities at two different temperatures in tabulated reference data for a particular coolant. Knowing the constants then allows the desired dynamic viscosity to be calculated at the desired temperature.

3.2.4 Outer Shell Heat Transfer

Heat transfer from the outer shell must be considered in experimental and CFD cases where, in contrast to [7] and cooling fin theory which assume an adiabatic fin tip, all energy transferred across the chamber wall is not absorbed by the coolant in an idealized situation. The tip of the cooling fin adjoins the bottom of the outer shell and allows for a solid-to-solid heat transfer mechanism. The temperature differential between the coolant and the engine exterior also promotes the transfer of heat through the outer shell. For exterior temperatures likely much lower than the combustion temperature, heat must be allowed to exit the outer shell into the surroundings. The surrounding fluid or vacuum is not considered part of the cooling system, but must be included for proper CFD boundary condition definition. According to the literature on the topic, two main outer shell heat transfer mechanisms are useful to be analyzed: convection to atmosphere, and radiation in vacuum.

The first boundary condition option is convection to atmosphere. The required heat transfer coefficient, α, can be estimated by using the technique of idealizing a thin strip of the outer surface, located on top of one cooling channel, as a flat plate when the curvature is "corrected" by flattening rather than projecting the length onto the centerline axis. The assumption of longitudinal frictionless flow and [13] are used to determine the mean heat transfer coefficient:

$$\alpha_m = \frac{2}{\sqrt{\pi}} \lambda \sqrt{\frac{w_m}{a L}} \text{ , [W/m}^2\text{-K]}, \tag{30}$$

where: λ = thermal conductivity of surrounding atmosphere, [W/m-K],

$a = \dfrac{\lambda}{c_p \rho}$ = thermal diffusivity of surrounding atmosphere, [m^2/s],

c_p = specific heat of surrounding atmosphere, [J/kg-K],

ρ = density of surrounding atmosphere, [kg/m^3],

w_m = constant average velocity of surrounding atmosphere, [m/s],

L = true cooling channel length along the surface of the chamber wall, [m].

Relatively stagnant atmospheric conditions can be assumed for the velocity.

The second boundary condition option is radiation to vacuum. No terms in the radiation heat flux of Equation (9) require extensive calculation through sub-equations when reference information is available.

3.3 Theory of Material Loading, Stress, and Failure

The rocket engine and regenerative cooling system require structural analysis and design in multiple ways for multiple locations. Analogous mathematical representations can be formed from the theories of [17] and [36].

3.3.1 Cylindrical Pressure Vessel Analogy

The combustion chamber of a rocket engine can be viewed as a cylindrical pressure vessel. For known pressure, radius, and material, a manipulation of the circumferential hoop stress equation allows the required wall thickness to be determined depending on the application:

$$t = \frac{p\,r}{\sigma}\ , \text{[m]}, \tag{31}$$

where: p = applied internal pressure, [N/m^2],

r = inner radius, [m],

σ = material static yield or ultimate stress, [N/m^2].

The longitudinal axial stress, and stresses at the inner and outer surfaces, are calculated by other

formula which result in smaller thicknesses, would give an under-designed engine, and are not considered.

3.3.2 Fixed End Beam With Uniform Pressure Load Analogy

The span of chamber wall length between two adjacent fins, at the bottom of a particular cooling channel, can be idealized as a fixed-end statically indeterminate beam with a uniform pressure load *q* acting over the entire length *L*. The situation is depicted in Figure 3-2.

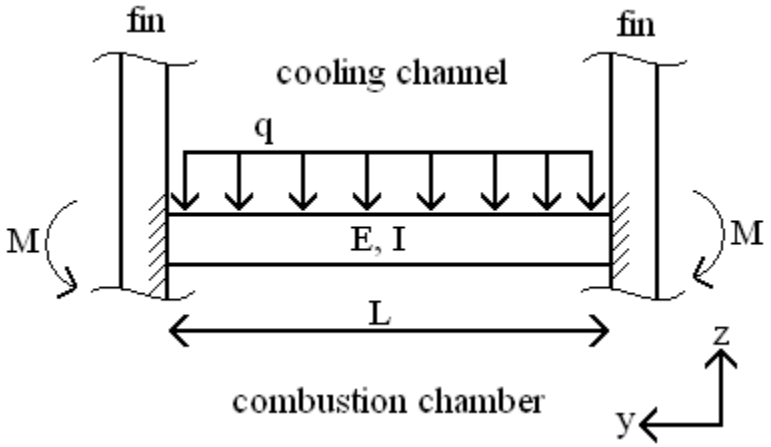

Figure 3-2: Statically indeterminate fixed-end beam representation of chamber wall span between two fins, at the bottom of one cooling channel.

The uniform pressure load as shown is a force per unit length, and can be converted to an effective pressure due to the combustion chamber pressure and the cooling channel pressure. The effective pressure is depicted in Figure 3-3.

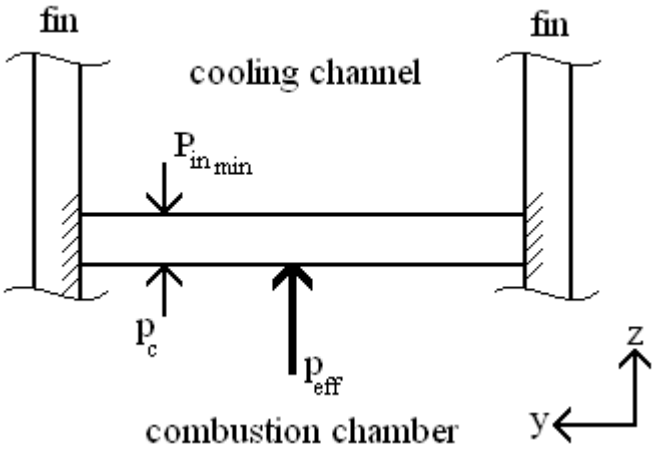

Figure 3-3: Illustration of effective pressure acting on the chamber wall.

The effective pressure is a force per unit area, assumed constant, and acts over the x direction length of the channel. Calculation thus becomes:

$$p_{eff} = P_{in\ \min} - p_c \tag{32}$$

where: $P_{in\ \min}$ = assumed maximum constant pressure experienced along the length of the channel, also equals the cooling channel minimum allowable inlet pressure, [N/m^2],

p_c = combustion chamber pressure, assumed constant along the length of the chamber, [N/m^2].

The uniform pressure load is thus equivalently:

$$q = p_{eff}\, L_{chan} \tag{33}$$

where: L_{chan} = actual length of the channel, equivalent to the "corrected" length of the chamber, [m].

Viewing the beam representation in Figure 3-4 depicts the orientation for the bending moment of inertia.

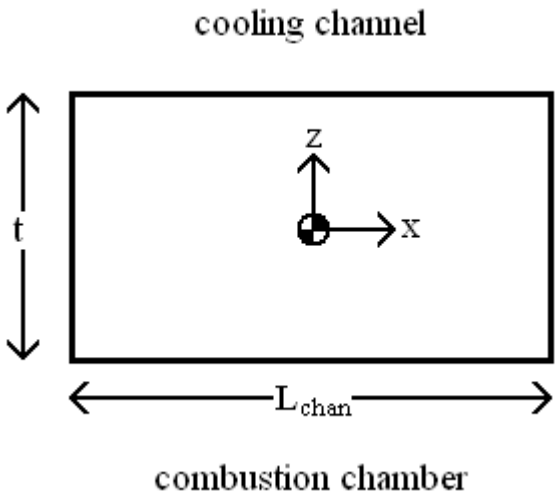

Figure 3-4: Beam representation as seen along the *y* axis.

For a rectangular cross section, the bending moment of inertia with the origin at the centroid, with respect to the *x* axis, is given by:

$$I = \frac{L_{chan}\, t^3}{12} \tag{34}$$

where: t = chamber wall thickness as depicted in Figure 3-4, [m].

Because the failure with respect to deflection is unknown, the Euler-Bernoulli theory of beam bending can be used. The moment in the beam is shown in Figure 3-2, and given by:

$$M = \frac{qL^2}{12} \ . \tag{35}$$

The flexure formula then gives the normal stresses due to the bending moments:

$$\sigma = -\frac{Mz}{I} \tag{36}$$

where: $z = -\frac{t}{2}$ = the distance in the z direction for the positive maximum stress on the face of the beam, [m].

Combining Equations (35) and (36) using limiting criteria gives a maximum allowable pseudo-beam length when solved for L:

$$L_{\max} = t_{\min}\sqrt{\frac{2\sigma_Y}{p_{eff}}} \tag{37}$$

where: $L_{\max}$ = maximum allowable channel width, [m],

$t_{\min}$ = minimum allowable chamber wall thickness, [m],

σ_Y = chamber wall material yield stress, [N/m^2].

Interestingly, the result is in the same form as the partial equation found in [16] that was not adequately defined to be used in itself. Even though the derived formulation appears consistent, not enough information is given to use the related data of [16] with a high degree of confidence.

3.3.3 Fixed End Beam With Uniform Temperature Load Analogy

Continuing the idealization of a fixed-end statically indeterminate beam, consideration of temperature effects can be included. For the regenerative cooling channel, a temperature differential exists between the combustion chamber hot gasses and the cooling channel coolant. This fluid temperature differential causes a material temperature differential between the hot-wall and the channel lower wall. Instead of Equation (35), the moment in the beam of Figure 3-2 is now:

$$M = \frac{\alpha E I \Delta T}{t} \tag{38}$$

where: α = coefficient of thermal expansion of the material, [m/m-K],

E = modulus of elasticity of the material, [N/m^2],

I is per Equation (34),

ΔT = material temperature differential, [K].

Combining with the flexure formula of Equation (36) eliminates the chamber wall thickness parameter *t*, thus a maximum temperature differential allowed before yielding occurs can be solved for:

$$\Delta T_{\max} = \frac{2\sigma_Y}{\alpha E} \quad . \tag{39}$$

3.3.4 Column Subject To Buckling Analogy

The outer shell of a coaxial engine is typically made of a material with a much higher strength than the inner shell. As such the cooling fins typical of HARCC applications, made of the lower strength inner shell material, may be subjected to loads which could cause buckling. The higher strength outer shell acts as a rigid support, fixing a fin at the top against rotation and translation, as depicted in Figure 3-5. The fin is viewed as a column with the lower end fixed against rotation, and no differential pressure load between adjoining channels.

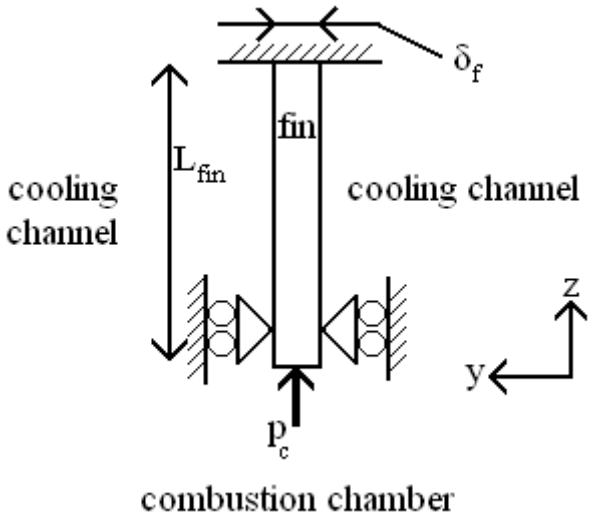

Figure 3-5: Cooling fin represented as a column subjected to buckling loads.

The bending moment of inertia for a rectangular cross section, with the origin at the centroid, is again with respect to the *x* axis. The beam representation in Figure 3-6 depicts the orientation when viewed down the column.

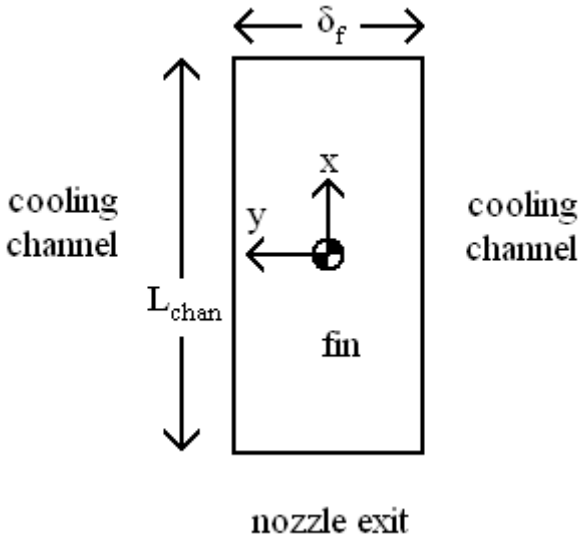

Figure 3-6: Column representation as seen along the *z* axis.

The bending moment of inertia equation is per:

$$I_{fin} = \frac{\delta_f^3 L_{chan}}{12} \quad . \tag{40}$$

The critical load which causes buckling is thus calculated using the equation:

$$F_{cr} = \frac{4\pi^2 E I_{fin}}{L_{fin}^2} \quad . \tag{41}$$

The combustion chamber pressure shown in Figure 3-5 acts over the idealized fin base area, being the base of the column representation, and can be equivalenced into a point force with:

$$F_c = p_c \delta_f L_{chan} \quad . \tag{42}$$

If the combustion chamber force is set as the critical load which causes buckling, $F_c = F_{cr}$, a ratio

can be found which relates the maximum allowable fin height to the minimum allowable fin width, for the condition that buckling will occur beyond those values. Equating Equations (41) and (42), using (40), results in:

$$\frac{L_{fin\ \max}}{\delta_{f\ \min}} = \pi \sqrt{\frac{E}{3\,p_c}} \ . \tag{43}$$

3.3.5 Recommended Criteria For Loads

The work of [10] provides an alternate basis for the definition of static pressure loading conditions which allow for a strong design. The values obtained in this manner are then combined with material stress limits and Equation (31) to determine the geometric features required to withstand the loads. For regenerative cooling systems, the process must be used twice to accommodate the chamber wall of the inner shell, and then the outer shell.

The process begins with a definition of various load types, all of which are pressures for the particular application to rocket engines. Load Type A, L_A, is defined as the working load under normal steady-state operating conditions, and is typically set by the design. Load Type B, L_B, is defined as the working load under transient operating conditions of normal engine start and stop, which can be idealized as equivalent to L_A if information is not available. Load Type C, L_C, is defined as the working load under occasional transient operating conditions of irregular starts. Load Type D, L_D, is defined as the mandatory malfunction load which must be taken into account in instances of continued operation during other component failures. The mathematical relationship is as follows:

$$L_A = \text{set by design}, \tag{44}$$

$$L_B \approx L_A \ , \tag{45}$$

$$L_C = 1.1 L_A \ , \tag{46}$$

$$L_D = 1.225 L_A \ . \tag{47}$$

The limit loads, L_L, are defined next for each load type:

$$L_{L\,A} = 1.2 L_A \ , \tag{48}$$

$$L_{L\,B} = 1.2 L_B \ , \tag{49}$$

$$L_{L\,C} = 1.1 L_C \ , \tag{50}$$

$$L_{L\,D} = 1.0 L_D \ . \tag{51}$$

The design limit load, L_{DL}, is selected as the maximum of the limit loads:

$$L_{DL} = \mathrm{MAX}\left\{L_{L\,A}, L_{L\,B}, L_{L\,C}, L_{L\,D}\right\} \ . \tag{52}$$

Finally, loads which may cause yielding, L_Y, or ultimate failure, L_U, can be determined:

$$L_Y = 1.1 L_{DL} \ , \tag{53}$$

$$L_U = 1.5 L_{DL} \ . \tag{54}$$

The material stress limits used with these loads are the associated yield, σ_Y, or ultimate, σ_U, strengths. For parts subjected to cyclic loading, the material endurance limit stress, σ_E, is used in place of the ultimate stress, if available.

3.3.6 Simplified Theory of Cyclic Loading Stress Analysis

Cyclic loading can be analyzed in a simplified manner for a preliminary stress analysis of the chamber wall using the methods and equations of [15]. Both low cycle fatigue and creep rupture life can be considered.

For the consideration of low cycle fatigue, noting that the bending pressure stresses are

maximum at the mid-channel, a design ratio can be found through rearrangement of the given equation. The result is interestingly of the same form as Equation (37):

$$\left(\frac{w}{t}\right) = \sqrt{\frac{2\sigma_B}{\left(P_{coolant} - P_{hotwall}\right)}} \tag{55}$$

where: $w = L$ of Figure 3-2 = channel width, [m],

σ_B = material bending stress maximum, [N/m^2],

$P_{coolant}$ = loading on the coolant side of the chamber wall, [N/m^2],

$P_{hotwall}$ = loading on the hot-wall, [N/m^2],

$\left(\frac{w}{t}\right) = \left(\frac{w}{t}\right)_{\max} = \left(\frac{w_{\max}}{t}\right) = \left(\frac{w}{t_{\min}}\right)$ for yield or ultimate P's and σ_B.

In the rearranged equation, the loading parameters can be taken as either the yield or the ultimate values, used with the associated yield or ultimate material stress values.

For the consideration of creep rupture life, Equation (55) is used with the rupture life stress in the place of σ_B to give the design ratio.

3.4 Using Methane as the Coolant and Fuel

The use of oxygen and methane (O_2/CH_4) in a combustion process at the proper mixture ratio requires knowledge of the expected chamber temperature. Not only is the temperature essential for defining an important numerical boundary condition, but it is needed in the utilization of the Bartz equation to determine the convective heat transfer coefficient variation on the hot-wall. Because a temperature value is not readily found in literature for this oxidizer/fuel combination, the chamber total temperature, T_{0g}, can be determined from a calculation of the adiabatic flame temperature of the combustion components per the methods of [32].

The oxidizer to fuel mixture ratio is used to setup a reaction equation of the form:

$$a\,\mathrm{CH_4} + b\,\mathrm{O_2} \rightarrow c\,\mathrm{CO_2} + d\,\mathrm{H_2O} + e\,\mathrm{CO} \tag{56}$$

where the small letters represent the molar coefficients, and carbon monoxide is included to account for the possibility of incomplete combustion. Determination of the adiabatic flame temperature is based on the energy rate balance heat transfer equation:

$$\dot{Q} = H_P - H_R \tag{57}$$

where: $\dot{Q}$ = rate of heat transfer at the combustion chamber control volume boundary, [J],

H_P = enthalpy of the products, [J],

H_R = enthalpy of the reactants, [J].

For the adiabatic condition, $\dot{Q}$ = 0, so that $H_R = H_P$. The heat transfer equation becomes, on a molar basis and summed for all products and reactants in terms of enthalpy:

$$\sum_i \left(n_i\,\overline{h}_i\right)_R = \sum_i \left(n_i\,\overline{h}_i\right)_P \tag{58}$$

where: n_i = coefficient of the reaction equation for the ith component, per mole of fuel, [kmol],

$\overline{h}_i$ = specific enthalpy for the ith component, per mole of fuel, [kJ/kmol].

The specific enthalpy for compounds not at the reference temperature of 298.15 K is found by adding the enthalpy of formation (representative values seen in Table 2-12) and the change:

$$\overline{h} = \overline{h}_f^{\circ} + \Delta\overline{h} \tag{59}$$

where: $\overline{h}_f^{\circ}$ = enthalpy of formation for a compound at the standard state, [kJ/kmol],

$\Delta\overline{h} = \overline{c}_p\,\Delta T$ = specific enthalpy change between the standard state and the state of interest, [kJ/kmol],

$\bar{c}_p$ = specific heat for a particular compound, [kJ/kmol-K],

$\Delta T = (T - 298.15)$ = change in the temperature from the standard state to the state of interest, [K],

T = temperature at the state of interest, [K].

For compounds at the reference temperature, $\Delta\bar{h} = 0$. Also, since $\bar{c}_p = \bar{c}_p(T)$, then $dh = \bar{c}_p(T)\,dT$, which can be written for substitution as:

$$\Delta\bar{h} = \int_{T_1}^{T_2} \bar{c}_p(T)\,dT \tag{60}$$

where: T_1 = initial temperature of the compound before the reaction, [K],

T_2 = final temperature of the compound after the reaction, [K].

The heat diagram method is used in the determination of temperature limits for Equation (60). The required ideal gas specific heats are calculated using the equations provided in [28], shown in Table 3-1. Finally, substitutions are made into Equation (58) to determine the required flame temperature.

Table 3-1: Ideal gas specific heats of expected combustion reactants and products, from [28].

Gas	$\bar{c}_p = \bar{c}_p(T)$, [kJ/kmol-K]; $\theta = \frac{T}{100}$, [K]
CH_4	$-672.87 + 439.74\,\theta^{0.25} - 24.875\,\theta^{0.75} + 323.88\,\theta^{-0.5}$
O_2	$37.432 + 0.020102\,\theta^{1.5} - 178.57\,\theta^{-1.5} + 236.88\,\theta^{-2}$
CO_2	$-3.7357 + 30.529\,\theta^{0.5} - 4.1034\,\theta + 0.024198\,\theta^{2}$
$H_2O(g)$	$143.05 - 183.54\,\theta^{0.25} + 82.751\,\theta^{0.5} - 3.6989\,\theta$
CO	$69.145 - 0.70463\,\theta^{0.75} - 200.77\,\theta^{-0.5} + 176.76\,\theta^{-0.75}$

3.5 Theory Required for Computational Modeling and CFD

A thorough knowledge of the assumptions and implications involved in any computational modeling technique are essential. For a pre-packaged CFD software program, additional knowledge is necessary to avoid the "black box, junk-in & junk-out" effect typical of less experienced users. In so doing, proper determination of the computational mesh, turbulence model parameters, and flow entrance length are necessary.

3.5.1 Mesh Considerations, "y" Values, Etc.

Determination of the proper mesh density is essential for obtaining reasonable results. The initial details can be calculated, but must then be adjusted through a mesh sensitivity study involving trial runs of the desired simulations.

Prandtl's "Mixing Length Theory" from the definition of shear stress, a part of the "Law of the Wall", forms the basis for determining a limit mesh size in order to realistically resolve boundary layer details at a wall. The wall friction velocity is defined per [13] and [43] as:

$$w_\tau = \sqrt{\frac{\tau_0}{\rho}} \tag{61}$$

where: τ_0 = shear stress at the wall due to the constant of integration of the momentum equation for the boundary layer in a steady-state, turbulent, stratified flow of a channel with vanishing pressure gradient, [kg/m-s^2],

ρ = density of the fluid, [kg/m^3].

Also, the non-dimensional distance from the wall is defined as:

$$y^+ = \frac{w_\tau y}{\nu} \tag{62}$$

where: y = dimensional distance from the wall, [m],

ν = kinematic viscosity of the fluid, [m^2/s].

Combining Equations (61) and (62) results in the same equation as in [41] for y^+:

$$y^+ = \frac{y}{\nu}\sqrt{\frac{\tau_0}{\rho}} \tag{63}$$

which can be written in terms of mesh nomenclature as:

$$y^+ = \frac{\Delta y_p}{\nu}\sqrt{\frac{\tau_w}{\rho}} \tag{64}$$

using: Δy_p = distance of the near-wall computational grid node to the solid surface, equivalent to the distance between the wall and the center of a CFD finite volume mesh element (i.e. the center of a FLUENT or HyperMesh mesh element), see Figure 3-7, [m],

$\tau_w = \tau_0$ = shear stress at the wall, [$kg/m\text{-}s^2$].

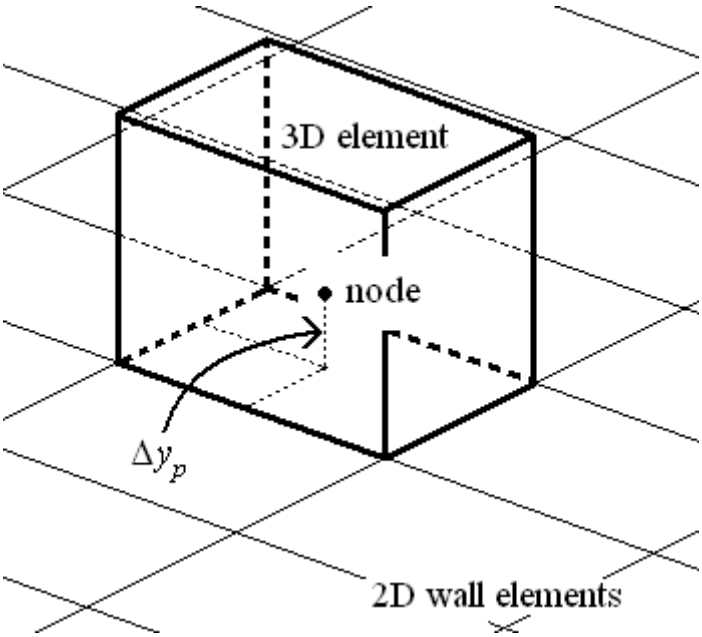

Figure 3-7: Distance of the near-wall computational node to the solid surface for a 3D CFD element.

For the near-wall, viscous, linear to 1st order, flow region the shear stress can be represented as:

$$\tau_w = \mu \frac{u_p}{\Delta y_p} \tag{65}$$

where: μ = dynamic viscosity of the fluid, [kg/m-s],

u_p = average velocity for turbulent flow at the grid node near the wall, where viscous shear dominates, [m/s].

In order to use known values for the calculation of a mesh size, note that by definition the viscosities are related to the density by:

$$\nu = \frac{\mu}{\rho}\ , \tag{66}$$

and solve for the distance Δy_p by substituting Equation (65) into (64) to obtain:

$$\Delta y_p = \frac{\left(y^+\right)^2 \mu}{u_p \rho} \quad . \tag{67}$$

By assuming an average, set the quantity $u_p \rho \approx \overline{\rho u} = G$, and substitute in Equations (22), (23), and (24) to obtain the final form for the distance between the wall and the center of a CFD finite volume mesh element:

$$\Delta y_p = \left[\frac{\left(y^+\right)^2 \mu \pi \left(\frac{2wh}{w+h} \right)^2 n_c}{4\dot{m}_t} \right] . \tag{68}$$

Equation (68) is useful for particular channel cross sectional geometries which have been previously determined, and subject to the y^+ criteria restrictions of Table 2-13.

Because the above formulation for Δy_p is not valid beyond the inner region of the boundary layer, using Equation (68) to directly determine the number of mesh elements to place along the height and width of a channel is not valid. It must be used only for the wall adjacent mesh element height, vertically or horizontally for a rectangular channel, and from that the total number can be determined with consideration for biasing possibilities. Biasing is the progressive stretching of adjacent elemental heights or widths as the element position progressively gets farther away from the wall. Also, the equation can not be used to determine the mesh density for the channel lengthwise direction, in the direction of the mean flow.

The maximum number of mesh elements theoretically required in either the vertical or horizontal direction can be found by using the minimum allowed value of y^+, resulting in the minimum allowed distance $\Delta y_{p\,\min}$, even if biasing is used. For no biasing, using a mesh with equal element heights or widths for the entire span of the vertical or horizontal direction, the

maximum number of elements can be calculated by the following. The maximum number of associated mesh elements in the vertical direction, for no biasing, is given by:

$$V_{\max} = \frac{h}{2\Delta y_{p\min}} \quad . \tag{69}$$

The maximum number of associated mesh elements in the horizontal direction, for no biasing and using the same value of $\Delta y_{p\min}$, is given by:

$$H_{\max} = \frac{w}{2\Delta y_{p\min}} \quad . \tag{70}$$

These values are also related to the number of channels, n_c, as the channel height and width are functions of n_c per Equations (20), (25), and associated.

Although not related to y^+, the channel lengthwise mesh should ideally be fine enough to resolve the variation in heat transfer coefficient along the hot-wall as calculated by Equation (10). The number of lengthwise elements can be calculated by:

$$L = \frac{L_T}{L_e} \tag{71}$$

where: L_T = total length of the channel, [m],

L_e = length per element for a non-biased mesh, [m].

3.5.2 Turbulence Model Parameters

Both the k-ε and Reynolds Stress turbulence models in a CFD simulation require initial guesses of the inlet boundary conditions for the turbulent kinetic energy, k, and turbulent dissipation rate, ε, parameters.

An explicit calculation of the inlet distribution of turbulent kinetic energy for internal flows

is performed per [41] and [47] by:

$$k = \frac{3}{2}\left(U_{avg}\, I\right)^2 \tag{72}$$

where: U_{avg} = reference average flow velocity, [m/s],

I = turbulence intensity of Table 2-14.

Combining Equations (72), (22), (23), and (24) results in the usable form:

$$k = \frac{3}{2} I^2 \left(\frac{4\dot{m}_t}{n_c \pi \left(\frac{2wh}{w+h} \right)^2 \rho} \right)^2 , [\mathrm{m^2/s^2}], \tag{73}$$

where the CFD channel inlet density, ρ, can be estimated for the coolant using Equation (17) with the coolant molecular weight, and the ideal gas law:

$$\rho = \frac{p_{inlet}}{R\, T_{inlet}} \tag{74}$$

using: p_{inlet} = channel pressure at the CFD channel inlet, [N/m^2],

T_{inlet} = channel temperature at the CFD channel inlet, [K].

In a CFD model, a pre-inlet entrance length is added upstream of the inlet to the actual modeled cooling channel of interest. The modeled cooling channel is where heat is added and what is being simulated. The CFD channel inlet is thus the inlet to the channel in the CFD model, and is upstream of the inlet to the modeled channel which is being considered. Knowledge of the modeled channel inlet pressure per Equation (5), p_{in}, can be used to determine the channel pressure at the CFD channel inlet, p_{inlet}, using the same method as before. Using the feedline pressure loss (drop) ahead of the actual channel inlet from [7] of 2.5% formulates the following relation in terms of the CFD channel inlet pressure:

$$\%\ \text{of} = \text{is}\ ,$$

$$0.025\ p_{inlet} = p_{fd}\ , \tag{75}$$

where p_{fd} is the feedline pressure drop between the CFD inlet and the modeled inlet. The CFD and modeled channel inlet pressures are thus related by:

$$p_{inlet} = p_{in} + p_{fd}\ , \tag{76}$$

and upon substitution of Equation (76) into (75) for p_{inlet} and rearrangement gives a relation for the feedline pressure drop in terms of the modeled channel inlet pressure:

$$\left(\frac{0.025\ p_{in}}{1-0.025}\right) = p_{fd}\ . \tag{77}$$

Substitution of Equation (77) back into (76) results in the desired relationship needed for Equation (74) and thus calculation of the turbulent kinetic energy per Equation (73):

$$p_{inlet} = \left(1+\frac{0.025}{1-0.025}\right) p_{in}\ . \tag{78}$$

Next, the length scale for fully developed turbulent pipe flows is calculated per [41] and [47] using the hydraulic diameter of Equation (22) by:

$$l = 0.07\,D\ . \tag{79}$$

Finally, an explicit calculation of the inlet distribution of turbulent dissipation rate for internal flows is performed per [41] and [47] by:

$$\varepsilon = C_{\mu}^{3/4}\frac{k^{3/2}}{l}\ ,\ [\text{m}^2/\text{s}^3], \tag{80}$$

where the constant coefficient parameter is seen in Table 2-15 and is C_{μ} = 0.09.

3.5.3 Pre-Channel Entrance Length

Various options are available to determine the required entrance length. The entrance length for laminar, internal, forced flow in circular tubes entering at constant velocity is given in [13] approximately as:

$$x_{e\,A} \approx 0.056\,\mathrm{Re}\,d \tag{81}$$

where: d = D = hydraulic diameter for non-circular channels, per Equation (22),

Re = Reynolds number, as previously shown with Equation (26).

The Reynolds number can be expressed based on the hydraulic diameter per channel, and average mass flow per unit area, using Equations (22) and (23), as:

$$\mathrm{Re} = \frac{G\,D}{\mu} \ . \tag{82}$$

Substitution of Equations (82), (22), and (23) into (81) results in a more useful form for this entrance length suggestion:

$$x_{e\,A} \approx 0.056\left(\frac{4}{\pi}\right)\left(\frac{1}{\mu}\right)\dot{m}_c \ . \tag{83}$$

The suggestion of [22] is to use a multiple of the heated length L:

$$x_{e\,B} = 10\,L \ . \tag{84}$$

The development of turbulent flow will occur much sooner than for laminar flow, which will require a much shorter entrance length and less computational expense. Since the CFD simulations involve the modeling of turbulence, an equation from [31] to calculate the turbulent entrance length is useful:

$$x_{e\,C} \approx 4.4\,D\left(\mathrm{Re}\right)^{1/6} \ . \tag{85}$$

Performing the same substitutions as before results in the more useful form:

$$x_{e\,C} \approx 4.4\left(\frac{4}{\pi}\dot{m}_c\frac{1}{\mu}\right)^{1/6}\left(\frac{2wh}{w+h}\right)^{5/6} \quad . \tag{86}$$

Each entrance length value should be compared for reasonableness.

CHAPTER 4

METHODOLOGY TO DESIGN AND OPTIMIZE REGENERATIVE COOLING CHANNELS

This chapter presents the methodology required for the design and optimization of regenerative cooling channels, as performed for the cSETR 50lbf engine. Although CFD software is used, extensive hand calculations are required beforehand. The design begins with a preliminary stress analysis to determine a set of design features, then involves a thermal analysis to determine a set of channel geometries to investigate, and finally the CFD software FLUENT is used to find the optimal configuration.

4.1 Preliminary Stress Analysis

The design of regenerative cooling channels begins with a preliminary stress analysis. The purpose of being preliminary is to indicate that only basic theory is involved, and must be expanded upon in future design iterations for increased structural integrity. The stress analysis itself is required to formulate specific design features which are necessary for the cooling performance, as well as to build the regenerative cooling system upon a solid structural foundation without design excess. Any future work on the design determined through this preliminary analysis should take the methods and purposes used into consideration.

4.1.1 Analysis of Loading Conditions

Proper structural design must be based on at least the minimum anticipated loading

conditions. Only pressure and temperature loads are considered for the preliminary structural analysis. Other loads are required to be analyzed for a more detailed design, for instance thrust and mounting.

The combustion chamber pressure for the cSETR 50lbf engine is used as the basis in the determination of other pressure loads and values. From Table 2-18, p_c = 1.5 x 10^6 N/m^2. Options for the minimum channel outlet pressure are then calculated using Equations (1), (2), (3), and (4), which depend on the injector design, to give:

a) Equation (1) with (2): $P_{out\ \min 1}$ = 1,542,861.60645 ≈ 1.54 x 10^6 N/m^2

b) Equation (1) with (3): $P_{out\ \min 2}$ = 1.8 x 10^6 N/m^2

c) Equation (4): $P_{out\ \min 3}$ = 3.0 x 10^6 N/m^2

Next, options for the minimum pressure drop in the cooling channel are estimated from various literature references, since actual drops will be determined in the CFD simulations:

a) from Figure 2-7 for methane: ΔP_1 = 600,000 = 0.6 x 10^6 N/m^2

b) from [6] for hydrogen used in an engine larger than the cSETR 50lbf engine:
ΔP_2 = 5.0 x 10^6 N/m^2

c) from Table 2-9 for methane used in an engine much larger than the cSETR 50lbf engine: ΔP_3 = 1,158,319.2252 ≈ 1.2 x 10^6 N/m^2

An injector pressure drop of one full value of the combustion chamber pressure as used for $P_{out\ \min 3}$ seems excessive. The injector design values are not known, but a "good" design can be assumed. The values of $P_{out\ \min 2}$ and ΔP_1 are chosen, which allow the calculation of the cooling channel minimum allowable inlet pressure from Equation (5) to be $P_{in\ \min}$ = 2.4 x 10^6 N/m^2. Finally, the effective pressure on the idealized beam located at the bottom of the channel, as per

Figure 3-3, is determined with Equation (32) to be $p_{eff} = 0.9 \times 10^6$ N/m^2.

Yield pressure and ultimate failure pressure load conditions are found individually for the inner shell and outer shell. For the inner shell, the working load under normal steady-state operating conditions is set by the design of the cSETR 50lbf engine as the chamber pressure. For the outer shell, the working load is the cooling channel minimum allowable inlet pressure. Equations (44) through (54) are used, with the resulting values shown in Table 4-1.

Table 4-1: Yield and ultimate load conditions for the inner and outer shells.

Equation	Inner Shell Value, [N/m^2]	Outer Shell Value, [N/m^2]
(44)	$L_A = p_c = 1.5 \times 10^6$	$L_A = P_{in\,\min} = 2.4 \times 10^6$
(45)	$L_B \approx 1.5 \times 10^6$	$L_B \approx 2.4 \times 10^6$
(46)	$L_C = 1.65 \times 10^6$	$L_C = 2.64 \times 10^6$
(47)	$L_D = 1.8375 \times 10^6$	$L_D = 2.94 \times 10^6$
(48)	$L_{L\,A} = 1.8 \times 10^6$	$L_{L\,A} = 2.88 \times 10^6$
(49)	$L_{L\,B} = 1.8 \times 10^6$	$L_{L\,B} = 2.88 \times 10^6$
(50)	$L_{L\,C} = 1.815 \times 10^6$	$L_{L\,C} = 2.904 \times 10^6$
(51)	$L_{L\,D} = 1.8375 \times 10^6$	$L_{L\,D} = 2.94 \times 10^6$
(52)	$L_{DL} = 1.8375 \times 10^6$	$L_{DL} = 2.94 \times 10^6$
(53)	$L_{Y\,inner} = 2.02125 \times 10^6$	$L_{Y\,outer} = 3.234 \times 10^6$
(54)	$L_{U\,inner} = 2.75625 \times 10^6$	$L_{U\,outer} = 4.41 \times 10^6$

The typical operating temperature ranges found in [16] for the hot-wall and channel lower wall are used to set an expected thermal load of $\Delta T_{exp} = (806 - 478) = 328$ K between the two walls, since the actual value will be determined in the CFD simulations. This load occurs for the inner shell which is typically made of NARloy-Z, thus the maximum temperature differential allowed before yielding occurs is calculated by Equation (39) using the properties of Table 2-5 to be $\Delta T_{max} = 71.77$ K. The expected temperature differential is greater than this yield value, but a definite conclusion can not be made because Equation (39) is not a function of the material

thickness. A thicker material of certain geometry is expected to withstand the loads, thus the result warrants the investigation of cyclic stress analysis to determine the geometry.

4.1.2 Chamber Wall Thickness Determination

Recall that when the cooling channels are milled out of the inner shell, a relatively thin portion remains in the location beneath the channels termed the "chamber wall". As the thinnest location, the chamber wall thickness is a critical design location and must be able to withstand the expected loads. This is accomplished with the circumferential stress Equation (31) to directly determine the thickness. Afterward, design ratios can be determined from literature values or other equations, for comparison and determination of other cross sectional geometry features.

From the collection of possibly used inner shell materials, Equation (31) is used with the radius of the combustion chamber, combustion chamber pressure, and various yield, ultimate, or endurance loads and material limits from Tables 2-5, 2-6, 2-18, and 4-1 to compile Tables 4-2 for minimal safety factor yield criteria, 4-3 for working loads yield criteria, and 4-4 for working loads ultimate criteria. The use of the larger combustion chamber radius adds a safety factor into the design as the results are applied to the smaller radius throat. Typically, endurance strength values are unknown, but if known they are used rather than the ultimate strength for the chamber wall which is subject to cyclic loading.

Table 4-2: Various calculated chamber wall thicknesses for minimal safety factor yield criteria designs. Equation (31) used with listed input parameters, r_{cc} = 0.01625 m, and $p_c = 1.5 \times 10^6$ N/m^2.

Material	Strength Criteria, σ_Y, [N/m^2]	Thickness, [mm]
NARloy-Z	78.3875×10^6	$t_{min\ 1} = 0.311$
Copper, Annealed	33.3×10^6	$t_{min\ 2} = 0.732$
Copper, OFHC Soft	49 or 78×10^6	$t_{min\ 3} = 0.497$ or 0.313
Copper, OFHC Hard	88 or 324×10^6	$t_{min\ 4} = 0.277$ or 0.075
Copper, Annealed OFHC	29.915×10^6	$t_{min\ 5} = 0.815$
Copper, OFHC 1/4 Hard	310×10^6	$t_{min\ 6} = 0.079$
Copper, OFHC 1/2 Hard	317×10^6	$t_{min\ 7} = 0.077$

Table 4-3: Various calculated chamber wall thicknesses for working loads yield criteria designs. Equation (31) used with listed input parameters, r_{cc} = 0.01625 m, and $L_{Y\ inner} = 2.02125 \times 10^6$ N/m^2.

Material	Strength Criteria, σ_Y, [N/m^2]	Thickness, [mm]
NARloy-Z	78.3875×10^6	$t_{min\ 8} = 0.419$
Copper, Annealed	33.3×10^6	$t_{min\ 9} = 0.986$
Copper, OFHC Soft	49 or 78×10^6	$t_{min\ 10} = 0.67$ or 0.421
Copper, OFHC Hard	88 or 324×10^6	$t_{min\ 11} = 0.373$ or 0.101
Copper, Annealed OFHC	29.915×10^6	$t_{min\ 12} = 1.098$
Copper, OFHC 1/4 Hard	310×10^6	$t_{min\ 13} = 0.106$
Copper, OFHC 1/2 Hard	317×10^6	$t_{min\ 14} = 0.104$

Table 4-4: Various calculated chamber wall thicknesses for working loads ultimate or endurance criteria designs. Equation (31) used with listed input parameters, r_{cc} = 0.01625 m, and $L_{U\,inner}$ = 2.75625 x 10^6 N/m^2.

Material	Strength Criteria, σ_U or σ_E, [N/m^2]	Thickness, [mm]
NARloy-Z	137.9 x 10^6 (note: σ_E)	$t_{min\,15}$ = 0.325
Copper, Annealed	210 x 10^6	$t_{min\,16}$ = 0.213
Copper, OFHC Soft	215 x 10^6	$t_{min\,17}$ = 0.208
Copper, OFHC Hard	261 x 10^6	$t_{min\,18}$ = 0.172
Copper, Annealed OFHC	202 x 10^6	$t_{min\,19}$ = 0.222
Copper, OFHC 1/4 Hard	330 x 10^6	$t_{min\,20}$ = 0.136
Copper, OFHC 1/2 Hard	344 x 10^6	$t_{min\,21}$ = 0.130

The thickness results represent the minimum allowable thicknesses for the associated load and strength values. The worst-case-scenario for the chamber wall thickness is $t_{min\,12}$ = 1.098 mm. This value also exceeds the minimum allowable chamber wall thickness reported in [7], [12], and [16]. Even though the value obtained is not for NARloy-Z, this material is the most likely to be used for engine construction and its higher strength adds to the safety factor of the design.

With the chamber wall thickness determined, the radius to the outer surface of the chamber wall (to the bottom of the channel) is found by combining the inner surface throat radius from Table 2-18 to be r_o = 0.006248 m. Because the above stress calculations used the larger chamber radius, the resulting thicker wall when applied to the throat adds a safety factor to the critical thermal and stress location of the throat. Had the throat radius been used before, the wall thickness would have been much less and resulted in a weaker design. The construction of the engine is likely to be from one piece of material with a constant wall thickness from the nozzle, to the throat, to the combustion chamber.

4.1.3 Outer Shell Thickness Determination

Calculation of the outer shell thickness is performed in a manner similar to that for the chamber wall, using Equation (31). Because the fin height has not yet been found in the proceeding thermal analysis, an estimated radius value to the outer shell must be used. Starting with the chamber radius, the maximum possible fin height is about 8 mm, thus the value to the outer shell can be $r_J = 25.065$ mm. For an Inconel 718 outer shell, Tables 2-7 and 4-1 are used to obtain the minimum permissible thicknesses shown in Table 4-5.

Table 4-5: Various calculated outer shell thicknesses for Inconel 718 subject to different loading conditions. Equation (31) used with listed input parameters and $r_J = 25.065$ mm.

Pressure Load, [N/m^2]	Strength Criteria, [N/m^2]	Thickness, [mm]
$P_{in\ \min} = 2.4 \times 10^6$	$\sigma_Y = 980 \times 10^6$	$t_{\min J\ 1} = 0.0614$
$L_{Y\ outer} = 3.234 \times 10^6$	$\sigma_Y = 980 \times 10^6$	$t_{\min J\ 2} = 0.083$
$L_{U\ outer} = 4.41 \times 10^6$	$\sigma_U = 1100 \times 10^6$	$t_{\min J\ 3} = 0.1$

The worst-case-scenario for the outer shell thickness is $t_{\min J\ 3} = 0.1$ mm, however due to the limitations of HyperMesh a value of $t_J = 1.0$ mm is required, and is realistic.

4.1.4 Channel Width to Chamber Wall Thickness Design Ratio

A set of specific design ratios is required to relate the above calculated chamber wall thickness to other geometric features of the cooling channel cross section. The first such design ratio involves the channel width and chamber wall thickness, $\left(\frac{w}{t}\right)$, which can be interpreted as $\left(\frac{w}{t}\right) = \left(\frac{w}{t}\right)_{\max} = \left(\frac{w_{\max}}{t}\right) = \left(\frac{w}{t_{\min}}\right)$ for yield or ultimate loads and material strengths.

Therefore, the most critical ratio quantity which represents a likely failure design is the largest, and the ratio which represents a low chance for failure is the smallest.

Various literature references are utilized for the extraction of this ratio from the values they provide, not necessarily at the throat because a maximum ratio is needed in the determination of failure probability. A maximum channel width, or minimum chamber wall thickness, provides the maximum ratio. Tables 2-1, 2-4, and 2-2 are used to formulate this ratio, and the values are reported in Tables 4-6, 4-7, and 4-8. The values for Table 4-7 from [6] require the calculation of the chamber wall thickness using Equation (31), the pressure of 11 x 10^6 N/m^2, the assumed material OFHC 1/4 hard copper in Table 2-6, and chamber radius of 0.06 m, giving t = 2.129 mm.

Table 4-6: Literature values of the channel width to chamber wall thickness ratio, as found from [16] and Table 2-1.

Channel Width, w, [mm]	Chamber Wall Thickness, t, [mm]	Ratio, $\left(\frac{w}{t}\right)$
0.301	7.6	0.0396
0.338	7.6	0.0445
0.335	7.6	0.0441
0.663	7.6	0.0872
0.442	7.6	0.0582
0.373	0.635	0.5874
0.963	7.6	0.1267
0.427	7.6	0.0562
0.564	7.6	0.0742
0.919	7.6	0.1209
1.016	7.6	0.1337
0.411	7.6	0.0541
2.169	7.6	0.2854
0.569	7.6	0.0749

Table 4-7: Literature values of the channel width to chamber wall thickness ratio, as found from [6] and Table 2-4.

Design Number	Ratio, $\left(\frac{w}{t}\right)$	Design Note
2	0.298258	"good"
3	0.596515	
4	0.417561	"better"
5	0.894773	"optimal"

Table 4-8: Literature values of the channel width to chamber wall thickness ratio, as found from [18] and Table 2-2.

Configuration Number	Ratio, $\left(\frac{w}{t}\right)$	Design Note
1	1.910112	"average life"
2	1.146067	"long life"
3	0.285393	"no failure"

The life analysis performed by [6] and [18] places the focus on the values in Tables 4-7 and 4-8, especially noting that [16] has given unreasonable values before. To place the values into perspective, recall the statement of [15] that a value of this ratio is not favored over 1.0 due to the resulting maximum pressure stress being in bending, as failure is more likely to occur in bending rather than in shear for this structural configuration.

The channel width to chamber wall thickness ratio can be calculated when cyclic, yield, and ultimate load conditions are taken into consideration, using Equation (37) or (55) and the values in Tables 2-5, 2-6, and 4-1. For the terms given in Equation (55), with the yield criteria the terms represent $P_{hotwall} = L_{Y\,inner}$, $P_{coolant} = L_{Y\,outer}$, and $\sigma_B = \sigma_Y$, where for the ultimate criteria the terms represent $P_{hotwall} = L_{U\,inner}$, $P_{coolant} = L_{U\,outer}$, and $\sigma_B = \sigma_U$ or σ_E. For creep rupture life considerations, $\sigma_B = \sigma_R$. The resulting ratios are shown in Table 4-9 for the various possible inner shell materials.

Table 4-9: Values of the channel width to chamber wall thickness ratio for various inner shell materials, as found from Equation (55).

Material	Yield, $\left(\frac{w}{t}\right)_Y$	Ultimate, $\left(\frac{w}{t}\right)_U$	Rupture, $\left(\frac{w}{t}\right)_R$
NARloy-Z	11.369798	12.914042	yield loads: 5.840493 ultimate loads: 5.001499
Copper, Annealed	7.410568	15.936381	
Copper, OFHC Soft	8.989331 or 11.341661	16.124984	
Copper, OFHC Hard	12.046772 or 23.115424	17.766436	
Copper, Annealed OFHC	7.023828	15.629884	
Copper, OFHC 1/4 Hard	22.610502	19.977311	
Copper, OFHC 1/2 Hard	22.864357	20.396671	

Because material failure considerations were taken into account for determining the values in Table 4-9, the values are maximums placed on this ratio. The absolute maximum is $\left(\frac{w}{t}\right)_{\text{abs max}}$ = 5.001499, thus no actually used geometries should exceed this value. If the ratio used is well below the maximum, cyclic failure is not extremely likely within a reasonable engine life. Taking the advice of [15], the optimal ratio $\left(\frac{w}{t}\right)$ = 0.894773 from [6] is justified for determining the maximum channel width for a constant chamber wall thickness. Also, the smallest "no failure" ratio of Table 4-8, $\left(\frac{w}{t}\right)$ = 0.285393, is used to determine the minimum width for a constant thickness.

4.1.5 Fin Width to Channel Width Design Ratio

The next required design ratio links the previously determined design features to a new quantity. The fin width to channel width ratio, $\left(\frac{\delta_f}{w}\right)$, can be interpreted as $\left(\frac{\delta_f}{w}\right) = \left(\frac{\delta_f}{w}\right)_{\max} = \left(\frac{\delta_{f\ \max}}{w}\right) = \left(\frac{\delta_f}{w_{\min}}\right)$ if necessary to correspond to the previously determined channel width, but is usually not a fixed quantity because the fin width can be varied along the engine length to accommodate the varying circumference for a designed channel width. Therefore, only the ratio at the thermally critical throat location is necessary for definition, and the ratio can be adjusted at a later time for the other engine locations in consideration of channel pressure drop.

Various literature references are utilized for the extraction of this ratio from the values they provide. Table 2-4 and [12] are used, and the values are reported in Table 4-10.

Table 4-10: Literature values of the fin width to channel width ratio, as found from [12] and Table 2-4.

Design Number	Ratio, $\left(\frac{\delta_f}{w}\right)$	Design Note
1 and 3	7.4 or 2.7	
2	1.1	"good"
4	1.1	"better"
5	1.1	"optimal"
none, [12]	1.0	

No options are available for calculating this ratio in the literature for the critical throat location, therefore the most commonly used $\left(\frac{\delta_f}{w}\right) = 1.1$ is chosen due to its use in all of the noted best designs of Table 4-10 and fitting into the negligible influence range given by [15].

4.1.6 Fin Height to Fin Width Design Ratio

The next design ratio to be considered again links the previously determined design features to a new quantity. The fin height to fin width ratio, $\left(\frac{L_{fin}}{\delta_f}\right)$, can be interpreted as $\left(\frac{L_{fin}}{\delta_f}\right) = \left(\frac{L_{fin}}{\delta_f}\right)_{\max} = \left(\frac{L_{fin\ \max}}{\delta_f}\right) = \left(\frac{L_{fin}}{\delta_{f\ \min}}\right)$ as for previous ratios, but is more useful as a comparison tool.

Various literature references are utilized for the extraction of this ratio from the values they provide, however only [6] is useful as [16] does not give the required inputs directly. Table 2-4 is used, and the values are reported in Table 4-11.

Table 4-11: Literature values of the fin height to fin width ratio, as found from Table 2-4.

Design Number	Ratio, $\left(\frac{L_{fin}}{\delta_f}\right)$	Design Note
1 and 3	5.405 or 2.852	
2	4.545	"good"
4	4.545	"better"
5	4.545	"optimal"

The fin height to fin width ratio is also calculated when column buckling possibilities are taken into consideration, using Equation (43) and Table 2-5 for NARloy-Z. Calculating the ratio gives $\left(\frac{L_{fin\ \max}}{\delta_{f\ \min}}\right)$ = 527.771, which upon comparison to the values in Table 4-11 suggests that buckling in this manner is not a concern. Furthermore, the fin height will later be calculated directly based on optimized heat transfer into the coolant.

4.1.7 Summary of Important Values for Later Use

The values presented in Table 4-12 are compiled based on the results of the literature review and the preliminary stress analysis, and are required for additional calculations. The pressure values are also used for comparison to the CFD results of the present research.

Table 4-12: Summary of important values to be used in the present research for subsequent calculations and comparison.

Property Description	Value
Channel Width Minimum Fabrication Limit	$w \geq 0.5$ mm
Channel Height Maximum Fabrication Limit	$h \leq 8$ mm
Inner Shell Material	NARloy-Z
Outer Shell Material	INCONEL 718
Minimum Allowable Cooling Channel Outlet Pressure	$P_{out\ \min 2} = 1.8 \times 10^6$ N/m^2
Minimum Allowable Cooling Channel Inlet Pressure	$P_{in\ \min} = 2.4 \times 10^6$ N/m^2
Minimum Combustion Chamber Wall Thickness	$t_{\min 12} = 1.098$ mm
Radius of Throat on Outer Surface	$r_o = 0.006248$ m
Outer Shell Thickness	$t_J = 1.0$ mm
Channel Width to Chamber Wall Thickness Design Ratio, For Maximum w	$\left(\frac{w_{\max}}{t}\right) = 0.894773$
Channel Width to Chamber Wall Thickness Design Ratio, For Minimum w	$\left(\frac{w_{\min}}{t}\right) = 0.285393$
Fin Width to Channel Width Design Ratio	$\left(\frac{\delta_f}{w}\right) = 1.1$

4.2 Thermal Analysis

The design of regenerative cooling channels next involves a thermal analysis to determine a set of channel geometries to investigate in the subsequent CFD simulations. With the design features obtained through the preliminary stress analysis, the thermal analysis can proceed by applying the theories of heat transfer to the combustion chamber, cooling fins and channels, and outer shell.

The effects of the wall contour and channel curvature on the coolant flow characteristics are not studied in the present research, since they can be studied separately from the thermal effects. Instead, the Bartz equation is utilized to provide the curvature induced heat transfer coefficient variation along the hot-wall, but with straight channels. The curvature may have an effect on the cooling performance, therefore this method provides an initial set of results to which the curvature effects can be added for future research.

4.2.1 Combustion Chamber Thermal Conditions

The thermal analysis of a rocket engine begins with the combustion of the fuel and oxidizer, which is the source of the heat which must be extracted by the regenerative cooling system. Knowledge of the combustion temperature is necessary to then find the amount of heat that is transferred to the hot-wall surface and into the chamber wall of the inner shell. From the chamber wall, the heat is then transferred to the cooling channels via the channel lower wall, or into the fins and then into the channel via the fin walls adjacent to the coolant.

4.2.1.1 adiabatic flame temperature of combustion

The combustion temperature is determined through a calculation of the adiabatic flame temperature of the combusting gasses, comprised of oxygen and methane (O_2/CH_4), subject to the following assumptions. Adiabatic combustion at constant enthalpy for an ideal gas mixture is assumed, which itself assumes complete combustion although an incomplete combustion process must be considered due to the mixture ratio balance requirements of Equation (56). Also, the reactants begin at the steady state injection temperature of methane, equivalent to the temperature at the channel outlet per Table 2-9, of T_i = 526.222 K. This value is assumed since the actual value will be determined in the CFD simulations. The pressure dependence on the reaction is unknown, H_2O stays gaseous, and component properties are determined from Tables 2-12 and 3-1.

It is assumed that the given mixture ratio of Table 2-18 is on a mass basis because of the $\dot{m}$ ratio equivalence, thus it must be converted to a molar basis:

$$MR_{molar} = \left(\frac{0.0575\,\text{kg O}_2}{0.018\,\text{kg CH}_4}\right)\left(\frac{16.0426\,\text{kg CH}_4}{1\,\text{kmol CH}_4}\right)\left(\frac{1\,\text{kmol O}_2}{31.998\,\text{kg O}_2}\right) = 1.60135209701\,\frac{\text{kmol O}_2}{\text{kmol CH}_4}$$

The incomplete combustion reaction, Equation (56), is subject to the following conditions in order to balance properly:

1) to balance based on mixture ratio: $\frac{b}{a} = 1.60135209701$
2) to balance carbon: $a = c + e$
3) to balance hydrogen: $a = (1/2)\,d$
4) to balance oxygen: $b = c + (1/2)\,d + (1/2)\,e$

Equation (58) is for per mole of fuel, so the coefficient a = 1. When balanced, the following molar coefficients are discovered:

a) reactants:

1) $n_{CH4\ R} = 1$ kmol

2) $n_{O2\ R} = 1.60135209701$ kmol

b) products:

1) $n_{CO2\ P} = 0.20270419402$ kmol

2) $n_{H2O\ P} = 2$ kmol

3) $n_{CO\ P} = 0.79729580598$ kmol

Because $\bar{h}°_f$ of Table 2-12 is given for the standard condition temperature T° = 298.15 K, and since the reactants begin at the assumed injection temperature of T_i = 526.222 K, the reactants must be "cooled" down to T° before the reaction, then allowed to react from T° up to the adiabatic flame temperature desired, T^{ad}. When Equation (59) is substituted into Equation (58), the heat equation becomes:

$$n_{CH4\ R}\left(\bar{h}_f^\circ + \Delta\bar{h}\right)_{CH4\ R} + n_{O2\ R}\left(\bar{h}_f^\circ + \Delta\bar{h}\right)_{O2\ R} = n_{CO2\ P}\left(\bar{h}_f^\circ + \Delta\bar{h}\right)_{CO2\ P} +$$

$$+ n_{H2O\ P}\left(\bar{h}_f^\circ + \Delta\bar{h}\right)_{H2O\ P} + n_{CO\ P}\left(\bar{h}_f^\circ + \Delta\bar{h}\right)_{CO\ P} .$$

Next, using Equation (60) gives:

$$n_{CH4\ R}\ \bar{h}_{f\ CH4\ R}^\circ + n_{O2\ R}\ \bar{h}_{f\ O2\ R}^\circ + \int_{526.222}^{298.15}\left[n_{CH4\ R}\ \bar{c}_{p\ CH4}(T) + n_{O2\ R}\ \bar{c}_{p\ O2}(T)\right]dT =$$

$$= n_{CO2\ P}\ \bar{h}_{f\ CO2\ P}^\circ + n_{H2O\ P}\ \bar{h}_{f\ H2O\ P}^\circ + n_{CO\ P}\ \bar{h}_{f\ CO\ P}^\circ +$$

$$+ \int_{298.15}^{T^{ad}}\left[n_{CO2\ P}\ \bar{c}_{p\ CO2}(T) + n_{H2O\ P}\ \bar{c}_{p\ H2O}(T) + n_{CO\ P}\ \bar{c}_{p\ CO}(T)\right]dT .$$

This equation is solved for T^{ad} using the symbolic mathematics solver program MAPLE, giving T^{ad} = 4,269.158187 K as shown in Appendix I. Comparing this value to the lower values from

Table 2-18, [10], and [15], indicates that any subsequent calculations using this flame temperature will result in a desirable over-design as it adds an inherent safety factor to the cooling system.

4.2.1.2 parameters needed for the Bartz equation

Certain parameters and terms in the Bartz equation of Equations (10) and (11) require preliminary definition. First, the hot-wall temperature, T_{wh}, is unknown directly as that value is to be determined in the CFD simulations and is controlled by the cooling system performance. An assumed average reference value from literature is used to obtain an initial heat transfer coefficient, then if desired the value found from the later CFD results can be used in an iterative approach in future research. The value from [16] is chosen, T_{wh} = 806 K.

Next, the temperature ratio found in the σ correction factor of Equation (11) is defined using the adiabatic flame temperature determined previously:

$$\left(\frac{T_{wh}}{T_{0g}}\right)=\left(\frac{T_{wg}}{(T_c)_{ns}}\right)=\left(\frac{806}{4269.158187}\right)=0.188796 \ ,$$

which falls between the (1/8) and (1/4) curves in Figure 2-5. The last item needed in order to find the σ correction factor placement is the specific heat ratio of Equation (12), using the reaction coefficients determined previously and the values from [31]:

$$\gamma_{mixture}=\gamma_{avg}=\frac{\sum_i n_i\gamma_i}{\sum_i n_i}=\frac{n_{\text{CH4 R}}\ \gamma_{\text{CH4}}+n_{\text{O2 R}}\ \gamma_{\text{O2 R}}}{n_{\text{CH4 R}}+n_{\text{O2 R}}}=$$

$$=\frac{1(1.299)+1.601(1.395)}{2.601}=1.358 \ ,$$

which falls between the 1.3 and 1.4 curves. A linear interpolation using Equation (13) is used to determine the proper correction factor values between the bounding temperature and specific heat curves. Then, the Prandtl number of Equation (14) is Pr = 0.752146219884.

The dynamic viscosity is calculated using Equation (15) with proper unit conversion. To begin, the molecular weight of the combustion products is found using Table 2-12:

$$MW = MW_{CO2} + MW_{H2O} + MW_{CO} = 44.009 + 18.0148 + 28.01 = 90.0338 \left[\frac{\text{kg}}{\text{kmol}} \right] ,$$

converted to:

$$MW = \left(90.0338 \frac{\text{kg}}{\text{kmol}} \right) \left(\frac{1 \text{ lbm}}{0.45359237 \text{ kg}} \right) \left(\frac{1 \text{ kmol}}{1000 \text{ mol}} \right) = 0.198490552211 \left[\frac{\text{lbm}}{\text{mol}} \right] .$$

The temperature used is the adiabatic flame temperature, converted:

$$T = T^{ad} = 4269.158187 \left[\text{K} \right] = 7684.4847366 \left[\text{R} \right] .$$

Therefore, the dynamic viscosity becomes μ_0 = 4.45 x 10^{-7} [lb/in-sec], and when converted back to the required units:

$$\mu_0 = \left(4.45 \times 10^{-7} \frac{\text{lb}}{\text{in sec}} \right) \left(\frac{0.45359237 \text{ kg}}{1 \text{ lbm}} \right) \left(\frac{1 \text{ in}}{2.54 \times 10^{-3} \text{ m}} \right) = 7.95164004164 \times 10^{-5} \left[\frac{\text{kg}}{\text{m s}} \right] .$$

The specific gas constant of the combustion gas products is calculated from Equation (17) and converted to:

$$R = \left(\frac{8.314}{90.0338} \right) \left(\frac{\text{kJ}}{\text{kmol K}} \right) \left(\frac{\text{kmol}}{\text{kg}} \right) \left(\frac{1000 \text{ J}}{1 \text{ kJ}} \right) = 92.3430978144 \left[\frac{\text{J}}{\text{kg K}} \right] ,$$

so that the combustion gas specific heat of Equation (16) is c_{p0} = 350.284711821 [J/kg-K].

The local cross sectional area is found graphically from Figure 1-10.

4.2.1.3 Bartz heat transfer coefficient variation

The heat transfer coefficient variation along the hot-wall is determined along the true channel length from Table 2-18, using the local cross sectional area variation from Figure 1-10, the correction factor variation from Figure 2-5, the Bartz Equation of Equation (10), and a numerically based spreadsheet software. The result, shown in Appendix II, compares well to literature examples when graphed in Figure 4-1, with the nozzle exit at the far left, the expected peak at the throat, and the injector at the far right. For comparison, the variation along the true "flattened" channel length (not axially projected) is shown with the variation along the axially projected length. The true length is needed for a CFD simulation using a straight channel with no curvature.

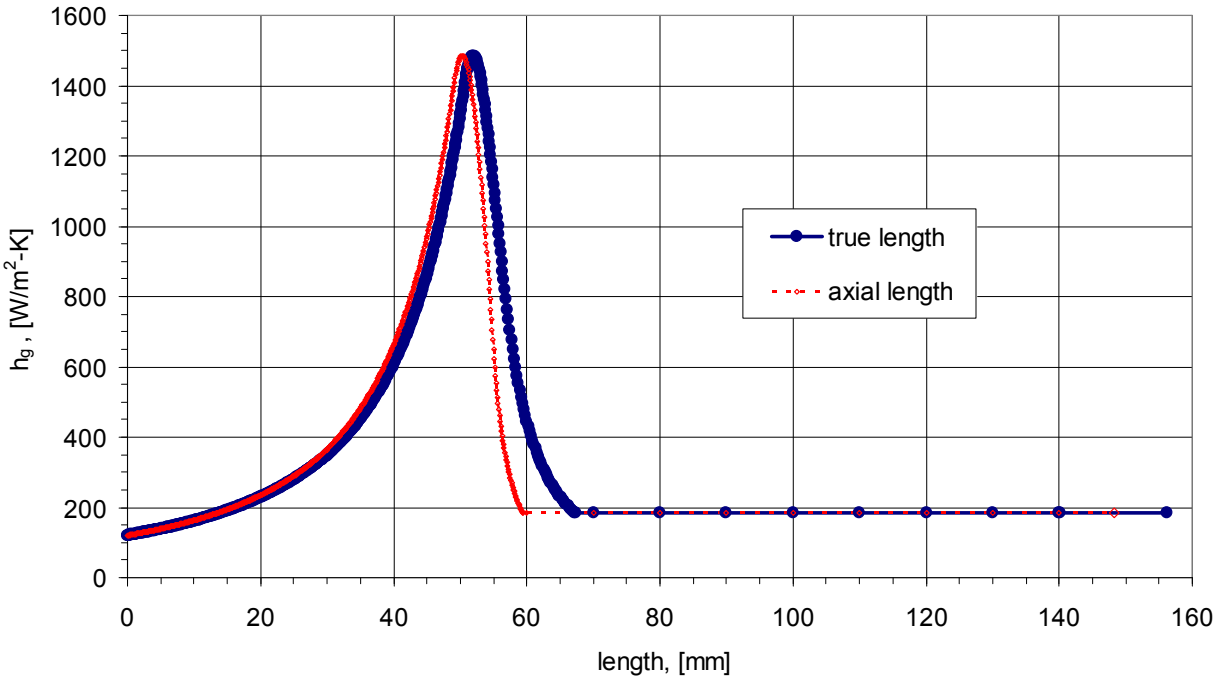

Figure 4-1: Heat transfer coefficient variation of Bartz along the cSETR 50lbf engine hot-wall versus length along hot-wall. The left portion is in the engine nozzle, the peak indicates the throat, and the right portion is in the combustion chamber. Values correspond to Appendix II.

4.2.2 Fin and Cooling Channel Thermal Conditions

The thermal analysis of the fin and cooling channel determines the geometries which provide optimal heat transfer from the solid fin to the fluid coolant, beginning with a determination of the fin height. Multiple geometries are possible due to the circumferential allowance for different numbers of channels, n_c, each geometry providing the optimal heat transfer for the particular n_c.

4.2.2.1 fin height and heat transfer coefficients

The extended surface cooling fin equation of Equation (20) is used to determine the fin height which provides the optimal heat transfer, subject to fabrication constraints. Combining the fin width to channel width design ratio of Table 4-12 and the circumferential length relationship of Equation (25) gives the following allowance for the fin width in terms of the number of channels and outer throat radius:

$$\delta_f = \left(\frac{22}{21}\right)\left(\frac{\pi\, r_o}{n_c}\right) .$$

Substituting this term into the fin height equation, rearrangement, and application to multiple inputs of the heat transfer coefficient gives:

$$h_i = 1.4192\left(\frac{11\,\pi\, r_o\, \lambda_f}{21\, n_c}\right)^{0.5} \left(\alpha_{g\,i}\right)^{-0.5} - \left(\frac{11\,\pi\, r_o}{21\, n_c}\right) ,$$

where the subscript *i* indicates the pairing.

Equation (25) and the ratio of Table 4-12 are also rearranged to give the channel width allowance:

$$w = \left(\frac{2\,\pi\, r_o}{2.1\, n_c}\right) .$$

Using this term with the bulk mean temperature as the standard state condition temperature, and Equations (22), (23), and (24), allows the first heat transfer coefficient of Equation (21) to be rearranged into the form:

$$\alpha_{g\,1} = \mathrm{A}\left(\frac{\dot{m}_t}{n_c}\right)^{0.8}\left(\frac{2\,\pi\,r_o\,h}{\pi\,r_o + 1.05\,n_c\,h}\right)^{-1.8},$$

which contains the fin height, and where the constants have been grouped into:

$$\mathrm{A} = 0.023\left(\frac{4}{\pi}\right)^{0.8} c_p^{0.33}\,\mu_b^{-0.47}\,\lambda_b^{0.67}.$$

Similarly by following [28], the other heat transfer coefficients of Equations (26), (27), and (28) become:

$$\alpha_{g\,2} = \mathrm{B}\left(n_c\right)^{-0.8}\left(\frac{2\,\pi\,r_o\,h}{\pi\,r_o + 1.05\,n_c\,h}\right)^{-1.8},$$

with

$$\mathrm{B} = 0.023\left(\frac{4}{\pi}\right)^{0.8} \lambda_b^{0.6}\,\mu_b^{-0.26}\,c_p^{0.4}\,\mu_w^{-0.14}\,\dot{m}_t^{0.8};$$

and,

$$\alpha_{g\,3} = \mathrm{D}\left(n_c\right)^{-0.8}\left(\frac{2\,\pi\,r_o\,h}{\pi\,r_o + 1.05\,n_c\,h}\right)^{-1.8},$$

with

$$\mathrm{D} = 0.027\left(\frac{4}{\pi}\right)^{0.8} \lambda_b^{2/3}\,\mu_b^{-49/150}\,c_p^{1/3}\,\mu_w^{-0.14}\,\dot{m}_t^{0.8};$$

and,

$$\alpha_{g\,4} = \mathrm{E}\left(n_c\right)^{-0.8}\left(\frac{2\,\pi\,r_o\,h}{\pi\,r_o + 1.05\,n_c\,h}\right)^{-1.8},$$

with

$$\mathrm{E} = 0.029\left(\frac{4}{\pi}\right)^{0.8}\lambda_b^{2/3}\,\mu_b^{-7/15}\,c_p^{1/3}\left(\frac{T_{co}}{T_{wc}}\right)^{0.55}\dot{m}_t^{0.8}.$$

This rearrangement shows that all of the equations are basically the same, differing only by the constant terms.

4.2.2.2 parameters needed for coolant side heat transfer

Certain parameters and terms require preliminary definition for the subsequent fin height and coolant side heat transfer calculations. For coolant bulk temperature requests, as the quantity is unknown before the CFD simulations, the standard reference temperature of T_{co} = 298.15 K is chosen. Also unknown beforehand is the cooling channel lower wall temperature, thus per [16] the value used is T_{wc} = 533 K.

Setting the cooling channel lower wall temperature allows the calculation of the coolant viscosity at that wall temperature, μ_w, using Sutherland's Equation of Equation (29) and the bounding viscosity values from Table 2-11. The constants become:

a) $C_2 = 1.01567799509 \times 10^{-6}$ kg/m-s-K$^{1/2}$

b) S = 180.182597411 K

Thus, at T_{wc} = 533 K, $\mu_w = 1.7525 \times 10^{-5}$ kg/m-s.

Equation (25) and the ratio of Table 4-12 are again rearranged to give the number of channels possible for the outer throat radius and some channel width:

$$n_c = \left(\frac{2 \pi r_o}{2.1 w} \right) .$$

The minimum number of cooling channels possible is stress limited and found using this relationship, the maximum width ratio, and other values from Table 4-12. The maximum width calculates to w_{max} = 0.000982 m, and the minimum number of channels is rounded to the whole number of $n_{c\ min}$ = 19.

The maximum number of cooling channels possible is fabrication limited and found using the above relationship, the minimum width ratio, and other values from Table 4-12. The minimum width possible calculates to w_{min} = 0.0003 m, which is below the fabrication limits of [3] so a value of w_{min} = 0.0005 m must be used. The maximum number of channels is thus $n_{c\ max}$ = 37.

4.2.2.3 iteration of fin height equation

With the heat transfer coefficient equations containing the fin height as a variable, and the fin height equation containing the heat transfer coefficient as a variable, the equation for the fin height must be iterated to find the optimal value. The option of four heat transfer coefficient equations increases the complexity. A numerical iteration algorithm, shown in Appendix III, is written in the MATLAB programming language with the above equations, constants, and relationships to perform the required computations. The algorithm handless divergence as it takes each of the four heat transfer coefficient equations and pairs them one at a time with the fin height equation, resulting in four heights to choose from. This is done for each of the possible number of channels, n_c from 19 to 37, resulting in an additional selection of fin heights.

The results of the iterations, given in Appendix IV, show that each heat transfer equation

gives similar coefficient and height values. The choice of which to use is not clear, so an average is taken to provide only the nineteen heights associated with the possible n_c. Only two n_c with the maximum height of 8 mm is used, reducing n_c to the range from 22 to 37. By using the nomenclature that $n_c = 22$ represents the geometry needed for the case of 22 total channels placed about the engine circumference, and so on for all n_c, then only sixteen CFD channel models are needed in total and are represented by $n_c = 22$ to $n_c = 37$.

The channel cross sectional details of Figures 4-2 through 4-5, some resulting from the averaging, are used for the CFD models.

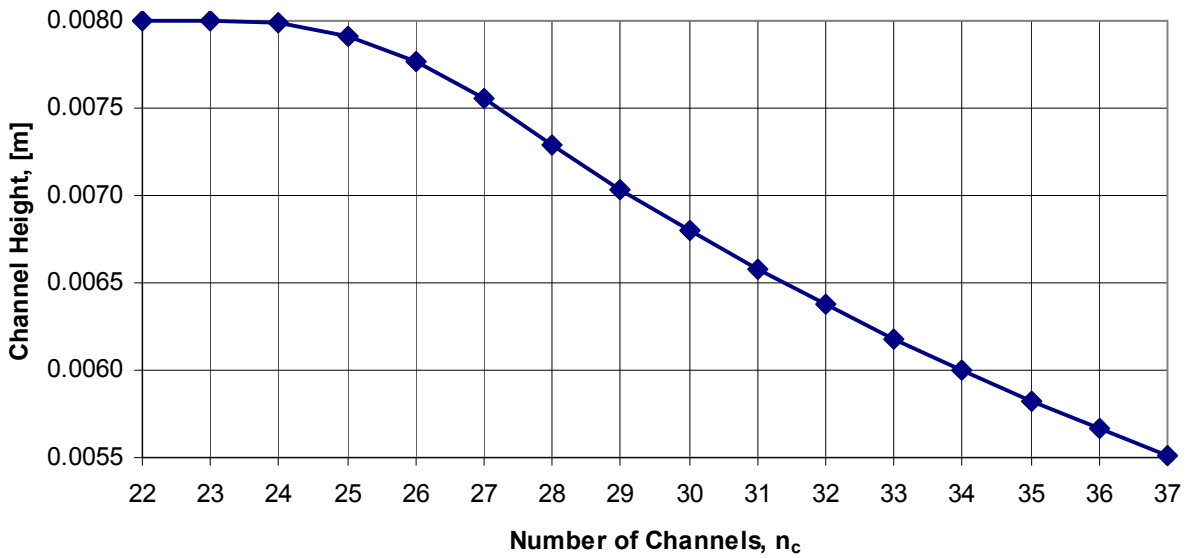

Figure 4-2: Geometry variation for the channel models n_c of channel height. Values correspond to Appendix IV.

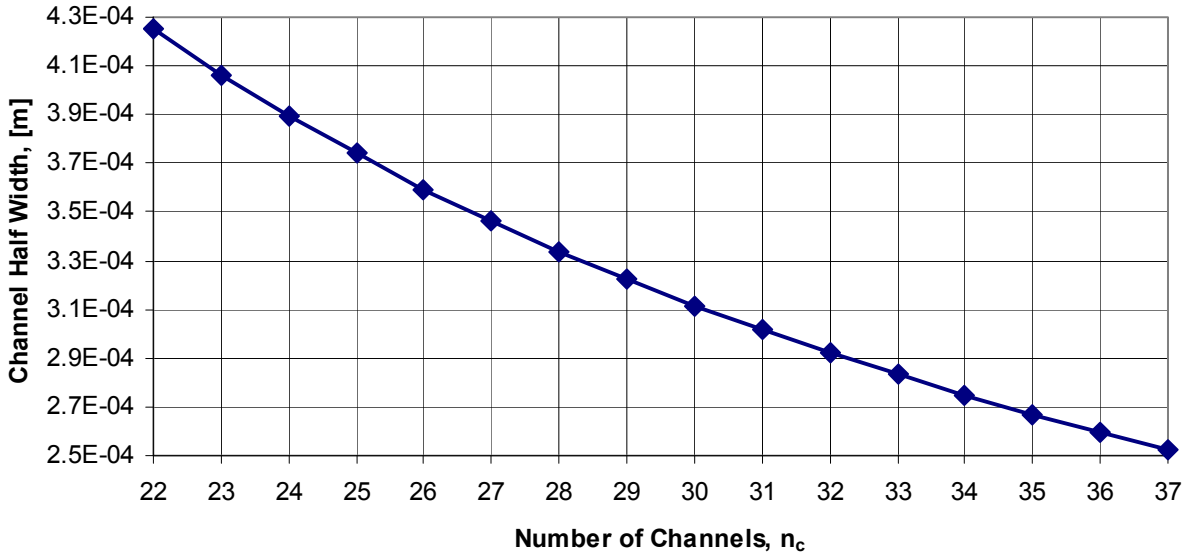

Figure 4-3: Geometry variation for the channel models n_c of the CFD modeled channel half widths. Values correspond to Appendix IV.

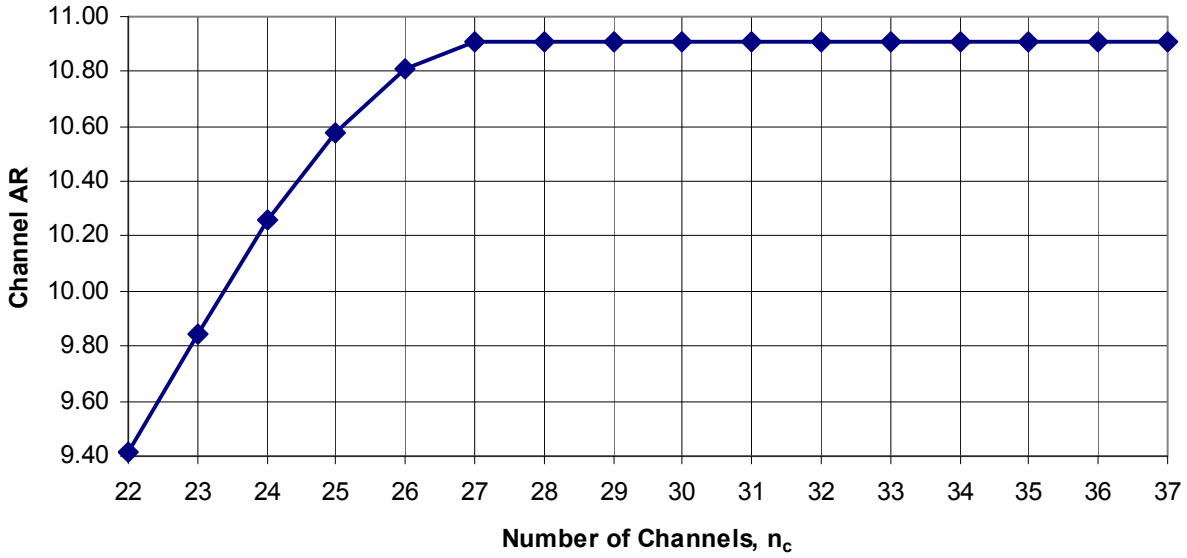

Figure 4-4: Geometry variation for the channel models n_c of the channel aspect ratio using the channel height and full width. Values correspond to Appendix IV.

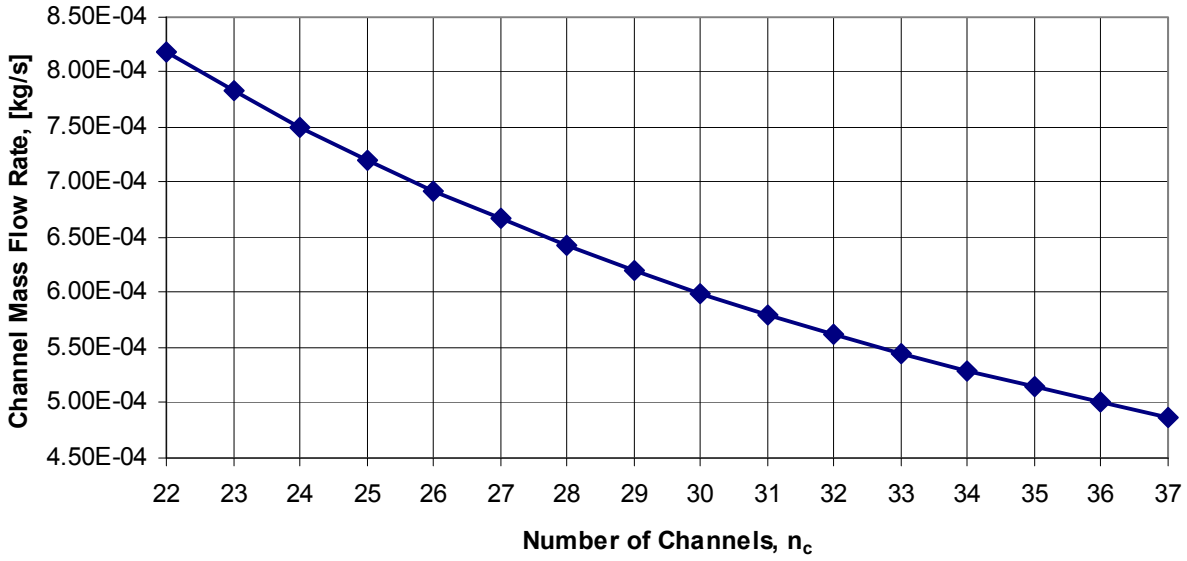

Figure 4-5: Flow variation for the channel models n_c of the channel mass flow rate. Values correspond to Appendix IV.

4.2.3 Outer Shell Thermal Conditions

Two boundary condition options are used for the outer shell thermal conditions. The first is convection to atmosphere. The properties of air from Table 2-17, a relatively stagnate condition of w_m = 1.0 m/s, and Equation (30) are used to give the mean heat transfer coefficient on the outer surface of α_m = 15.592445 W/m^2-K.

The second option is radiation to vacuum. The emissivity of rough surfaced nickel from [29] is used, with an exterior radiation sink temperature assumed to be T_∞ = 1 K for Equation (9) so that the vacuum of space is not at absolute zero. To compare, the average temperature on the Moon is about 20 K.

4.3 Pre-Channel Flow Calculations

As previously explained, in an experimental or CFD model, a pre-inlet entrance length is added upstream of the inlet to the actual channel section of interest. Flow calculations are performed to determine the upstream entrance length, using Equations (83), (84), and (86) with the geometries of Appendix IV. These equations give either unreasonably long or short entrance lengths, though the turbulent Equation (86) is likely to be at the more accurate end of the spectrum. Therefore, a middle value of one full channel length is added to the inlet, so that in the CFD models the CFD channel inlet represents the inlet to the coolant feedline. The inlet to the portion of the channel which represents the regenerative cooling channel is at the location downstream (now half way) where heat addition begins, and is termed the *modeled-inlet* since it does not represent an actual CFD inlet. In coordinates, using Table 2-18, the CFD inlet is at x = -0.1562488, the modeled inlet is at x = 0.0, and the cooling channel outlet is at x = 0.1562488.

4.4 CFD Setup Parameters

Several steps are necessary to organize the geometries of Appendix IV and prepare them for use in the subsequent CFD models.

4.4.1 Geometry Organization

The geometries in Appendix IV require organization in order to be applied to a CFD model, mainly to define CFD model geometry coordinates. The fin height is equivalent to the channel height, and because of symmetry only half of the fin width and half of the channel width need to be modeled in the cross section. The representation shown in Figure 4-6 shows the locations of

the points which are organized by n_c in Appendix V.

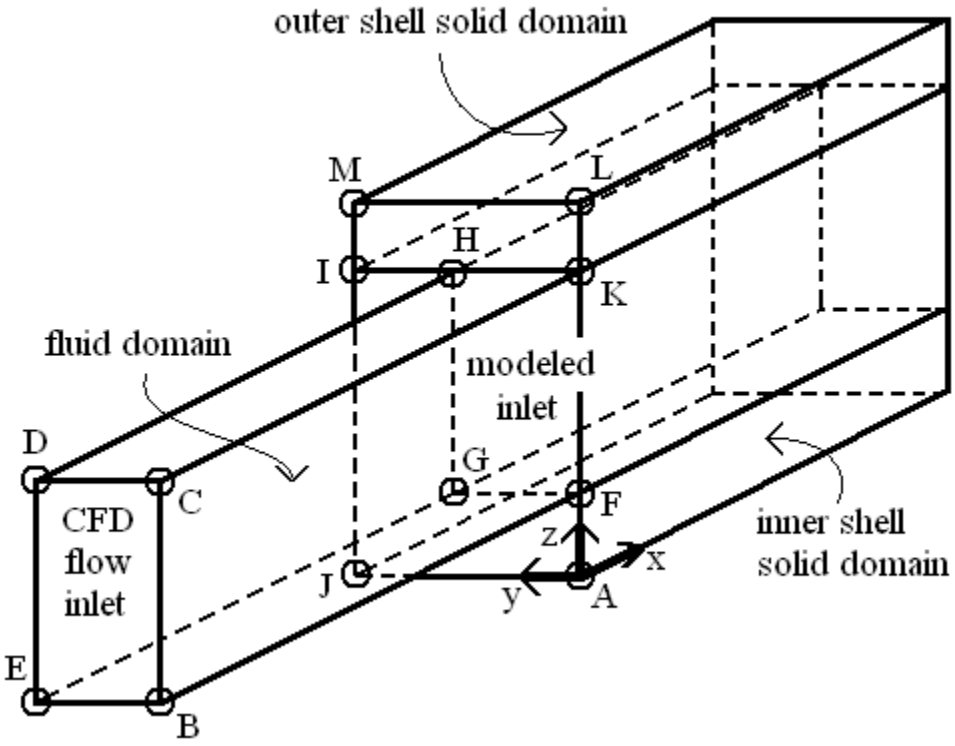

Figure 4-6: Representation of the CFD modeled geometry with drawing coordinate locations indicated. Points associated with Appendix V.

4.4.2 Initial Mesh Determination

The initial mesh for the fluid portion of the geometry is determined using Equation (68) for the dimensional distance for the first mesh element center, for only the n_c = 22 and n_c = 37 channel geometries from Appendix IV, using Tables 2-17 and 2-18, and y^+_{min} = 30. This mesh will be refined in the subsequent mesh refinement study.

For n_c = 22, w = 0.00085 m, h = 0.008 m, and Equation (68) gives $\Delta y_{p\ \min\ 22}$ = 2.2177 x 10^{-5} m. For n_c = 37, w = 0.000505 m, h = 0.0055122 m, and Equation (68) gives $\Delta y_{p\ \min\ 37}$ = 1.352

x 10^{-5} m. The associated maximum permissible mesh elements in the vertical and horizontal directions, for a non-biased rectangular mesh, are given by Equations (69) and (70) as $V_{max\ 22}$ = 181, $H_{max\ 22}$ = 20, $V_{max\ 37}$ = 204, and $H_{max\ 37}$ = 19. The horizontal number represents the full channel width. As n_c increases, y^+ increases to above y^+_{min} for the vertical direction, allowing the use of $V_{max\ 22}$ as an absolute vertical maximum number of elements for all n_c. The widths don't change as dramatically as the heights for varying n_c, and since they are so close, $H_{max\ 22}$ is also used.

For the lengthwise mesh, the discretization of the engine geometry and the Bartz heat transfer coefficient used a Δx = 0.1 mm, thus for the total channel length of L_T = 312.4976 mm, Equation (71) gives L = 3215 elements ideally. This value may lead to excessive computational times at little added benefit from a smaller value, and is limited by the CFD software license total cell limit. The channel cross section mesh is favored, and the lengthwise mesh is reduced to 1000 or less.

4.4.3 HyperMesh Geometry Generation

The geometries for each n_c of Appendix V are placed into separate HyperMesh geometry and mesh generation files, and the overall significant figures are reduced to a maximum of four. The mesh information is listed in a later section. The particularly important zones are defined in Figure 4-7. The very small angles associated with the radial placement of fins and channels about a circumference are not modeled due to insufficient solution sensitivity information from [3], [5], [7], and [18]. Four representative examples of the resulting HyperMesh geometries are shown in Figures 4-8, 4-9, 4-10, and 4-11.

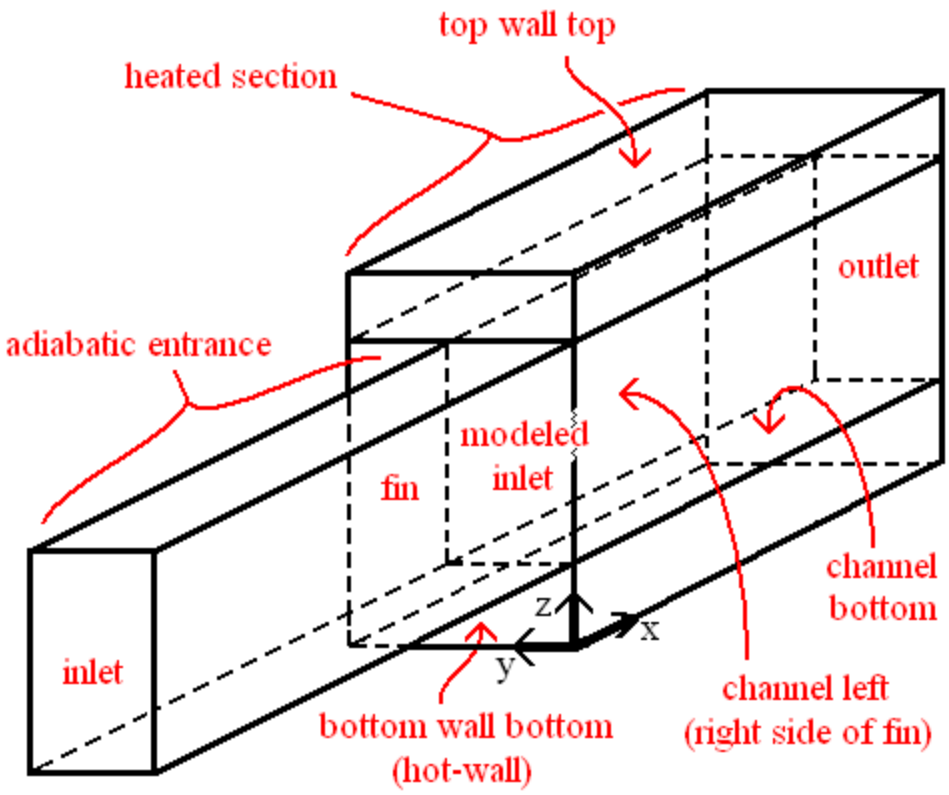

Figure 4-7: 2D wall zones, channel inlets and outlet, and 3D regions.

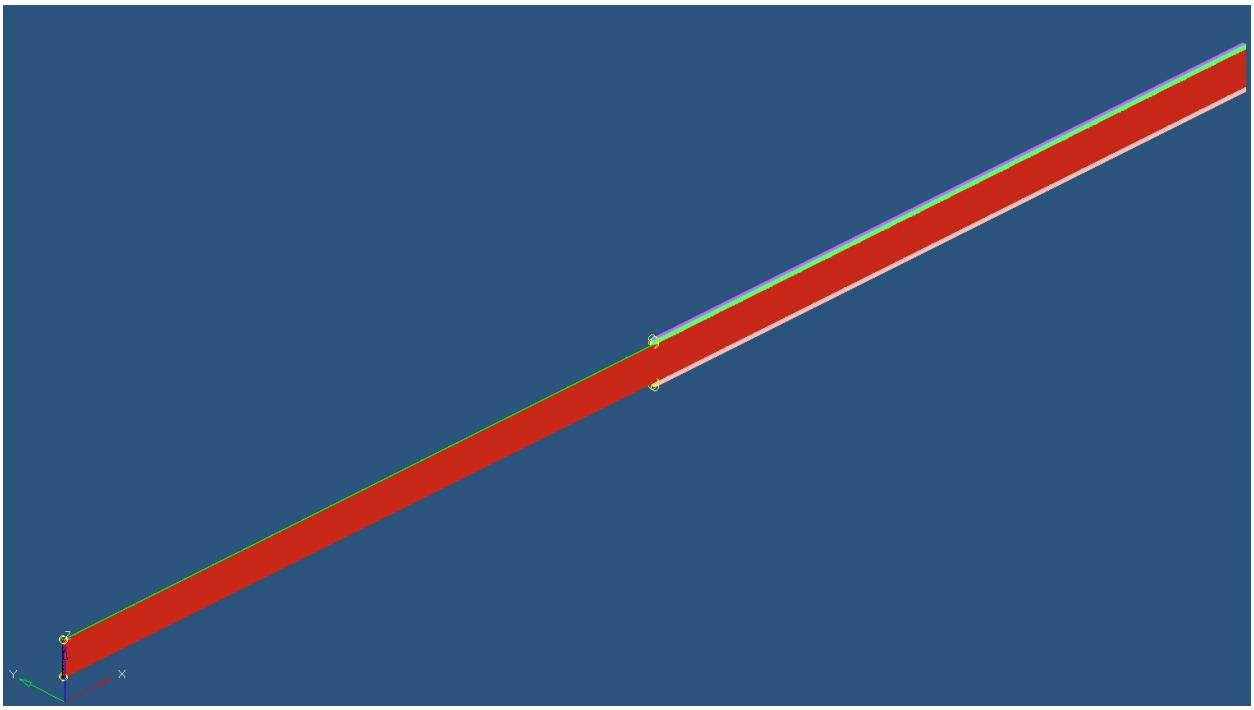

Figure 4-8: Isometric view of entire representative channel.

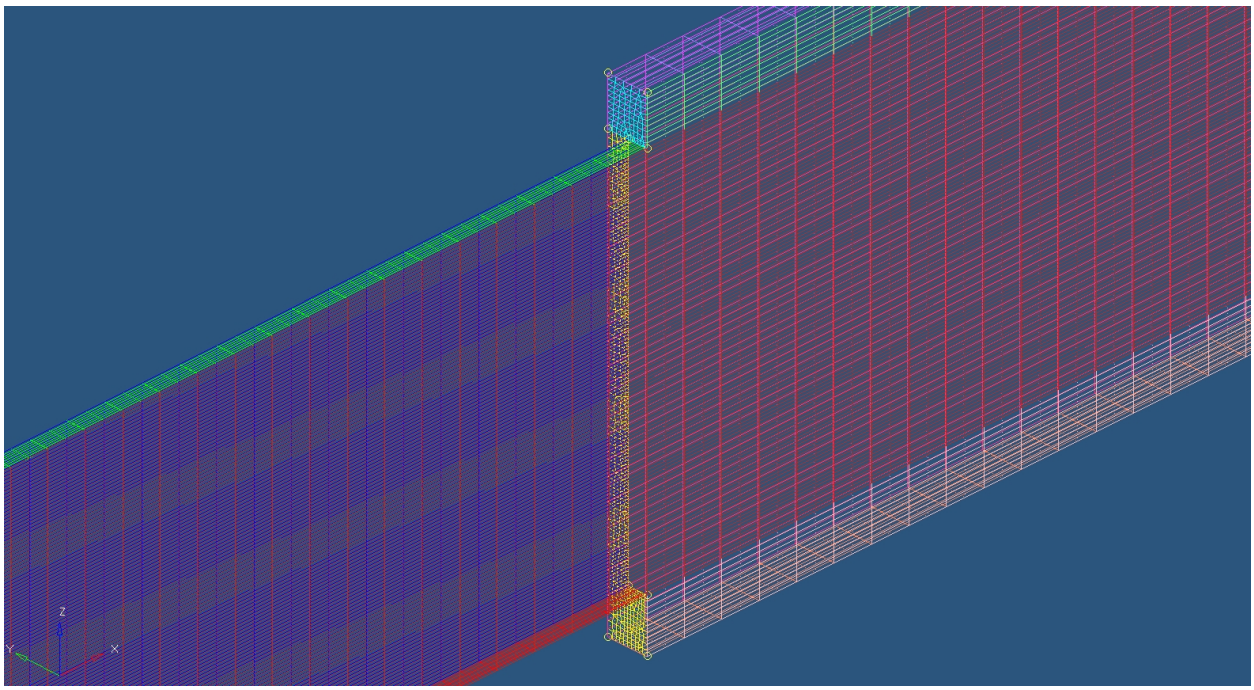

Figure 4-9: Modeled-inlet area showing the solid domains for a representative channel.

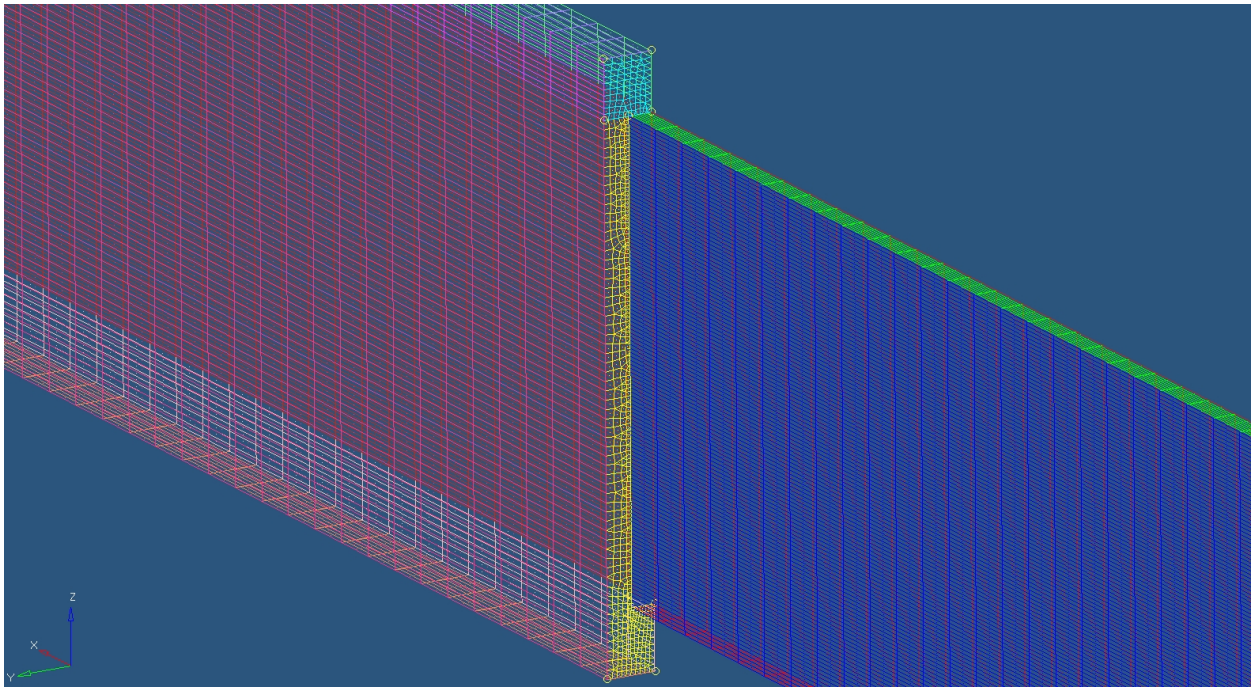

Figure 4-10: Alternate view of modeled-inlet area for a representative channel.

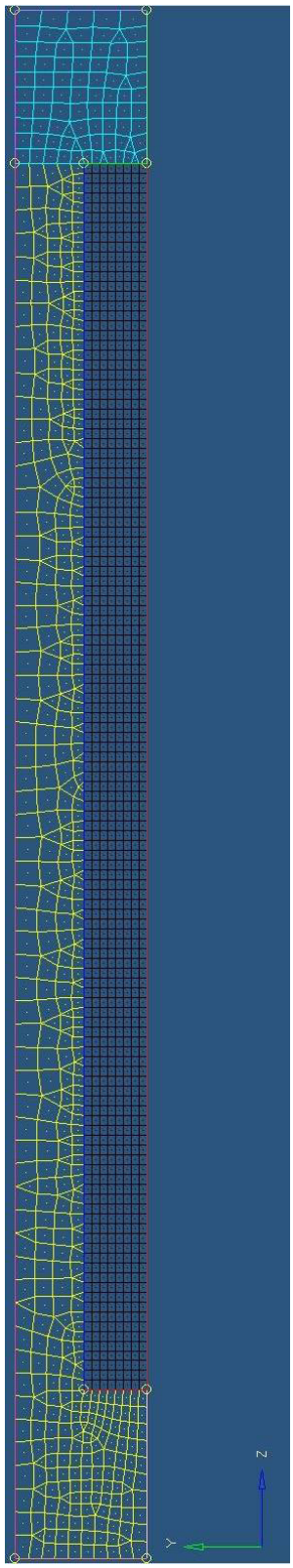

Figure 4-11: View of inlet of a representative channel showing solid domains, mesh, and half channel and fin widths. Symmetry planes are on both the left and right sides.

4.4.4 FLUENT Setup Parameters

The final step before running the CFD simulations is to setup the FLUENT models. Bartz heat transfer coefficient boundary condition input files, turbulence calculations, and case options need to be set.

4.4.4.1 boundary condition input files

The variation in the Bartz heat transfer coefficient on the hot-wall, as seen in Figure 4-1, is taken in its numerically discretized form along the true length and set into a numerical *x-y-z* coordinate grid which corresponds to each n_c channel individually since the widths are all different. The grid is located on the hot-wall, and is where the hot-wall is modeled in the HyperMesh files. The sixteen resulting mesh profile data files are loaded individually into the corresponding FLUENT case file. The Bartz heat transfer coefficient can then be used as a wall thermal boundary condition.

4.4.4.2 turbulence model parameters

The turbulence parameters are calculated for the CFD flow inlet, and applied in FLUENT as turbulence boundary conditions. Using a 2% turbulence intensity, geometry from Appendix IV, methane properties from Tables 2-12 and 2-18, setting the turbopump exit temperature as the value for the feedline entrance and CFD flow inlet from Table 2-9, and Equations (73), (74), (78), (79), and (80), the values for $n_c = 22$ are calculated as:

a) $p_{inlet} = 2{,}461{,}538.46154$ N/m^2

b) $\rho = 40.233233$ kg/m^3

c) $k = 0.07213\ m^2/s^2$

d) $l = 1.07570621469 \times 10^{-4}\ m$

e) $\varepsilon = 29.591453\ m^2/s^3$

These values compare well with [46], while the larger values for $n_c = 37$ don't.

4.4.4.3 FLUENT case options and parameters

The options and parameters used in the FLUENT case files for the present research are listed in Tables 4-13 through 4-21. The 2D walls separating the 3D fluid and solid zones are set as coupled interface wall zones to allow heat interaction. Smooth surface channel walls are used with no roughness effects included, and no carbon deposits on any surface.

Table 4-13: FLUENT models prescribed.

Model	Property	Value
Solver	dimension	3D
	precision	double
	solver type	pressure based
	time formulation	steady
	velocity formulation	absolute
	solver formulation	implicit
Energy	energy equation	activated
Viscous	model 1	k-epsilon 2 equation
	model 2	Reynolds Stress 7 equation
Gas	ideal	methane
Operating Condition	operating pressure	0 pa

Table 4-14: FLUENT viscosity model parameters prescribed.

Model	Property	Value
k-ε	type	realizable
	constants	default
	near wall treatment / wall handling	standard wall functions
	viscous heating / dissipation	activated
RSM	type	linear-pressure strain
	constants	default
	near wall treatment / wall handling	standard wall functions
	viscous heating / dissipation	activated
	wall bc from k equation	activated
	wall reflection effects	activated

Table 4-15: FLUENT domain values prescribed.

Domain	Material	Property	Value
Fluid	methane	density, [kg/m3]	ideal gas
		Cp, [j/kg-k]	piecewise-polynomial
		thermal conductivity, [w/m-k]	0.0332, constant
		viscosity, [kg/m-s]	1.087e-05, constant
Solid, Inner Shell	user defined from copper, NARloy-Z	density, [kg/m3]	9134
		Cp, [j/kg-k]	373
		thermal conductivity, [w/m-k]	295
Solid, Outer Shell	user defined from nickel, Inconel 718	density, [kg/m3]	8190
		Cp, [j/kg-k]	435
		thermal conductivity, [w/m-k]	11.4

Table 4-16: Bottom-wall-bottom (hot-wall) FLUENT wall zone boundary conditions.

Property	Value
material	narloy-z
thermal condition	convection
heat transfer coefficient, [w/m2-k]	loaded Bartz profile file
free stream temperature, [k]	4269.158187

Table 4-17: Inlet FLUENT mass flow inlet zone boundary conditions.

Property	Value
mass flow rate, [kg/s]	n_c dependent per Appendix IV
supersonic/initial gauge pressure, [pa]	2461538.46154
turbulent kinetic energy, [m2/s2]	0.07213
turbulent dissipation rate, [m2/s3]	29.591453
total (stagnation) temperature, [k]	118.055555

Table 4-18: Outlet FLUENT pressure outlet zone boundary conditions.

Property	Value
gauge (static) pressure, [pa]	1.8e+06
turbulent kinetic energy, [m2/s2]	0.07213
turbulent dissipation rate, [m2/s3]	29.591453
backflow total (stagnation) temperature, [k]	118.055555

Table 4-19: Top-wall-top FLUENT wall zone boundary conditions.

Property	Value
material	inconel718
thermal condition 1	convection
heat transfer coefficient, [w/m2-k]	15.592445
free stream temperature, [k]	298.15
thermal condition 2	radiation
external emissivity	0.41
external radiation temperature, [k]	1

Table 4-20: Various other FLUENT boundary conditions.

Zone	Type	Property	Value
multiple 2D adiabatic entrance	wall	heat flux, [w/m2]	0
left and right side walls and right side channel	symmetry		
multiple external 2D	wall	heat flux, [w/m2]	0
multiple internal 2D	interface		

Table 4-21: FLUENT solution monitors, methods and controls.

Parameter	Property	Value for Iterations 1 to 100	Value for Iterations 101 to Convergence
Residual Monitors	Absolute Criteria	1e-06 for k-ε	1e-06 for k-ε
		1e-04 for RSM	1e-04 for RSM
Pressure-Velocity Coupling Method	Coupled		
Spatial Discretization Methods	Gradient	Least Squares Cell Based	Least Squares Cell Based
	Pressure	Second Order	Second Order
	Density	First Order Upwind	QUICK
	Momentum	First Order Upwind	QUICK
	Turbulent Kinetic Energy	First Order	QUICK
	Turbulent Dissipation Rate	First Order	QUICK
	Reynolds Stress (RSM only)	First Order Upwind	QUICK
	Energy	First Order Upwind	QUICK
Solution Controls, k-ε	Courant Number	20 to 30, 100	20 to 30, 100
Solution Controls, RSM	Courant Number	50	50
Solution Controls, both	Relaxation Factors	default	default
Equations	Flow, Turbulence, Energy, Reynolds Stresses (RSM only)		

4.5 Running the CFD Simulations

The solution behavior and residuals are monitored as the simulations are running to properly utilize the CFD software and ensure that the results are accurate.

4.5.1 General Simulation Running Techniques and Behavior

The simulations are performed in groups depending on the parameters used:

a) mesh & turbulence sensitivity study, channel $n_c = 22$:
    1) k-ε group, 6 meshes, convection outer shell
    2) RSM group, 6 meshes, convection outer shell
b) main study with chosen mesh and turbulence model, channels $n_c = 22$ through 37:
    1) convection outer shell
    2) radiation outer shell

Each simulation, 44 in total, is set to run for 100 iterations with the low order discretizations shown in Table 4-21. The discretizations are changed to higher order, then the simulations are continued until convergence.

Convergence is achieved when the equation residuals continue to smoothly decrease for each successive iteration, and reach the criteria shown in Table 4-21, at which point the simulations automatically end. In the process of iterating, when FLUENT reports AMG Solver issues and the solution diverges to the point of automatically ending or stalling, the simulations are stopped and the Courant number is adjusted. For the mesh & turbulence sensitivity study, a Courant number of 100 is permitted, though for the main study values of 30 or down to 20 are required. The initial iterations still report AMG Solver problems, but with the lower Courant numbers, FLUENT automatically handles the issue and the simulations continue with fewer or no

problems until convergence. Convergence is found in under 400 iterations, and is achieved in under one hour while running on a quad-core desktop PC in a 3 processor parallel mode.

4.5.2 Mesh & Turbulence Sensitivity Study

The simulations performed for the mesh & turbulence sensitivity study use one channel geometry and the fluid domain mesh densities of Table 4-22. Decreasing the mesh density from the calculated density has the effect of increasing the y^+ value of the wall adjacent cell, which does not violate the y^+ criteria. Domains are matched to the adjoining domain mesh so there is no boundary discontinuity. The lengthwise mesh covers the total channel length of L_T = 312.4976 mm.

Table 4-22: Mesh & turbulence sensitivity study fluid domain mesh densities.

Model	Vertical (z)	Half Width Horizontal (y)	Lengthwise (x)
nc22_-6	50	4	100
nc22_-5	75	4	150
nc22_-4	100	4	200
nc22_-3	125	4	250
nc22_-2	150	6	350
nc22_-1	125	8	400
nc22_0, as calculated, exceeds total cell limit so not used	181	10	1000

The determination of the adequate mesh is done graphically by superimposing plots of line rake solution data for all the mesh density models to see which plot is different. The adequate mesh is the one with the lowest density and consistent results. The determination of the proper turbulence model is easier since the RSM plots do not show smooth curves like those of the k-ε

plots, instead they wiggle. In the plots, it is seen that the solid portions could probably use a higher density, but that is not allowed due to the software cell limitations. The thinness of the channels dictates that the horizontal mesh density is more sensitive to adjustment and should be kept as high as possible.

4.5.3 Main Study

The mesh and turbulence model chosen from the mesh & turbulence sensitivity study for use in the main study of channel models n_c = 22 to 37 are:

a) fluid domain, V x H x L: 125 X 8 X 380

b) solid domain: matched at edges; as dense as allowed by software cell limitations

c) turbulence model: k-ε

With these values used to setup HyperMesh and Fluent case files, the simulations are performed and the results of the main study are given in the next chapter. The initialization is performed at the inlet, giving the values shown in Figures 4-12 and 4-13. Recall that the focus of the current research is on the cooling performance and selection of the proper n_c geometry and configuration for use with the cSETR 50lbf engine.

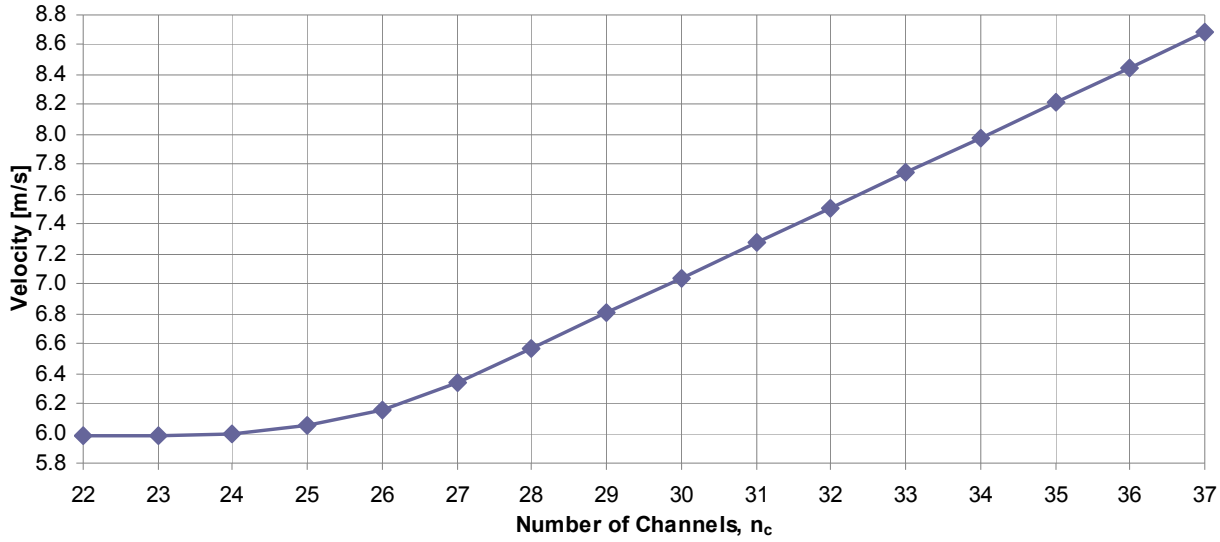

Figure 4-12: Main study initialized *x* velocity variation for the channel models n_c for both convection and radiation boundary types.

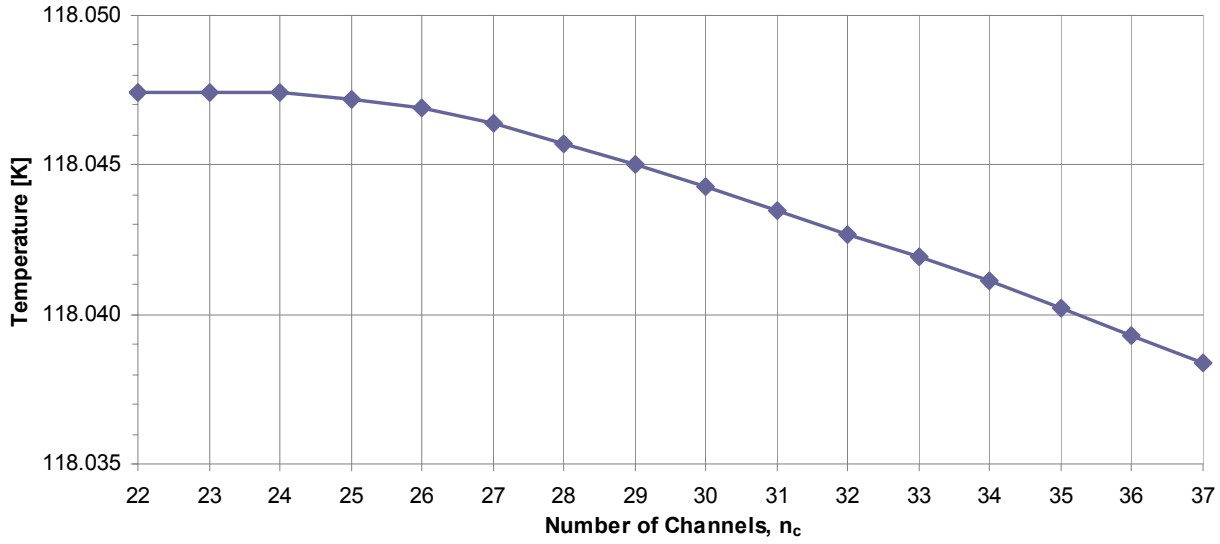

Figure 4-13: Main study initialized temperature variation for the channel models n_c for both convection and radiation boundary types.

CHAPTER 5

RESULTS OF THE MAIN STUDY CFD OPTIMIZATION SIMULATIONS

This chapter presents the results of the CFD simulations used for the determination of the optimal regenerative cooling system design configuration for the cSETR 50lbf engine. Four representations are provided: one for general performance characteristics, the second for performance between n_c, the third for performance between geometry, and the forth provides a real gas assessment. An analysis and discussion are also given of the results as they relate to material limits and literature values. From the analysis, an indication of the optimal n_c from the studied values, 22 to 37, can be found.

5.1 General Performance Characteristics

The CFD post graphics shown in Figures 5-1 to 5-5 show the results of one channel which represents the results of all channels. Each channel provided similar results as only small changes were made for each n_c, requiring a more detailed numerical analysis. It was found that the convection and radiation outer shell boundary conditions furthermore gave similar results, which confirms the use of the radiation boundary condition as well as depicts a simulation design that will perform well in the vacuum of outer space.

Figures 5-1 and 5-2 show that the temperature and heat flux variation peaks at the throat location as expected due to the use of the Bartz equation for the variation in heat transfer coefficient along the hot-wall (bottom-wall-bottom). Also, the heat flux values are as expected for the sign convention that positive values represent inward flux (as in the case of the bottom-

wall-bottom where heat is moving from the external combustion into the wall), and negative values represent outward flux (as in the case of the top-wall-top where heat is moving from the internal geometry to the external domain away from the engine).

The variation of fluid density is shown in overview in Figure 5-3, and at multiple lengthwise locations along the heated section of the channel in Figure 5-4, with the solid domains also in the images. The density images are provided as a means to give approximate locations of phase change along the channel for future researchers utilizing the real-gas fluid model, as the ideal gas model used in the present research can not depict the change accurately. Also, the density images all show the solid regions at one homogeneous value, as expected for the software used. As explained in [47], [48], and [51], only heat conduction is solved for solid domains in FLUENT, leaving density or stress calculations for a separate specialized software tool.

The variation of fluid static temperature is shown at the same multiple lengthwise locations as for the density, in Figure 5-5. The solid domains in these images show a reasonable variation in temperature, hottest at the hot-wall and coolest at the top-wall-top (of Figure 4-7), matching at the fluid interfaces. Unfortunately, the temperature variation in the solids is not as dramatic as shown in other works like [33], likely due to the small number of cells available after filling the fluid domain, which may effect the CFD modeled heat transfer into the channel. The locations of highest temperature also provide the approximate locations of likely phase change.

The fluid temperature and density variation along the channel length clearly shows the benefit of using a robust but generalized CFD software package such as FLUENT when compared to the results of [8] and [50], which do not show the boundary or corner effects at the top of the channel in their proprietary code results.

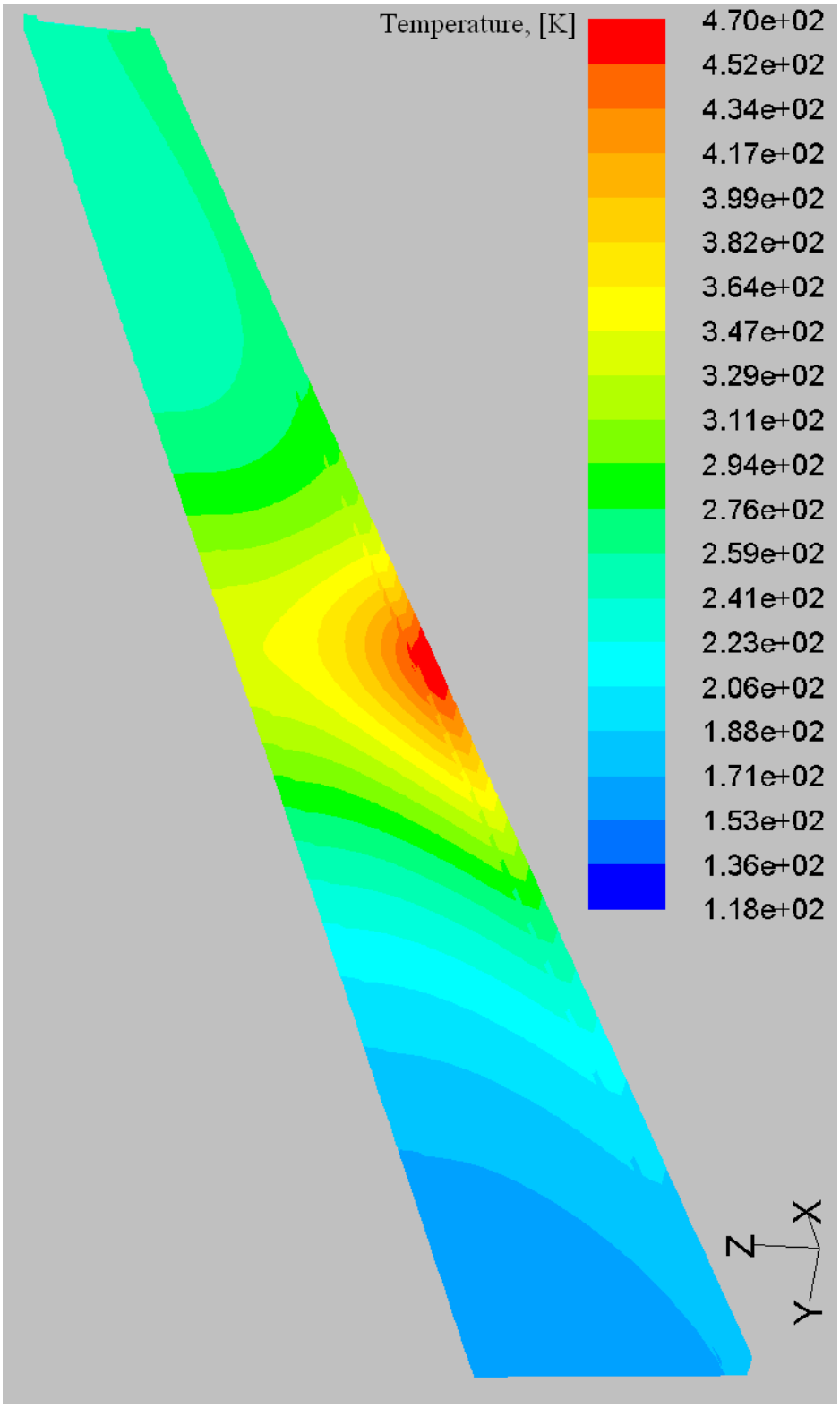

Figure 5-1: Overview of the temperature variation in the solid domains of a representative channel at the heated section.

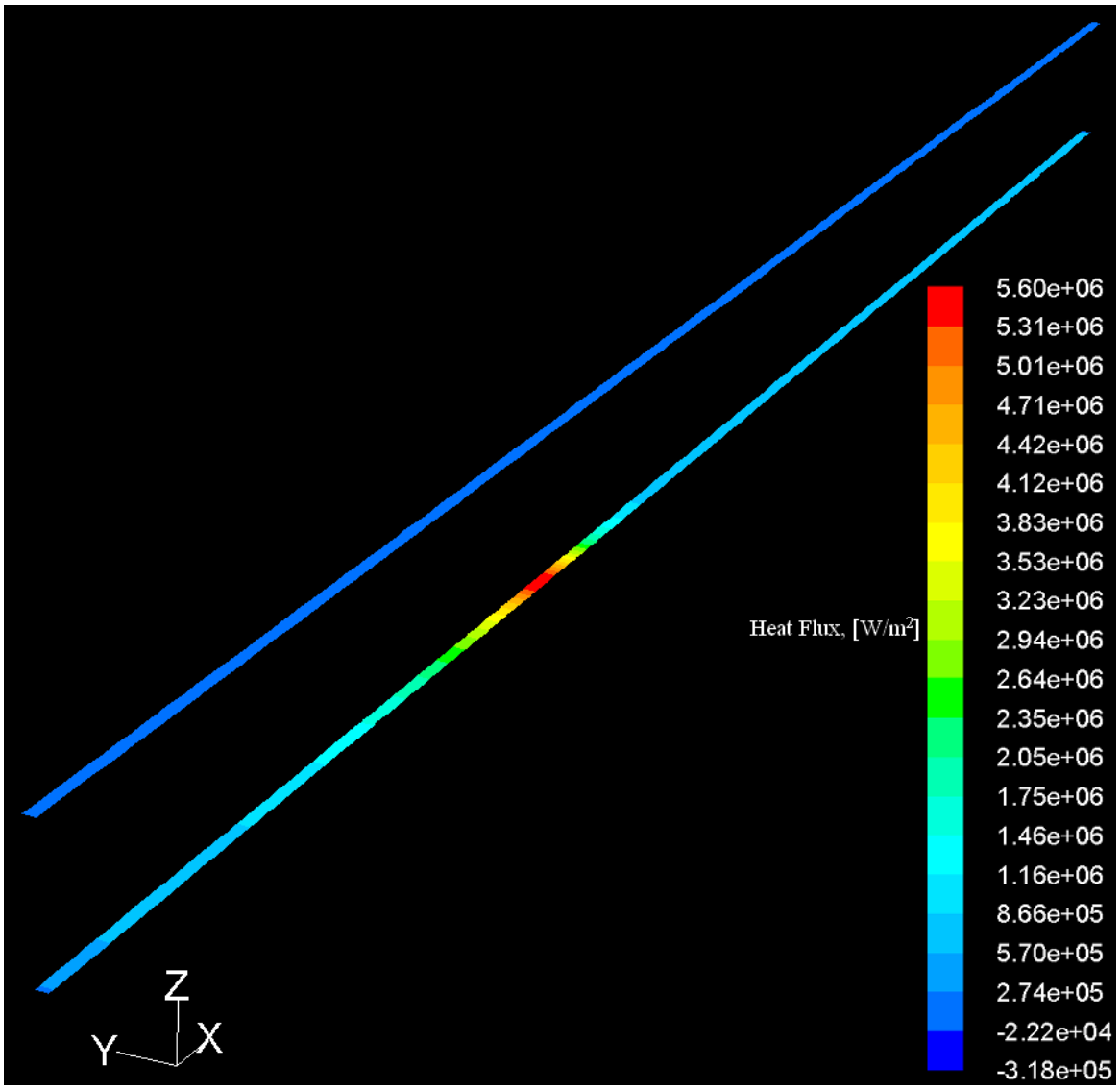

Figure 5-2: Overview of the heat flux variation on the bottom-wall-bottom (lower) and top-wall-top (upper) of a representative channel at the heated section.

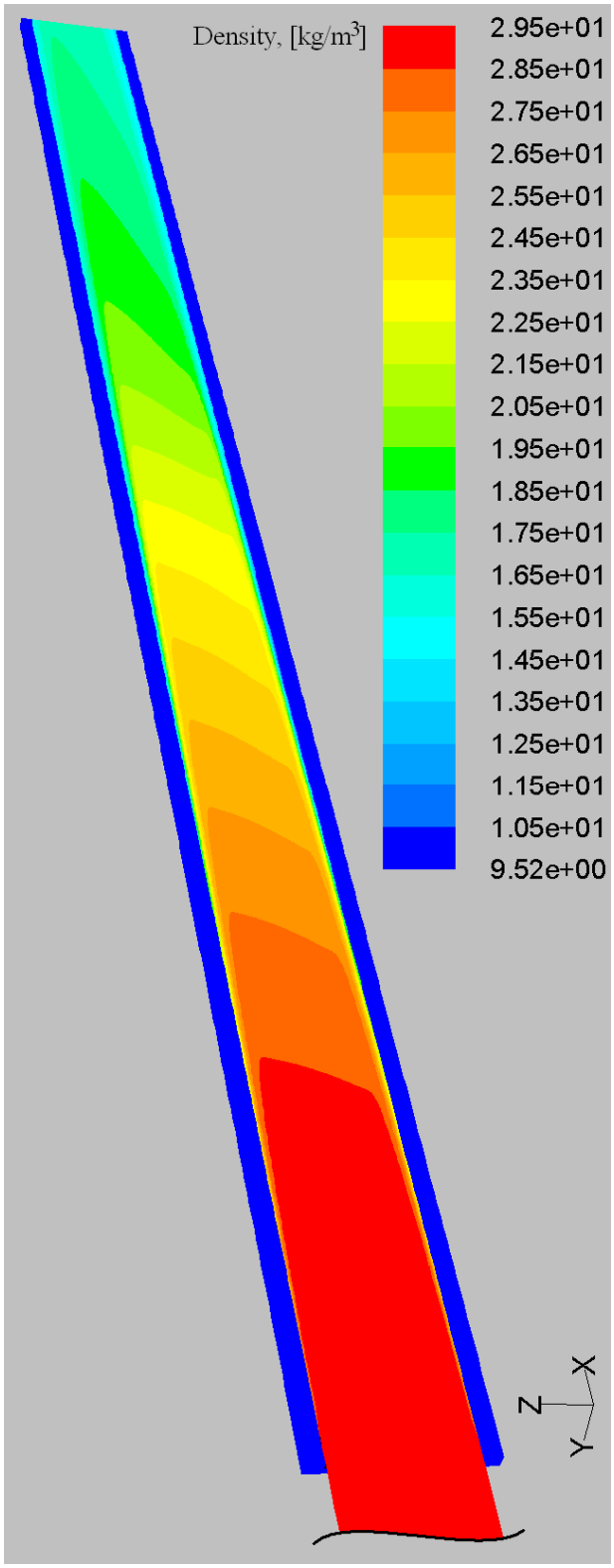

Figure 5-3: Overview of the density variation in the fluid domain of a representative channel at the heated section. The dark blue areas are the constant density solid domains.

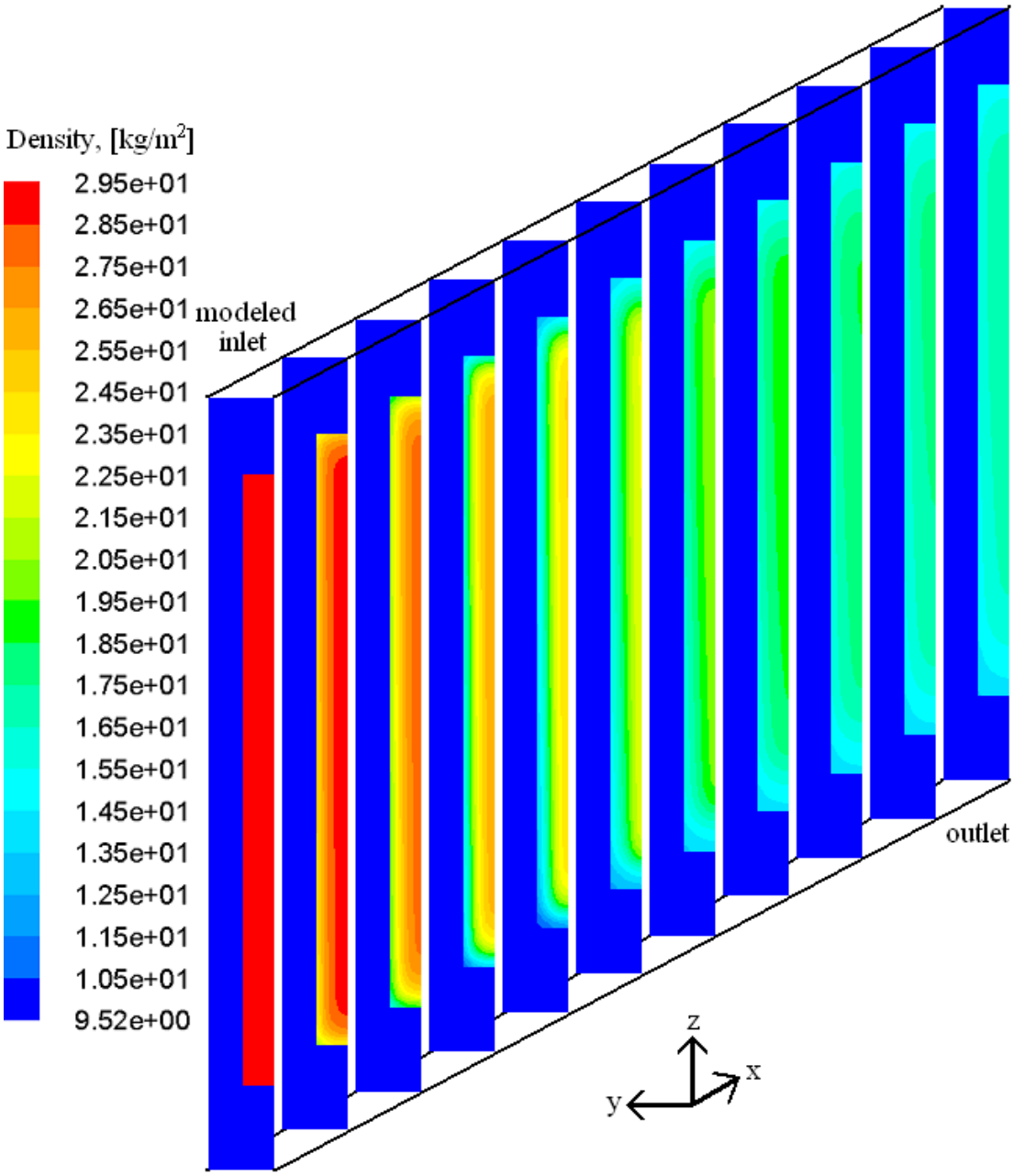

Figure 5-4: Variation of fluid density at multiple lengthwise locations along the heated section of a representative channel, between the modeled inlet and the outlet, with adjacent solid values.

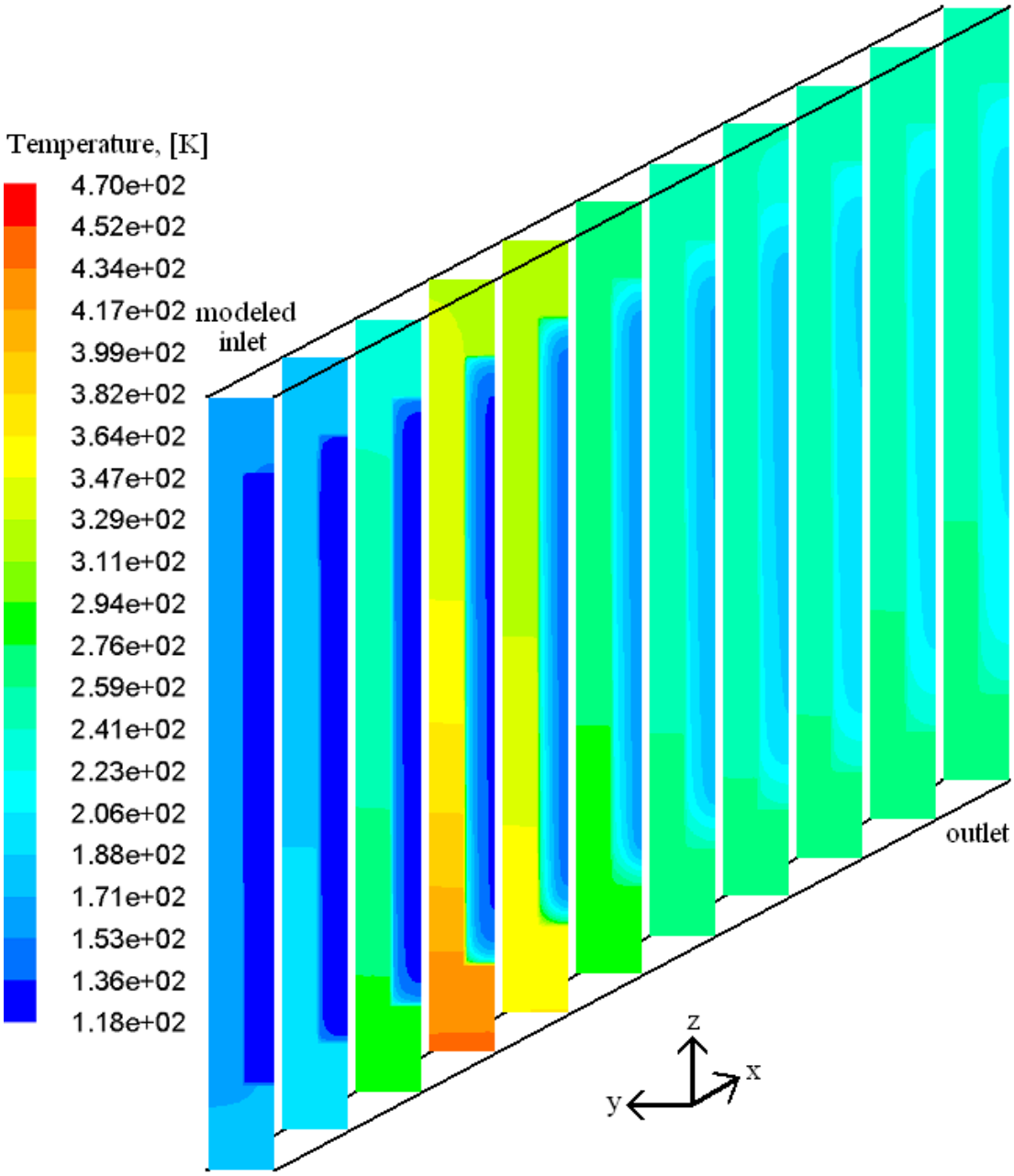

Figure 5-5: Variation of fluid temperature at multiple lengthwise locations along the heated section of a representative channel, between the modeled inlet and outlet, with adjacent solid values.

5.2 Performance Considering n_c

The solution data for various values on the multiple 2D wall zones shown in Figure 4-7, as well as for the modeled inlet and channel outlet, are exported from FLUENT in numerical format after the simulations are completed. The data is then imported into a numerical spreadsheet software for direct use, manipulation using the second order numerical differencing methods of [53] and [54], and graphical trend analysis.

Values of particular interest on the wall zones are the maximum temperature, and maximum and average total surface heat flux. For the heated channel section of interest, between the modeled inlet and the outlet, the important values are the coolant average total pressure, average lengthwise *x* velocity, and average static temperature.

The flow values are manipulated to find the channel pressure drop, velocity increase (an indication of possible phase change when using real gas), and temperature increase as an indication of cooling performance. The average total surface heat flux on the walls surrounding the fluid are combined to determine a net heat flux inward to the coolant, also as an indication of cooling performance. Graphing these values for each n_c allows a trend analysis to be performed between each n_c, as the data indicate that there is no clear-cut "best solution" n_c as found by [33] when their direct solution data showed a maximum or minimum of a particular quantity at a particular channel number. The limited range of n_c in the present research requires a more thorough analysis than simple raw data.

It was found that the convection and radiation outer shell boundary conditions gave similar numerical results, differing by only a tiny percentage, therefore only the convection results are shown in Figures 5-6 through 5-22.

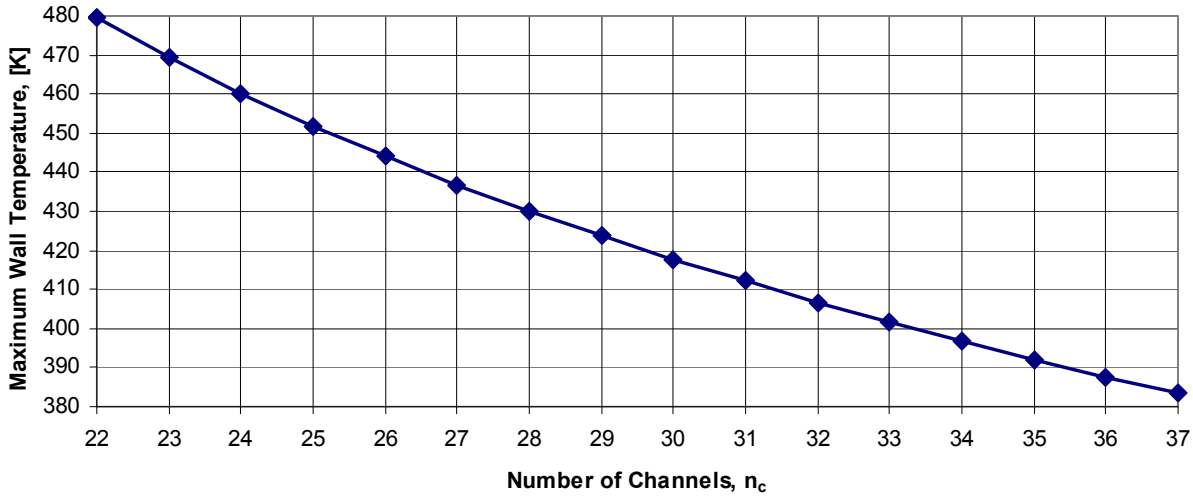

Figure 5-6: Maximum wall temperatures on the bottom-wall-bottom (hot-wall) 2D wall zone for channel models n_c.

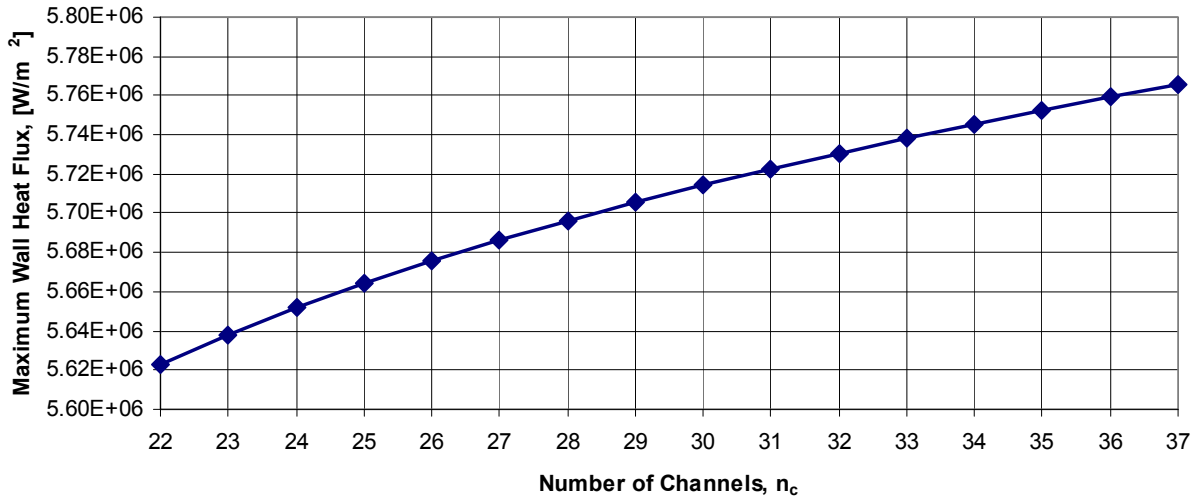

Figure 5-7: Maximum wall heat flux values on the bottom-wall-bottom (hot-wall) 2D wall zone for channel models n_c.

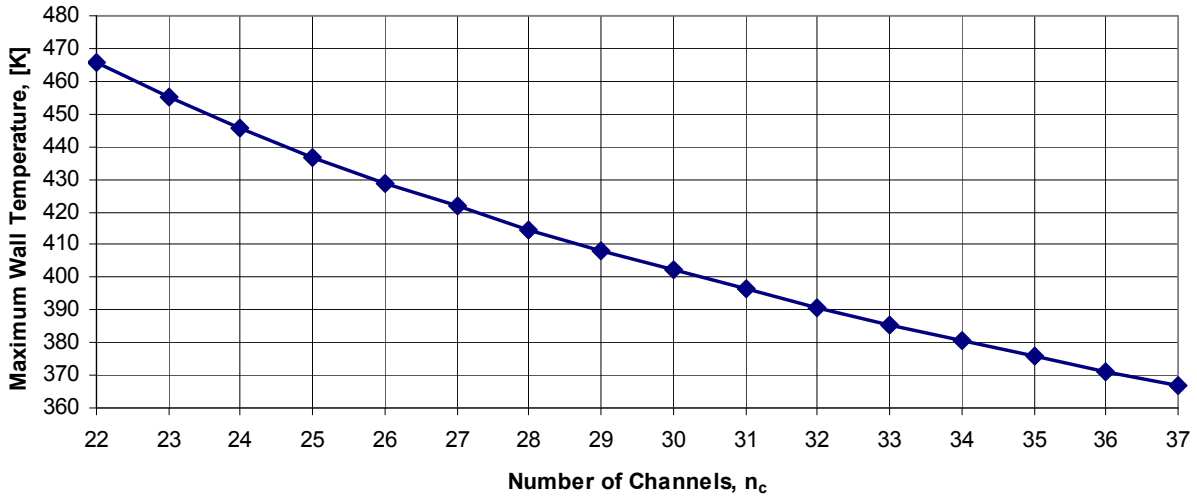

Figure 5-8: Maximum wall temperatures on the channel-bottom 2D wall zone for channel models n_c.

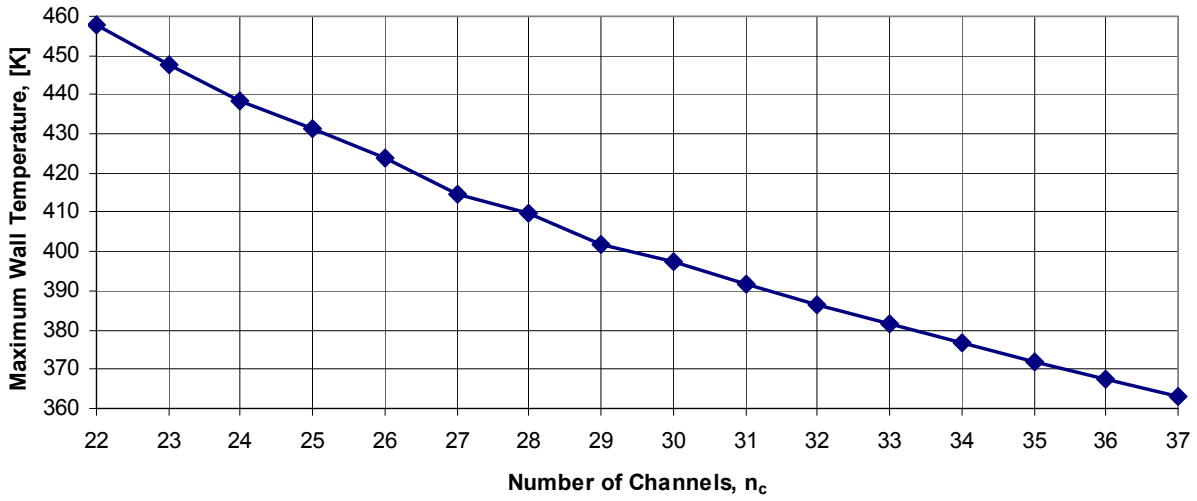

Figure 5-9: Maximum wall temperatures on the channel-left 2D wall zone for channel models n_c.

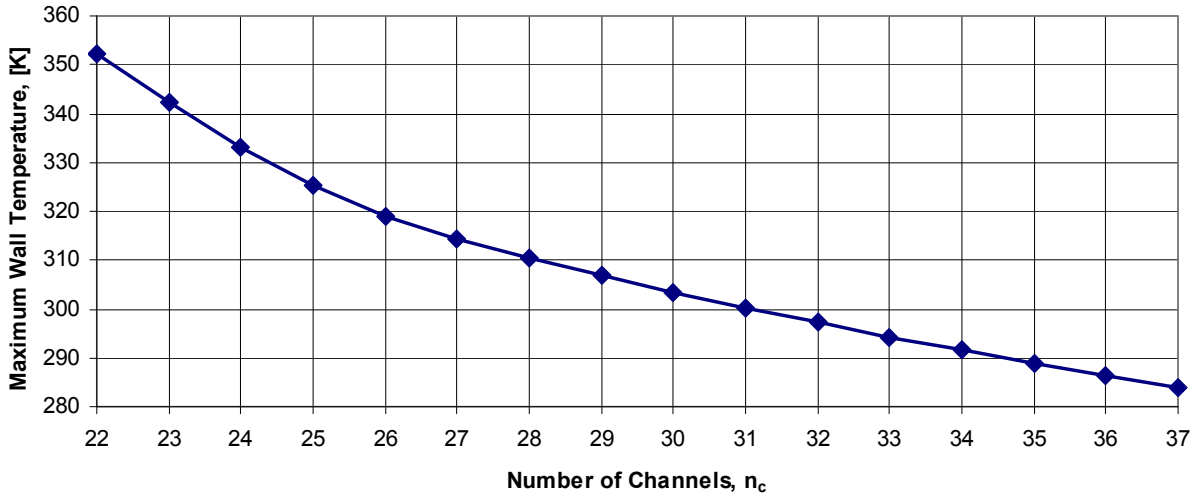

Figure 5-10: Maximum wall temperatures on the top-wall-top 2D wall zone for channel models n_c.

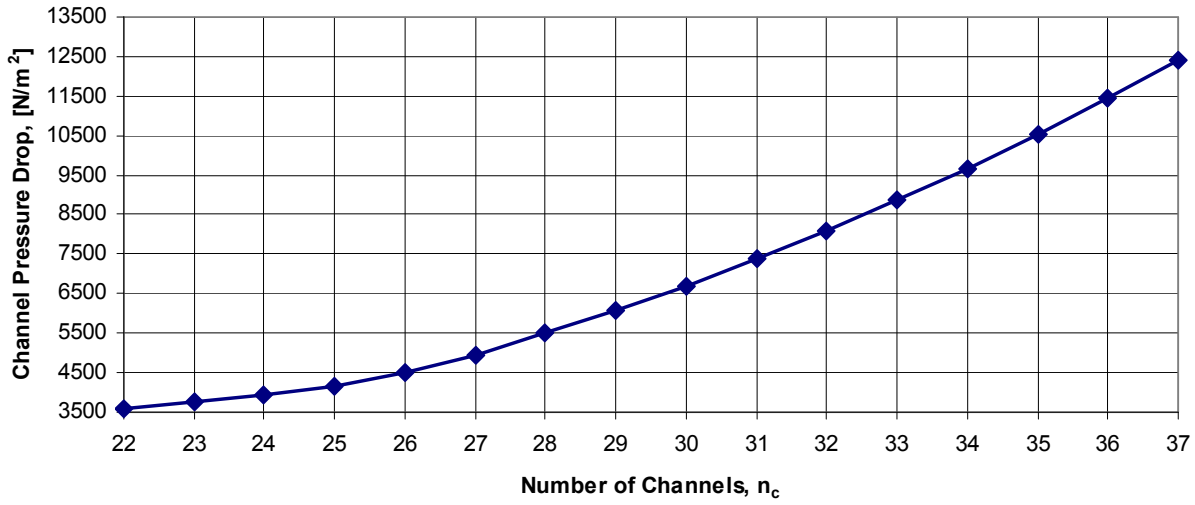

Figure 5-11: Channel pressure drops between the modeled-inlet and the outlet for channel models n_c.

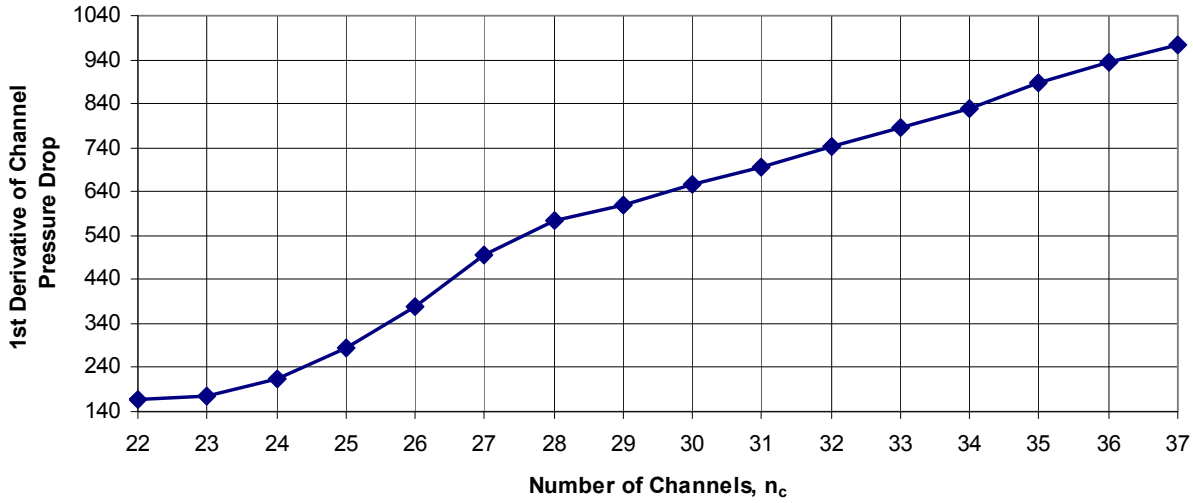

Figure 5-12: First derivatives of the channel pressure drops between the modeled-inlet and the outlet for channel models n_c.

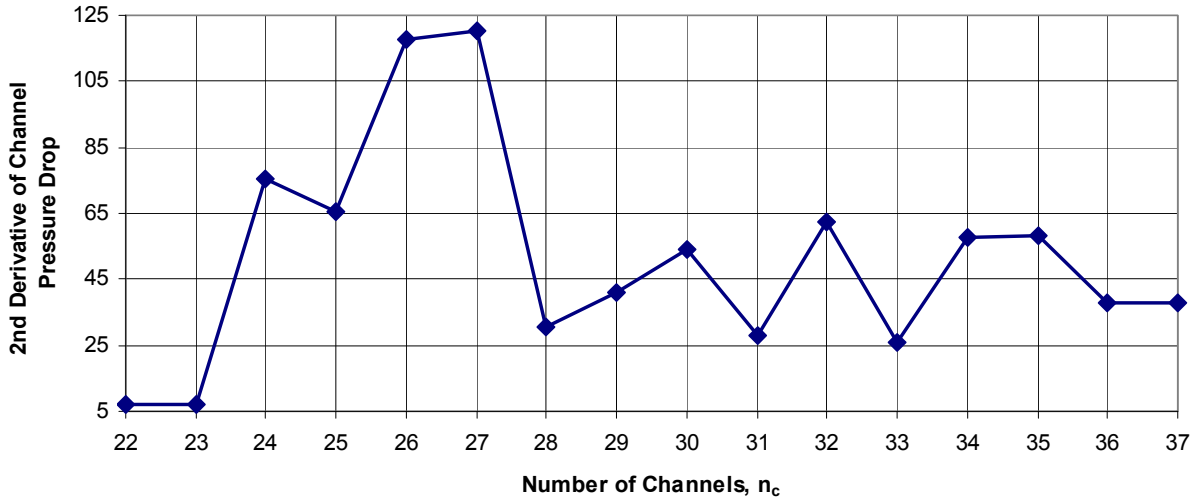

Figure 5-13: Second derivatives of the channel pressure drops between the modeled-inlet and the outlet for channel models n_c.

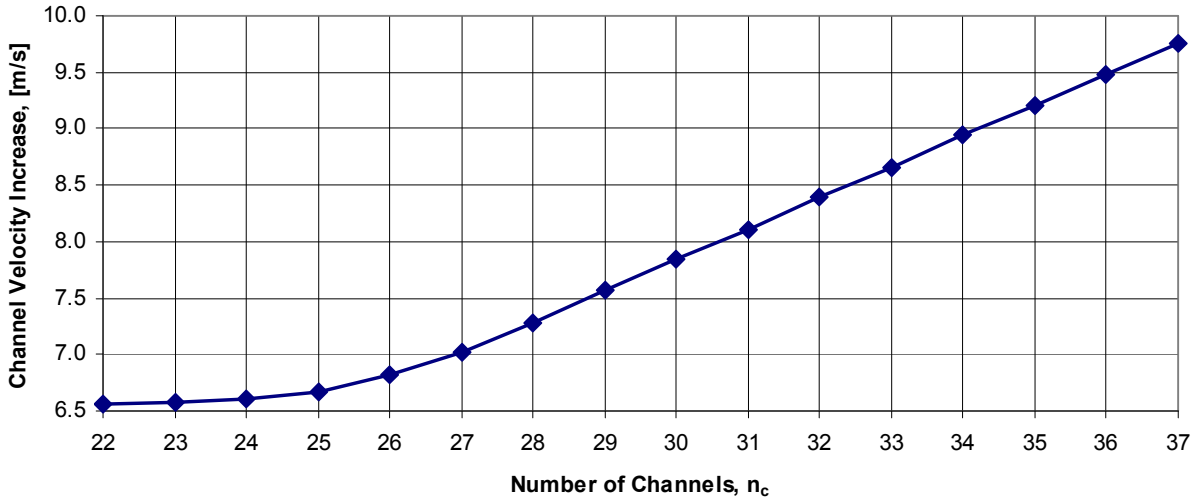

Figure 5-14: Channel velocity increases between the modeled-inlet and the outlet for channel models n_c.

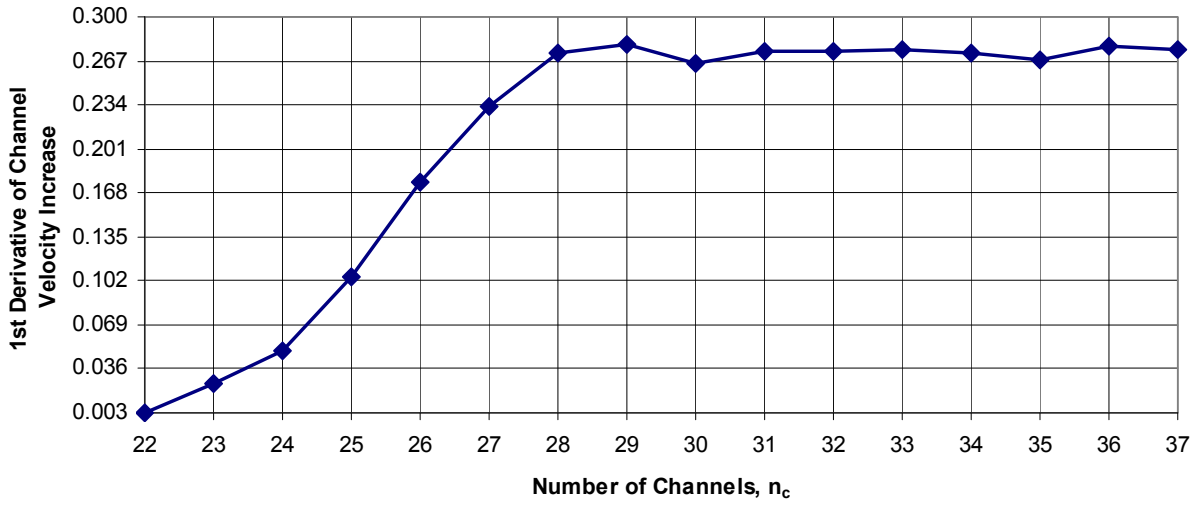

Figure 5-15: First derivatives of the channel velocity increases between the modeled-inlet and the outlet for channel models n_c.

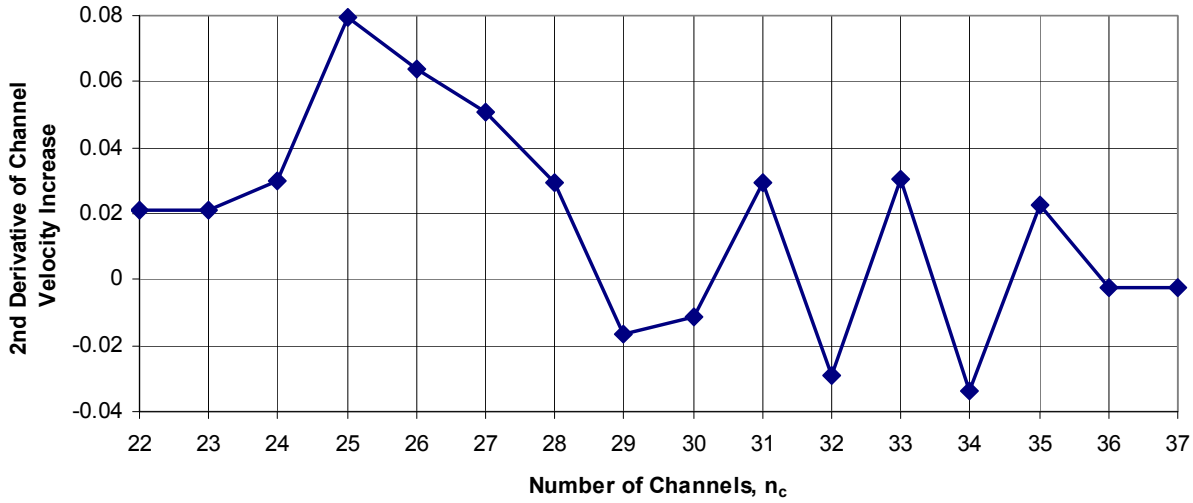

Figure 5-16: Second derivatives of the channel velocity increases between the modeled-inlet and the outlet for channel models n_c.

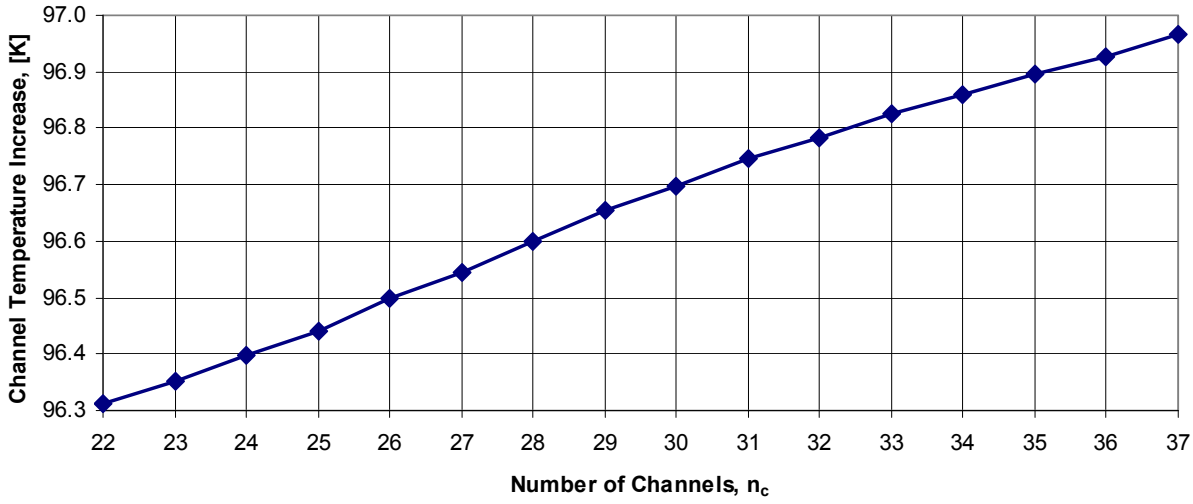

Figure 5-17: Channel coolant temperature increases between the modeled-inlet and the outlet for channel models n_c.

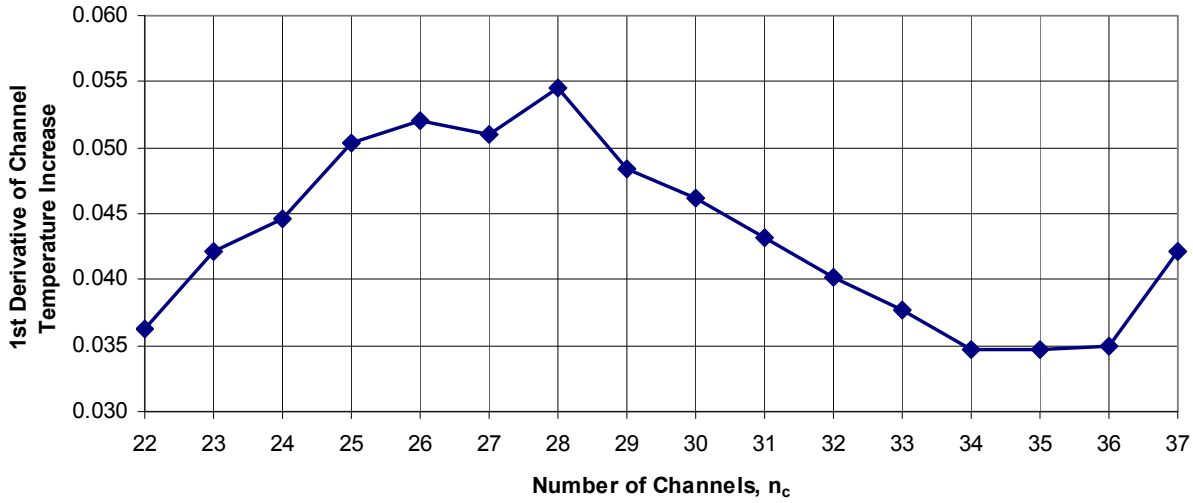

Figure 5-18: First derivatives of the channel temperature increases between the modeled-inlet and the outlet for channel models n_c.

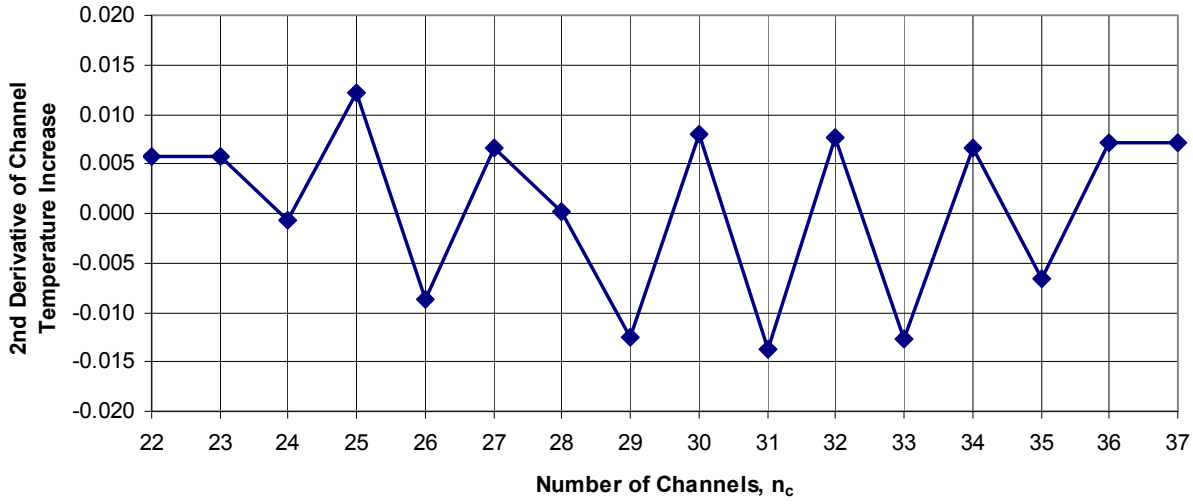

Figure 5-19: Second derivatives of the channel temperature increases between the modeled-inlet and the outlet for channel models n_c.

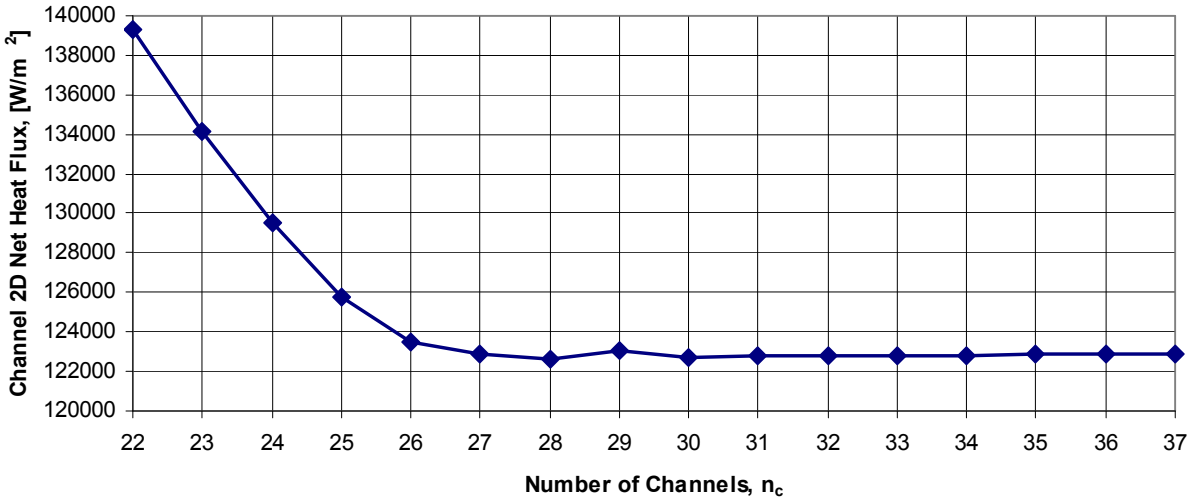

Figure 5-20: Net heat flux quantities entering the channel through the surrounding 2D walls for channel models n_c.

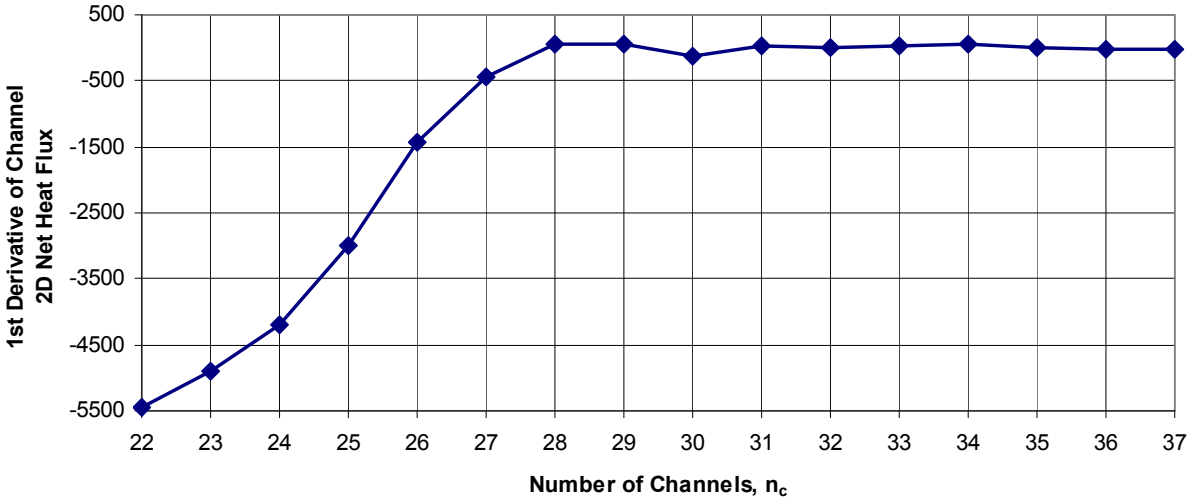

Figure 5-21: First derivative of the net heat flux quantities entering the channel through the surrounding 2D walls for channel models n_c.

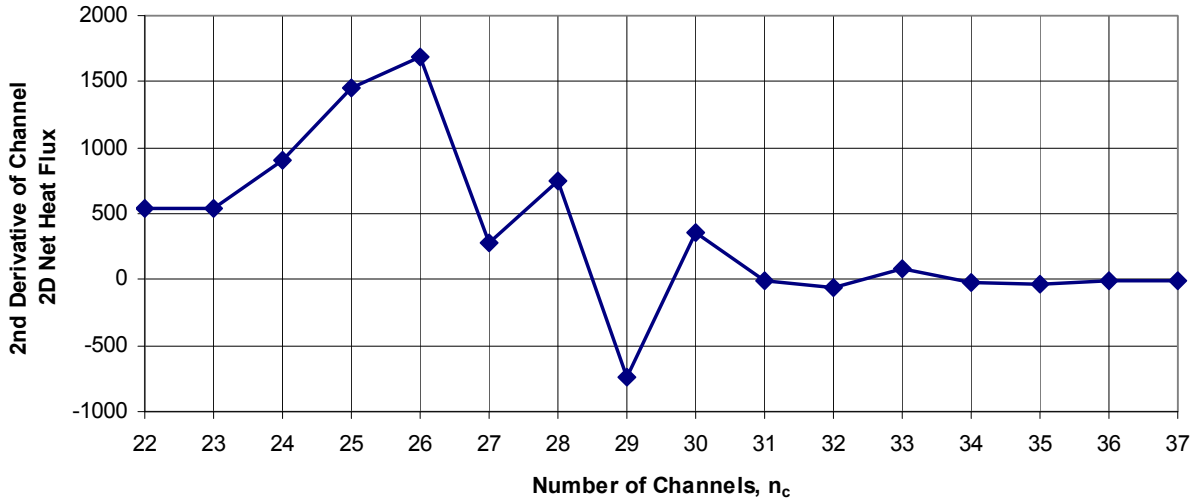

Figure 5-22: Second derivative of the net heat flux quantities entering the channel through the surrounding 2D walls for channel models n_c.

Studying the results shown in Figures 5-6 through 5-22 gives an indication of the best channel configurations for the cSETR 50lbf engine. Because there are no apparent minimums or maximums in the FLUENT raw data, numerical differencing derivatives are used to show how the raw data changes when n_c is increased from 22 to 37. Channels 28 to 34 show particular promise as the 2nd derivative of the channel pressure drop finds a minimum, indicating that for $n_c < 28$ the pressure drop has not become stabilized, and viewing the 1st derivative that for $n_c > 28$ little added benefit is found by using more channels. Furthermore, the actual channel pressure drops for $n_c = 28$ or 29 are in the lower third of all channel pressure drops. It is noted that the minimum allowable channel outlet pressure condition of Table 4-12 is met.

At $n_c = 28$, the 1st derivative of channel velocity increase levels off to indicate that velocity has stabilized, and with the 2nd derivative reaching a local minimum at $n_c = 29$, shows little added benefit in using more channels.

The channel temperature increase is an indication of the cooling performance, whereby a

higher value shows that more heat is extracted from the solid regions. The 1st derivative of channel temperature increase is maximum at n_c = 28, showing that although the actual temperature increase is higher for higher n_c there is little added benefit. The 2nd derivative of channel temperature increase does not allow for conclusive results.

Perhaps the best indication of cooling performance is the net heat flux into the coolant. A 2D idealization is used since the inlet and outlet fluid heat flux values are not given directly by FLUENT. The net heat flux uses the average heat flux values through the three surrounding 2D walls, by adding the flux entering through the channel-bottom and channel-left, while subtracting the flux exiting through the wall at the top of the channel. Again, channels 28 to 34 are discovered as most beneficial. The net heat flux and 1st derivative level off at n_c = 28, with a 2nd derivative minimum at n_c = 29. The 2nd derivative minimum indicates that little added benefit is found if other channel configurations are used.

Comparing the maximum wall temperatures for n_c = 29 to Tables 2-5 and 2-6 and the information from [16] shows that the material limits are not reached and are lower than assumed for previous calculations. However, the average outlet temperature of 215 K for methane is much lower than the experimental values given in literature.

5.3 Performance Considering Geometry Features

In a more general sense, Figures 5-23 through 5-41 show the geometry and simulation data in terms of the channel aspect ratio and the hydraulic diameter.

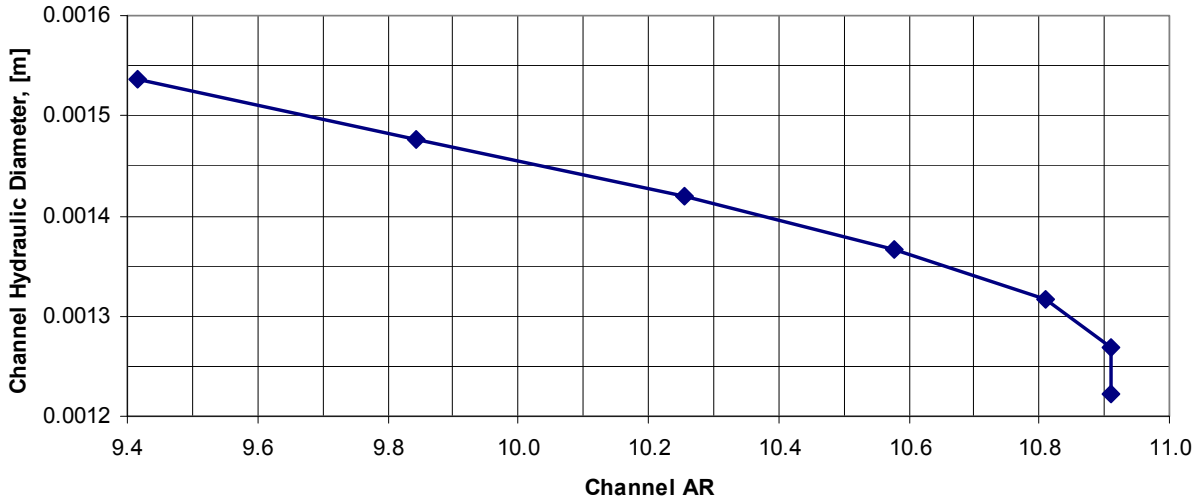

Figure 5-23: Channel hydraulic diameters for the range of aspect ratios considered.

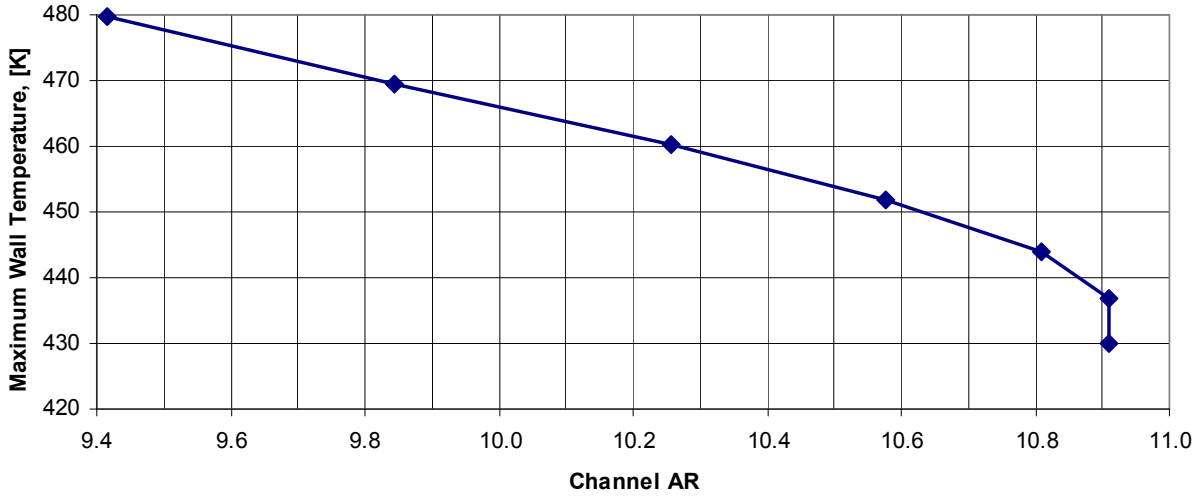

Figure 5-24: Maximum wall temperature on the bottom-wall-bottom (hot-wall) 2D wall zone for the range of aspect ratios considered.

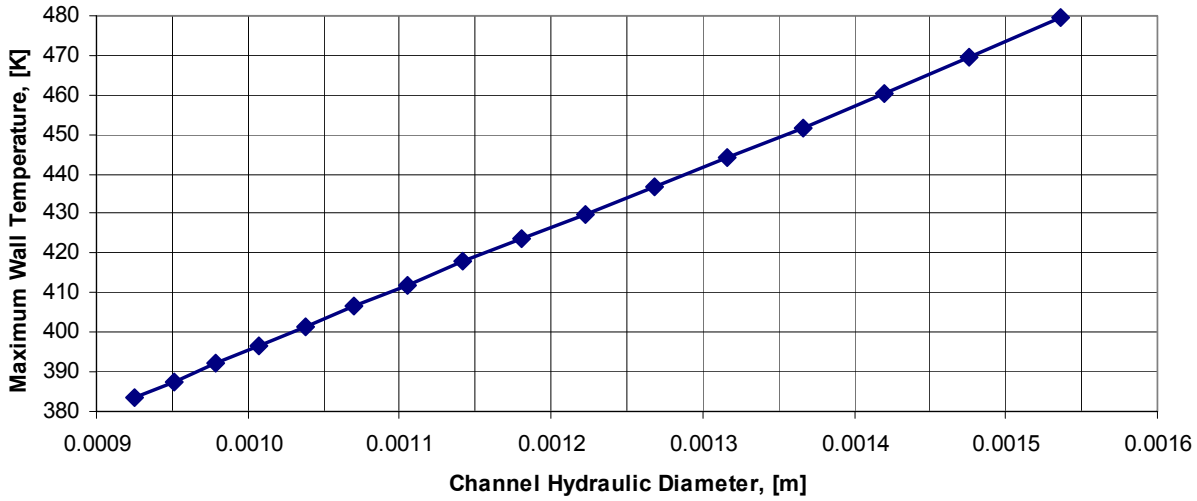

Figure 5-25: Maximum wall temperature on the bottom-wall-bottom (hot-wall) 2D wall zone for the range of hydraulic diameters considered.

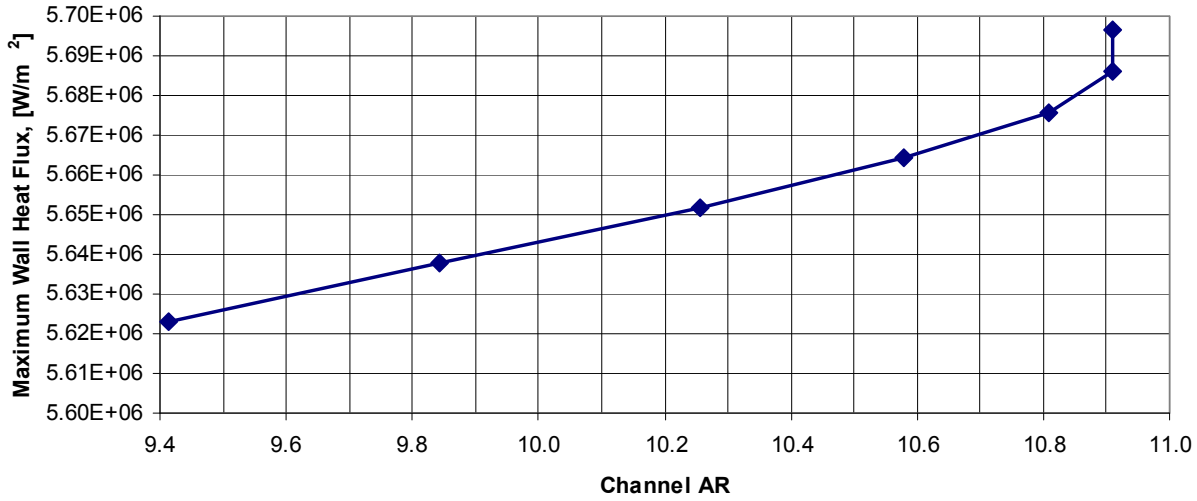

Figure 5-26: Maximum wall heat flux on the bottom-wall-bottom (hot-wall) 2D wall zone for the range of aspect ratios considered..

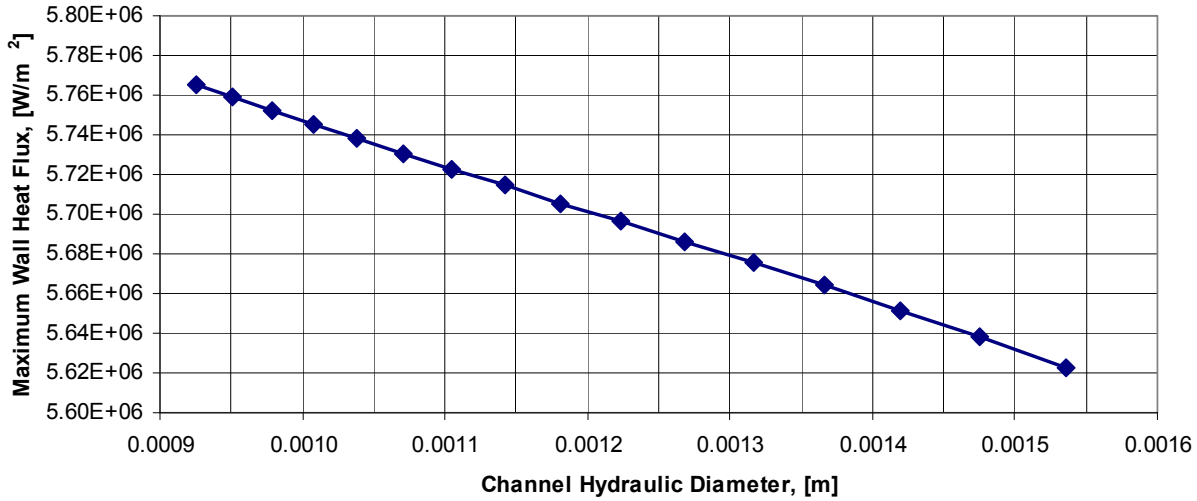

Figure 5-27: Maximum wall heat flux on the bottom-wall-bottom (hot-wall) 2D wall zone for the range of hydraulic diameters considered.

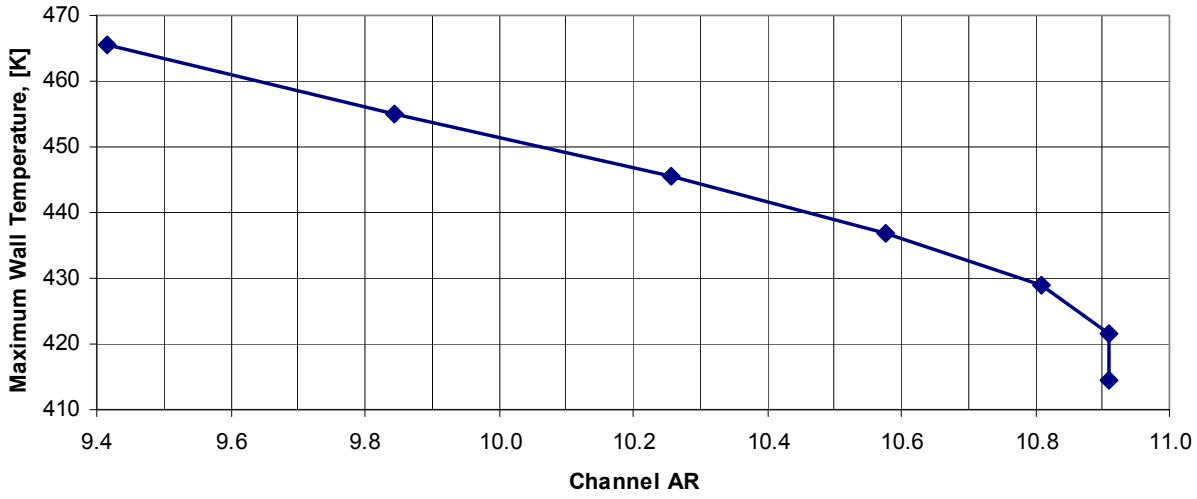

Figure 5-28: Maximum wall temperature on the channel-bottom 2D wall zone for the range of aspect ratios considered..

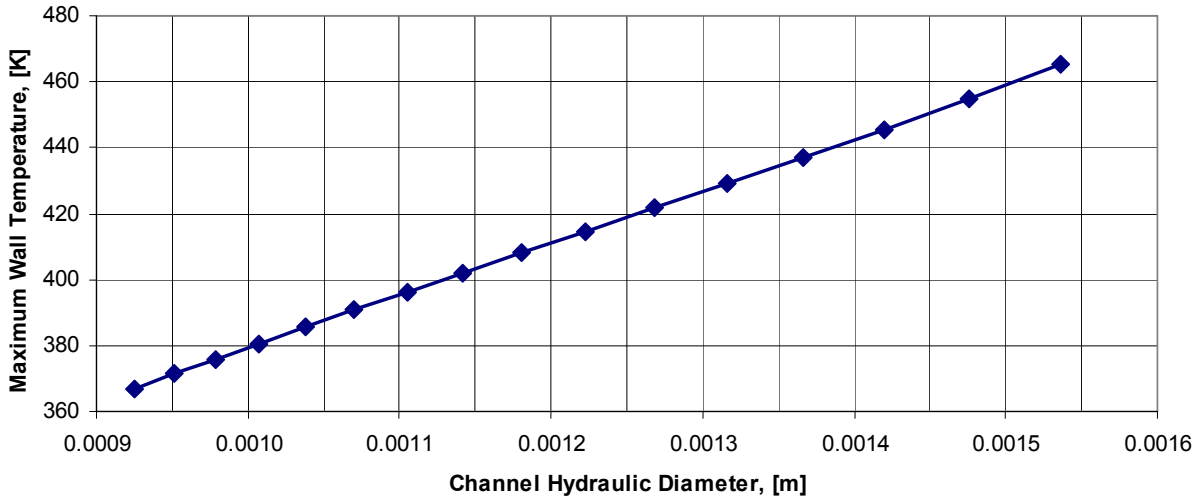

Figure 5-29: Maximum wall temperature on the channel-bottom 2D wall zone for the range of hydraulic diameters considered.

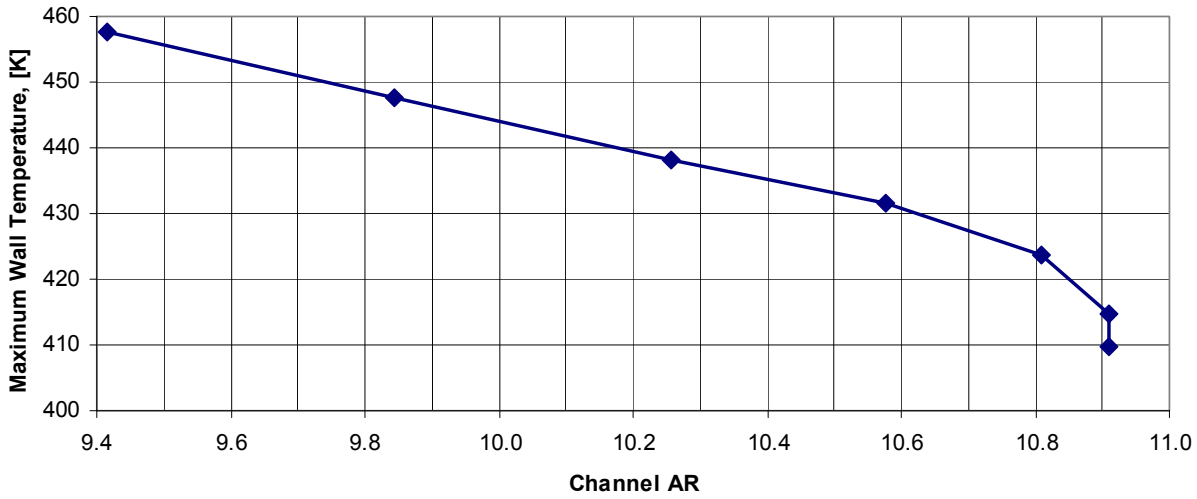

Figure 5-30: Maximum wall temperature on the channel-left 2D wall zone for the range of aspect ratios considered..

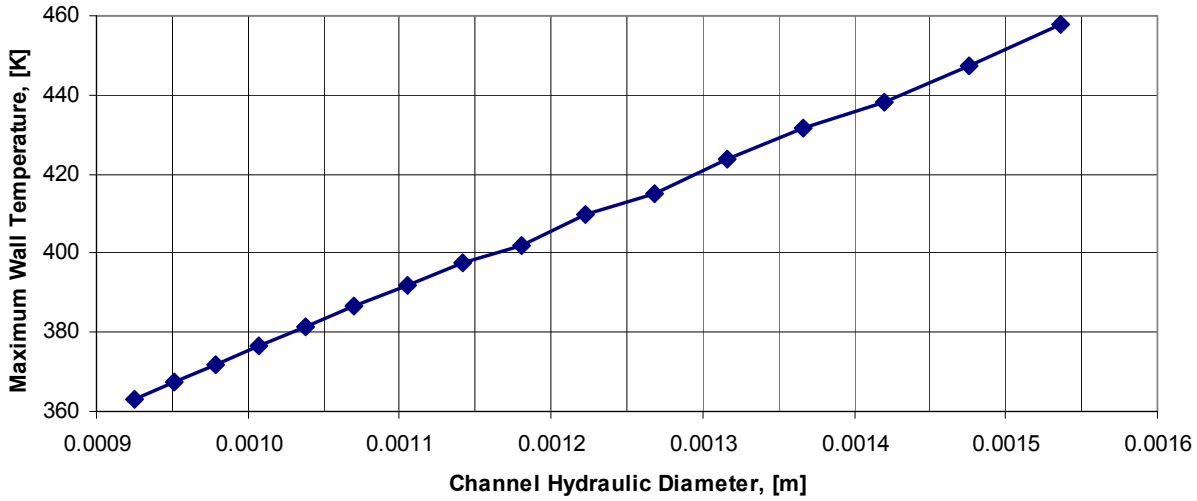

Figure 5-31: Maximum wall temperature on the channel-left 2D wall zone for the range of hydraulic diameters considered.

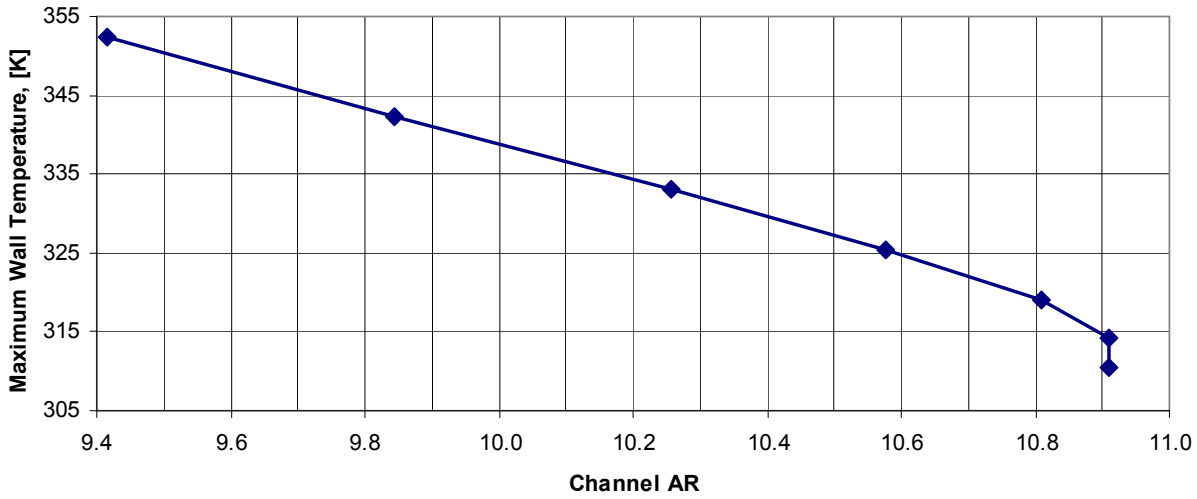

Figure 5-32: Maximum wall temperature on the top-wall-top 2D wall zone for the range of aspect ratios considered.

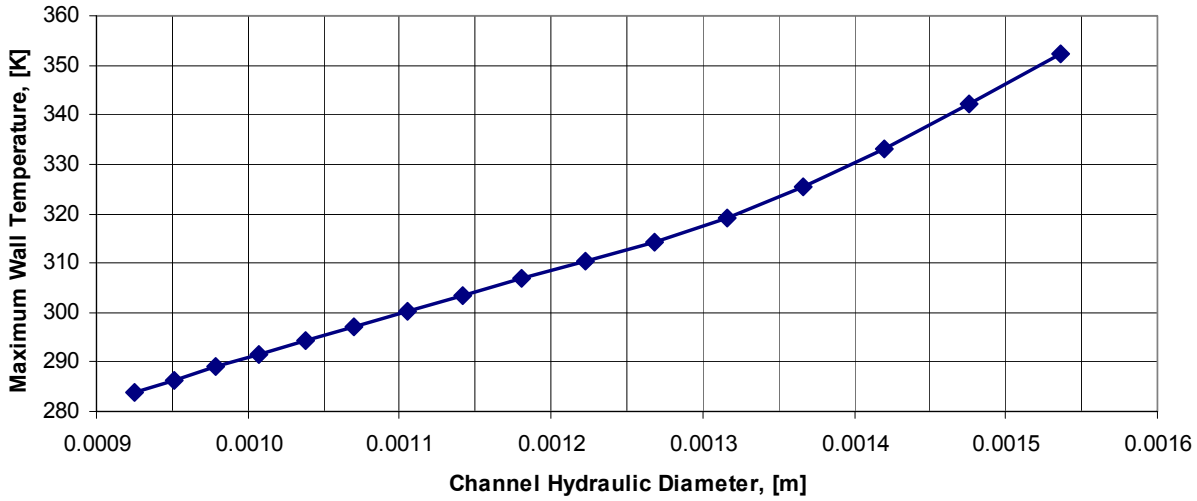

Figure 5-33: Maximum wall temperature on the top-wall-top 2D wall zone for the range of hydraulic diameters considered.

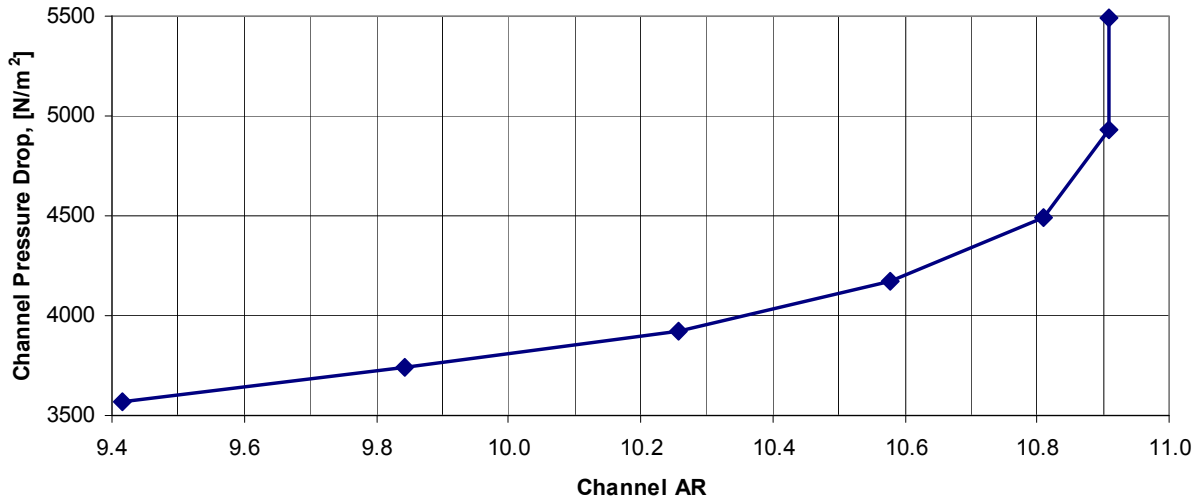

Figure 5-34: Channel pressure drop between the modeled-inlet and the outlet for the range of aspect ratios considered.

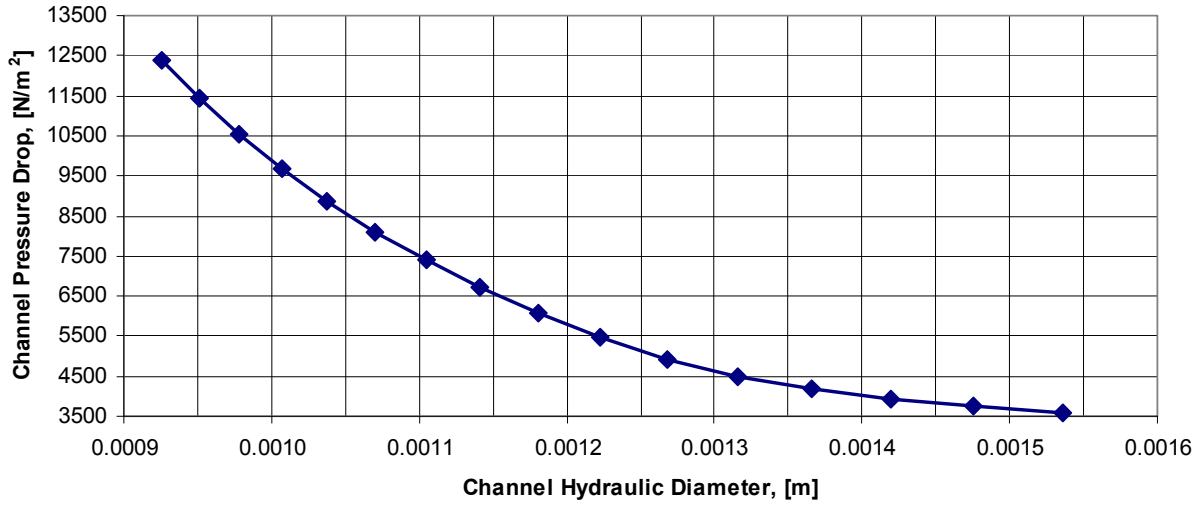

Figure 5-35: Channel pressure drop between the modeled-inlet and the outlet for the range of hydraulic diameters considered.

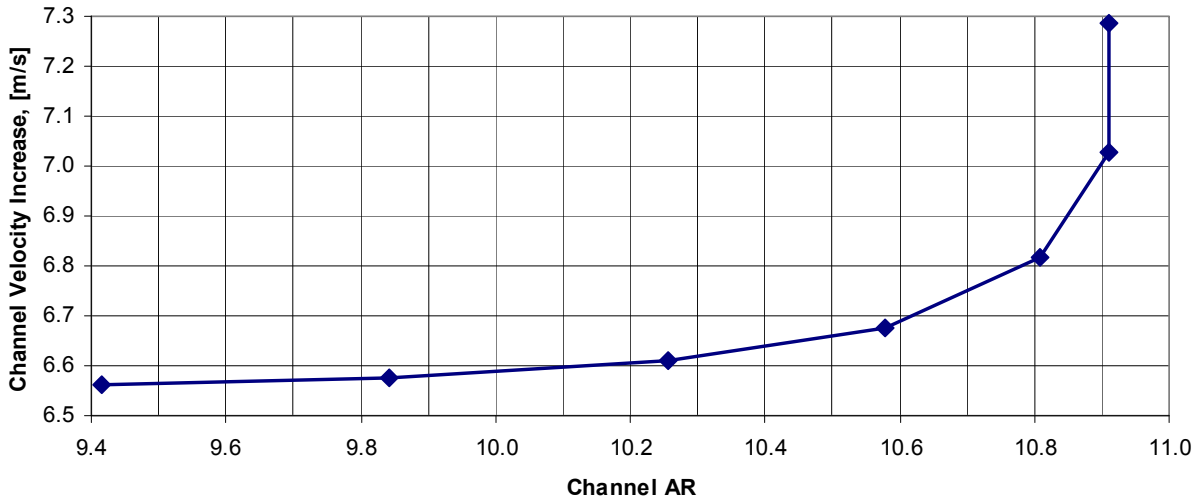

Figure 5-36: Channel velocity increase between the modeled-inlet and the outlet for the range of aspect ratios considered.

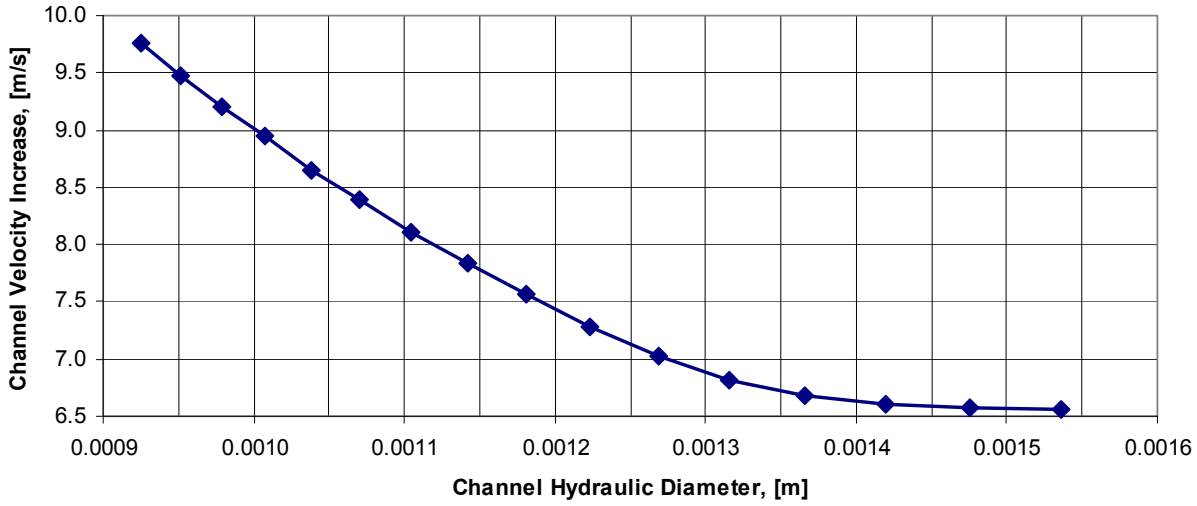

Figure 5-37: Channel velocity increase between the modeled-inlet and the outlet for the range of hydraulic diameters considered.

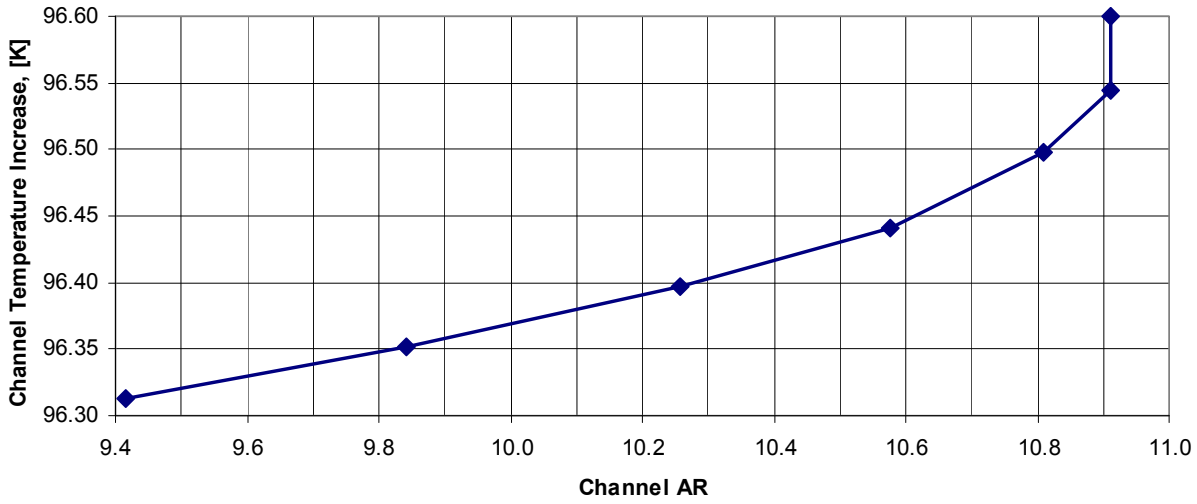

Figure 5-38: Channel temperature increase between the modeled-inlet and the outlet for the range of aspect ratios considered.

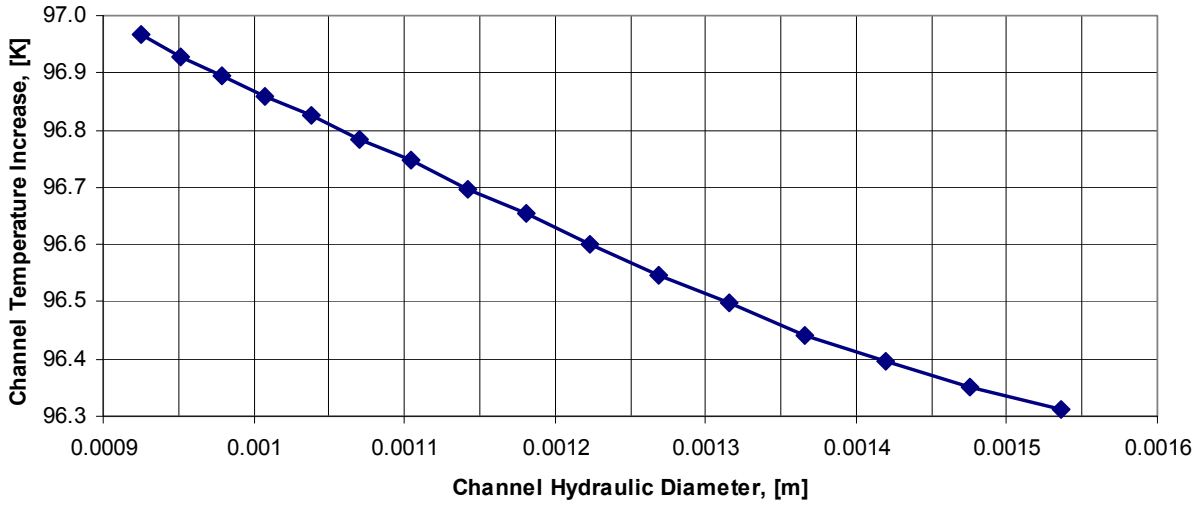

Figure 5-39: Channel temperature increase between the modeled-inlet and the outlet for the range of hydraulic diameters considered.

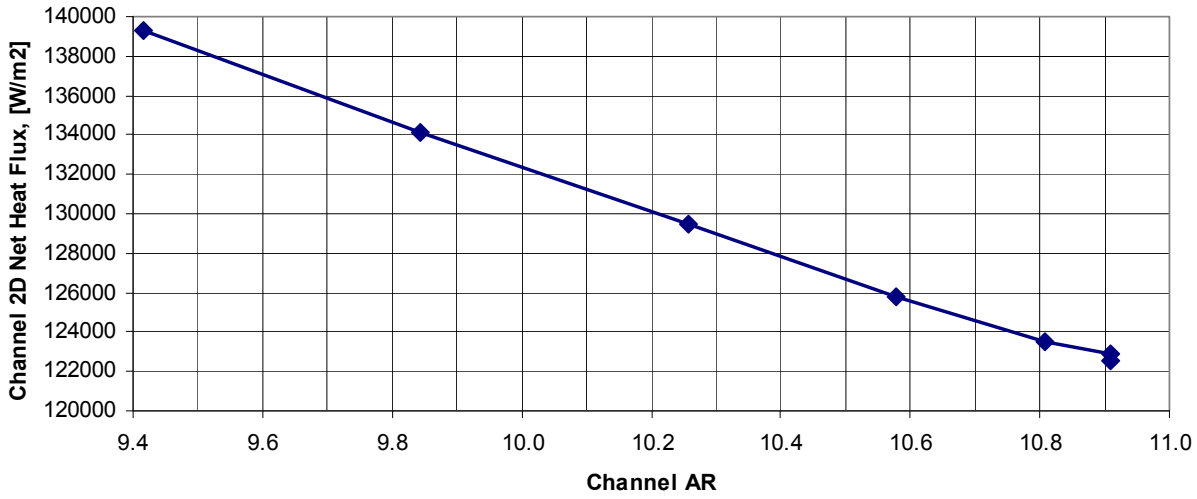

Figure 5-40: Net heat flux quantities entering the channel through the surrounding 2D walls for the range of aspect ratios considered.

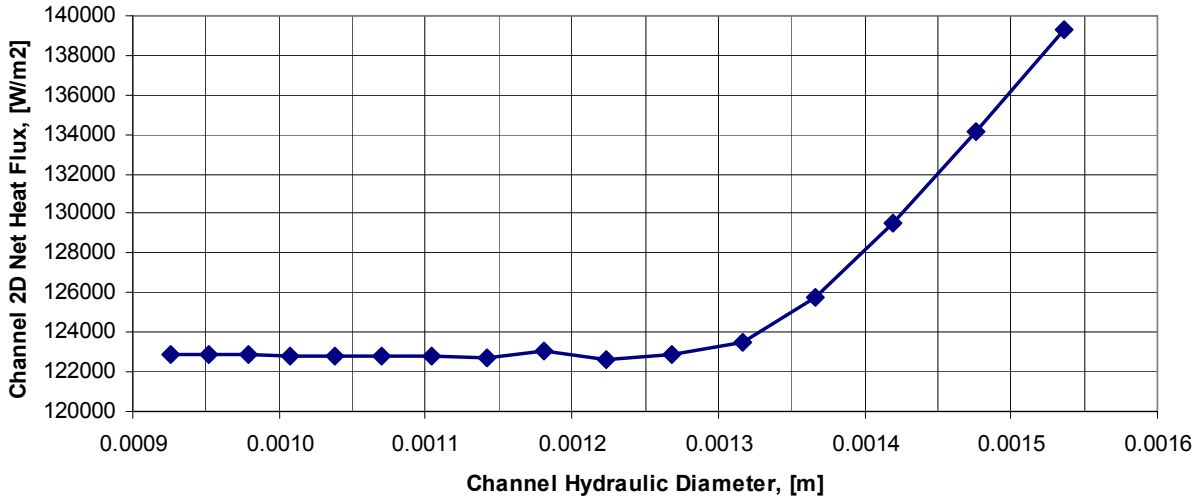

Figure 5-41: Net heat flux quantities entering the channel through the surrounding 2D walls for the range of hydraulic diameters considered.

5.4 Relating Ideal and Real Gas Behavior

A 20 point line rake of the fluid data is taken for n_c = 29 running ideal gas between the modeled-inlet and the outlet along a diagonal in order to compare the pressure, temperature, and density CFD results with the ideal gas equation of state, and real gas behavior. The data results in a 0.002% average difference between the FLUENT result densities and the densities calculated using the ideal gas equation of state with the FLUENT molecular weight from Table 2-17, and a universal gas constant of 8.31451 J/mol-K.

Another 20 point line rake is taken for n_c = 29 running the NIST Real Gas Model option in FLUENT for methane. In order to obtain data for a real gas simulation, the channel inlet temperature must be artificially increased to a value beyond the phase change transition value determining liquid to vapor at the running pressure, to 175 K. The simulation must only be performed in one phase region due to the limitations outlined in [48]. A real gas model which can begin at the required 118 K remains desirable.

The range of the data found is plotted in Figure 5-42, on top of the real gas state diagram from [55] and shows the similarity with Figure 1-9, and the expected phase change behavior.

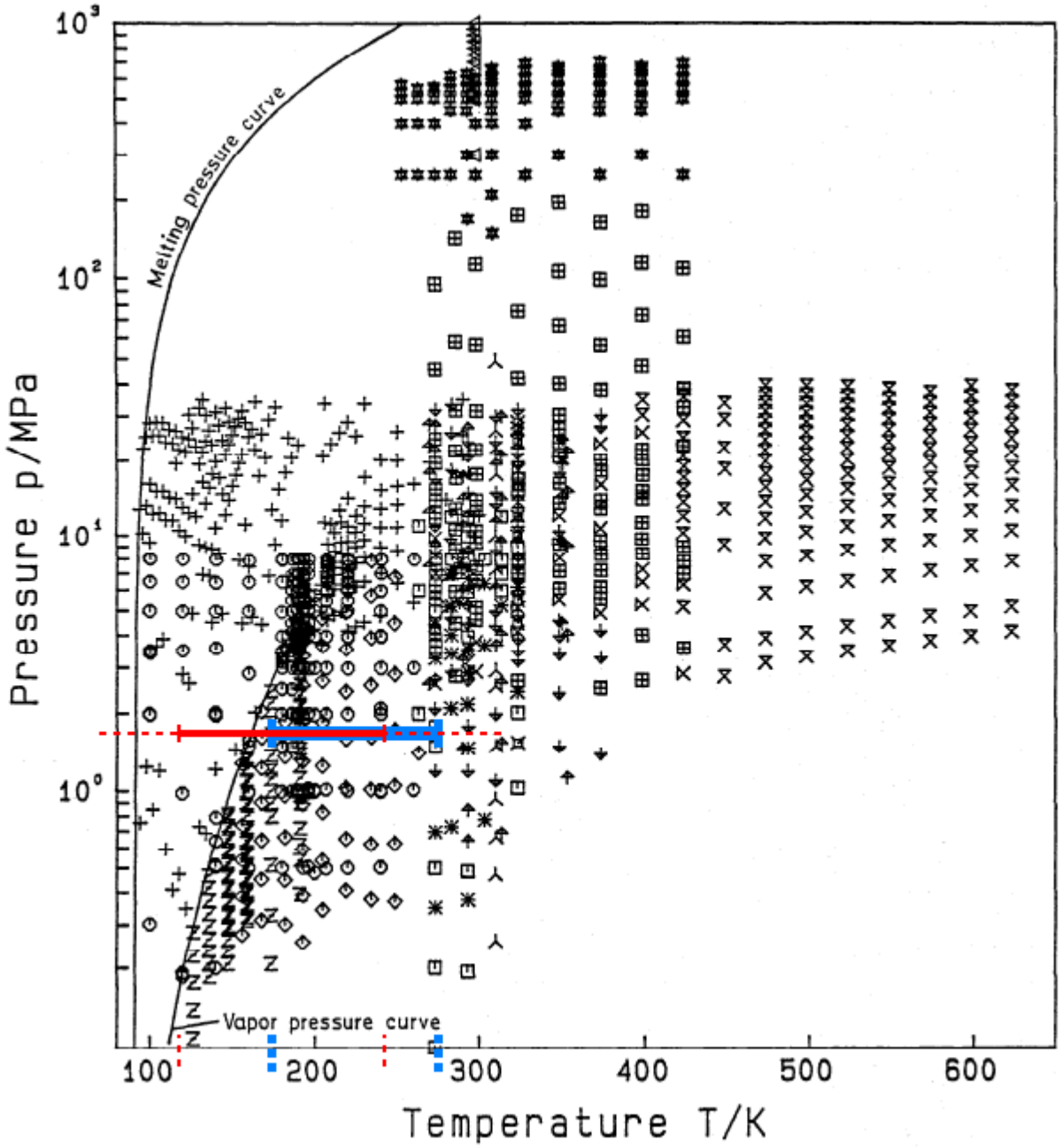

Figure 5-42: Ideal gas (red) and real gas (blue) CFD rake results superimposed upon the real gas methane state diagram considered by [55]. Adapted from [55].

Figure 5-43 shows the data depicted in Figure 5-42 in a way that is easier to see how the ideal and real gas results differ. Values of the ideal gas curve can not be compared to any projection of the real gas curve for temperatures lower than about 170 K due to the sudden change in density expected with real gas behavior at the phase change line, increasing dramatically for lower temperatures at these pressures. For the curve portions above 175 K the difference between the ideal and real gas results are between 7.56% and 19.96%, which is in addition to the 20% error expected by [42] due to using the 1D Nusselt correlations. Figure 5-43 shows the necessity of using a real gas computational model for the entire flow regime, to increase the computational accuracy closer to what may be expected in experimental set-ups.

Table 5-1 compares the ideal and real gas results numerically, and shows higher wall temperatures with the real gas simulations. Although Figure 5-42 shows the ideal gas data range passing through the phase change line, recall that both the ideal gas and real gas numerical models as utilized only solve for a vapor. The phase change line as shown is only useful to realize that an actual cooling channel will experience phase change with the parameters used. The NIST real gas model in FLUENT will solve for a liquid only if the data range stays on the liquid side of the phase change line, but no heat addition can be modeled because the temperature will increase past the line.

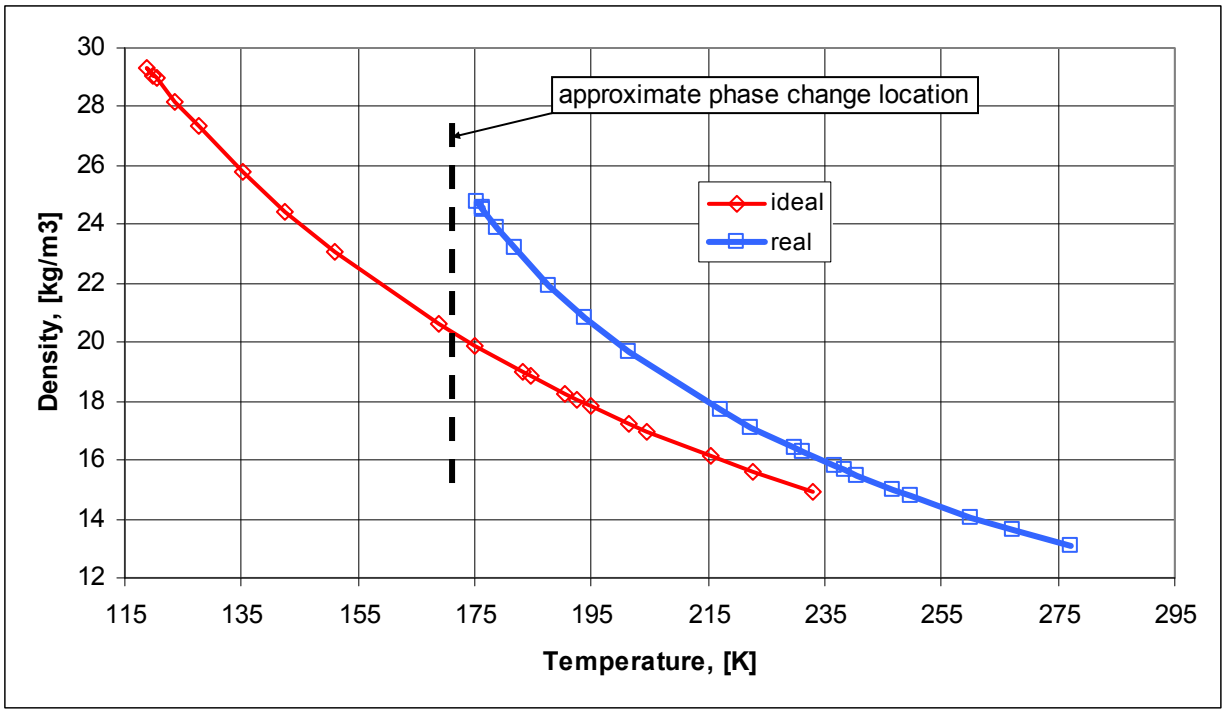

Figure 5-43: Ideal gas (red) and real gas (blue) CFD rake results showing density variation and gas model discrepancies.

Table 5-1: Numerical comparison between $n_c = 29$ results using ideal and real gas.

Parameter	Ideal Gas Result	Real Gas Result
Channel Inlet & Backflow Temperature, [K]	118.055555	175
Max. Hot-wall Wall Temperature, [K]	423.765	465.287
Max. Hot-wall Heat Flux, [W/m^2]	5,705,557.917	5,643,949.78
Max. Channel-bottom Wall Temperature, [K]	408.280	450.036
Max. Channel-left Wall Temperature, [K]	401.935	443.757
Max. Top-wall-top Wall Temperature, [K]	306.907	349.992
Channel Pressure Drop, [N/m^2]	6,076.656	6,895.029
Channel Velocity Increase, [m/s]	7.573	8.367
Channel Coolant Temperature Increase, [K]	96.654	84.919

CHAPTER 6

CONCLUSIONS

Based on the results of the previous chapter, it can be concluded that the circumferential placement of 29 regenerative cooling channels on the cSETR 50lbf engine is the optimal configuration, for the case of running CFD simulations using ideal gas methane, the thermal properties of a NARloy-Z inner shell and an Inconel 718 outer shell, and the other assumptions used. The results of the present research are thus not expected to match exactly a real-world experimental test or actual working engine, but do provide a close estimate from which to build upon. Materials with similar thermal properties may be substituted in an experimental build to maintain similar cooling performance. The parameters for $n_c = 29$ are summarized in Table 6-1.

For comparison purposes, the numerical results of $n_c = 29$ are paired to the results of the same configuration but with a reduced mass flow rate of near nothing in relation. By noting the higher wall temperatures in Table 6-2 for the reduced-flow channel, the benefit of regenerative cooling is discovered overall, and this shows the possible effect of contaminated or blocked channels. Also, using a reduced-flow simulation allows for a control set of data to see that the CFD models are in fact cooling the walls for the required mass flow rate. Recall that a high value for the coolant temperature increase within the channel was expected for the as-designed channel due to the values found in literature. A high value is seen for the reduced-flow channel, however this is deceptive due to the increased heat conduction in the slower moving fluid which can not replenish the channel with the colder inlet flow, as well as due to the higher wall temperatures increasing the average coolant temperature.

Despite the conclusion of using the $n_c = 29$ configuration for the present research, it must be

remembered that a more thorough stress design and analysis should be performed, as well as to use a real-gas model in the CFD simulations to account for the expected phase change with methane, as seen in Figure 5-42. Experimental tests for validation of computational results is always necessary.

Table 6-1: Summary of the parameters for the concluded optimal cooling channel configuration on the cSETR 50lbf engine, using ideal gas methane as the coolant. Values reported are for static ground test conditions (convection outer shell CFD boundary condition).

Group	Parameter	Value
Geometry	Number of Cooling Channels	29
	Channel Width, [mm]	0.645
	Fin Width, [mm]	0.709
	Channel Height, [mm]	7.033
	Channel AR	10.91
	NARloy-Z Chamber Wall Thickness, [mm]	1.098
	INCONEL 718 Outer Shell Thickness, [mm]	1.000
Performance	Maximum Hot-Wall Temperature, [K]	423.765
	Maximum Hot-Wall Heat Flux, [W/m^2]	5,705,557.917
	Maximum Channel-Bottom Temperature, [K]	408.280
	Maximum Top-Wall-Top Temperature, [K]	306.907
	Channel Pressure Drop, [N/m^2]	6,076.656
	Channel Velocity Increase, [m/s]	7.573
	Channel Temperature Increase, [K]	96.654
	Minimum Allowable Cooling Channel Outlet Pressure, [N/m^2]	1.8×10^6

Table 6-2: Numerical comparison between n_c = 29 results and the results of the same configuration with a reduced mass flow rate.

Parameter	As-designed Value	Reduced-flow Value
Channel Mass Flow Rate, [kg/s]	0.00062069	0.0001
FLUENT Courant Parameter	30	20
Max. Hot-wall Wall Temperature, [K]	423.765	782.195
Max. Hot-wall Heat Flux, [W/m^2]	5,705,557.917	5,173,740.572
Max. Channel-bottom Wall Temperature, [K]	408.280	768.359
Max. Channel-left Wall Temperature, [K]	401.935	762.657
Max. Top-wall-top Wall Temperature, [K]	306.907	677.580
Channel Pressure Drop, [N/m^2]	6,076.656	1,154.363
Channel Velocity Increase, [m/s]	7.573	6.001
Channel Coolant Temperature Increase, [K]	96.654	475.789
Channel 2D Net Heat Flux, [W/m^2]	123,021.709	105,838.083

CHAPTER 7

RECOMMENTATIONS FOR FUTURE RESEARCHERS

This chapter lists recommendations for future researchers who choose to continue the work presented herein. Multiple issues arose during the course of this investigation that should be considered by other researchers. Also, the segmented design and analysis of regenerative cooling systems leaves more work to be done for a complete design.

Recommendation 1: model the existing geometry curvature, and optimize the engine contour for the best flow and heat transfer in the channels; refer to [15], [16], [18], [19], and [45].

Recommendation 2: use a user defined real gas model with the existing equations of state found in the other FLUENT real gas model files, study the real gas effect on the heat transfer, and check that the flow resembles the behavior described in literature; refer to [10], [12], [13], and [29].

Recommendation 3: perform a more thorough stress design and analysis for the inner and outer shell before modeling the geometry and running the CFD simulations, and after running the CFD simulations with a separate specialized software tool since only heat conduction is solved in FLUENT for the solid domains; refer to [10], [15], and [22].

Recommendation 4: directly use the solid model geometry files for improved accuracy.

Recommendation 5: model and optimize a channel lengthwise width variation for minimal pressure drop with consideration of thermal effects; refer to [6].

Recommendation 6: use the solid materials that will actually be used for the engine with consideration of both thermal and stress effects, or run multiple simulations with different material properties.

Recommendation 7: include channel surface roughness effects; refer to [10] and [15].

Recommendation 8: use the NASA computer codes for additional validation and design detail; refer to [3], [6], and [23].

Recommendation 9: use a software based method for various thermodynamic properties at elevated temperatures for increased accuracy or validation; refer to [3], [28], and others.

Recommendation 10: investigate the cooling capacity limits; refer to [10].

Recommendation 11: include the combustion heat flux due to radiation; refer to [3].

Recommendation 12: compare the numerical and CFD results to experiment.

Recommendation 13: formulate or use a standardized material property database for variable temperature dependence.

Recommendation 14: iterate for the unknown hot-wall temperature after using the assumed average reference value from literature, as well as for other assumed values.

Recommendation 15: use software programs with the same numerical tolerances when pairing (like MATLAB and HyperMesh and FLUENT) so that the dimensions are exactly as input into one program as are found in the next program, with no "fuzzy zeros" (values of ### x 10^{-19} rather than exactly zero as inputted); recall that HyperMesh has a number insertion problem where it is limited to a certain number of decimal places so the value fits inside the type-in box.

Recommendation 16: use a shorter entrance length so that more cells are available for the solid domains to abide by the FLUENT license cell limit and to allow for better heat transfer within and between all domains.

REFERENCES

[1] NASA University Research Centers website, retrieved 4/15/2011: http://www.nasa.gov/offices/education/programs/descriptions/University_Research_Centers.html

[2] UTEP cSETR website, retrieved 4/15/2011: http://research.utep.edu/Default.aspx?alias=research.utep.edu/csetr

[3] Boysan, M. E., "Analysis of Regenerative Cooling in Liquid Propellant Rocket Engines", M. Sc. thesis, Middle East Technical University, Ankara, Turkey, 2008.

[4] Swiss Propulsion Laboratory website, retrieved 2/10/2011: http://www.spl.ch/products/index.html

[5] Kuhl, D., O. J. Haidn, N. Josien, and D. Coutellier, "Structural Optimization of Rocket Engine Cooling Channels", AIAA-98-3372, 1998.

[6] Wadel, M. F., "Comparison of High Aspect Ratio Cooling Channel Designs for a Rocket Combustion Chamber With Development of an Optimized Design", NASA/TM--1998-206313, National Aeronautics and Space Administration, Lewis Research Center, January, 1998.

[7] Schuff, R., M. Maier, O. Sindiy, C. Ulrich, and S. Fugger, "Integrated Modeling and Analysis for a LOX/Methane Expander Cycle Engine: Focusing on Regenerative Cooling Jacket Design", AIAA Paper 2006-4534, 42nd AIAA/ASME/SAE/ASEE Joint Propulsion Conference & Exhibit, Sacramento, California, July 9 - 12, 2006.

[8] Pizzarelli, M., F. Nasuti, and M. Onofri, "Flow Analysis of Transcritical Methane in Rectangular Cooling Channels", AIAA Paper 2008-4556, 44th AIAA/ASME/SAE/ASEE Joint Propulsion Conference & Exhibit, Hartford, CT, July 21 - 23, 2008.

[9] Internal cSETR communications with Chance P. Garcia and Adrian Trejo, 9/24/2010.

[10] Huzel, D.K., Huang, D.H., “Design of Liquid Propellant Rocket Engines,” NASA SP-125, National Aeronautics and Space Administration, Washington, D. C., 1967.

[11] "Liquid Rocket Engine Nozzles", NASA-SP-8120, National Aeronautics and Space Administration, Glenn Research Center, 1976.

[12] Mitchell, J. P., and W. R. Kaminski, "Space Storable Regenerative Cooling Investigation", AIAA Paper 68-616, AIAA 4th Propulsion Joint Specialist Conference, Cleveland, Ohio, June 10-14, 1968.

[13] Baehr, H. D., and K. Stephan, "Heat and Mass Transfer", 2nd ed., Springer, New York,

2006.

[14] Wennerberg, J. C., W. E. Anderson, P. A. Haberlen, H. Jung, and C. L. Merkle, "Supercritical Flows in High Aspect Ratio Cooling Channels", AIAA Paper 2005-4302, 41st AIAA/ASME/SAE/ASEE Joint Propulsion Conference & Exhibit, Tucson, AZ, July 10-13, 2005.

[15] Cook, R.T., Coffey, G.A., "Space Shuttle Orbiter Engine Main Combustion Chamber Cooling and Life," AIAA Paper 73-1310, AIAA/SAE 9th Propulsion Conference, Las Vegas, NV, November 5-7, 1973.

[16] Schoenman, L., "Low-Thrust Isp Sensitivity Study, Final Report", NASA-CR-165621, National Aeronautics and Space Administration, Lewis Research Center, April, 1982.

[17] Gere, J. M., "Mechanics of Materials", 5th ed., Brooks/Cole Thomson Learning, Pacific Grove, CA, 2001.

[18] Carlile, J., and R. Quentmeyer, "An Experimental Investigation of High-Aspect-Ratio Cooling Passages", NASA-TM-105679 also as AIAA Paper 92-3154, 28th AIAA/SAE/ASME/ASEE Joint Propulsion Conference, Nashville, TN, July 6-8, 1992; page 1 missing from NASA Technical Reports Server (http://ntrs.nasa.gov/) electronic download when retrieved.

[19] Meyer, M. L., and J. E. Giuliani, "Flow visualization study in high aspect ratio cooling channels for rocket engines", Pennsylvania State Univ., NASA Propulsion Engineering Research Center, Volume 2, p 101-105, November 1, 1993.

[20] Mitsubishi Materials Online Catalog website, retrieved 2/10/2011: http://www.mitsubishicarbide.net/mmus/en/catalogue/index.html

[21] MSC Industrial Supply Company, Melville, NY, website, retrieved 2/9/2011: www.mscdirect.com

[22] Kuhl, D., "Thermomechanical Analysis Using Finite Element Methods with Particular Emphasis on Rocket Combustion Chambers", European Congress on Computational Methods in Applied Sciences and Engineering, ECCOMAS 2004, July 24-28, 2004.

[23] Naraghi, M. H., S. Dunn, and D. Coats, "Dual Regenerative Cooling Circuits for Liquid Rocket Engines (Preprint)", AIAA Paper 2006-4367, 42nd AIAA/ASME/SAE/ASEE Joint Propulsion Conference & Exhibit, Sacramento, California, July 9 - 12, 2006.

[24] MatWeb Material Property Data, MatWeb, LLC, website, retrieved 2/10/2011: www.matweb.com

[25] Esposito, J. J., and R. F. Zabora, "Thrust Chamber Life Prediction; Volume I - Mechanical and Physical Properties of High Performance Rocket Nozzle Materials,"

NASA CR-134806, National Aeronautics and Space Administration, Lewis Research Center, 1975.

[26] Conway, J.B., R. H. Stentz, and J. T. Berling, "High-Temperature, Low-Cycle Fatigue of Copper-Base Alloys for Rocket Nozzles; Part I - Data Summary for Materials Tested in Prior Programs", NASA-CR-134908, National Aeronautics and Space Administration, Lewis Research Center, 1975.

[27] Ellis, D. L., and G. M. Michal, "Mechanical and Thermal Properties of Two Cu-Cr-Nb Alloys and NARloy-Z", NASA-CR-198529, National Aeronautics and Space Administration, Lewis Research Center, 1996.

[28] Hill, P. G., and C. R. Peterson, "Mechanics and Thermodynamics of Propulsion", 2nd ed., Addison-Wesley Publishing Company, Inc., Massachusetts, 1992.

[29] Janna, W. S., "Engineering Heat Transfer", 2nd ed., CRC Press LLC, Boca Raton, Florida, 2000.

[30] Bucchi, A., A. Congiunti, and C. Bruno, "Investigation of Transpiration Cooling Performance in LOX/Methane Liquid Rocket Engines", IAC Paper IAC-03-S.3.08, 54th International Astronautical Congress of the International Astronautical Federation, the International Academy of Astronautics, and the International Institute of Space Law, Bremen, Germany, September 29 - October 3, 2003.

[31] Cengel, Y. A., and R. H. Turner, "Selected Material from Fundamentals of Thermal-Fluid Sciences", McGraw-Hill, New York, 2001.

[32] Moran, M. J., and H. N. Shapiro, "Fundamentals of Engineering Thermodynamics", 6th ed., John Wiley & Sons, Inc., Hoboken, NJ, 2008.

[33] Wang, Q., F. Wu, M. Zeng, L. Luo, and J. Sun, "Numerical simulation and optimization on heat transfer and fluid flow in cooling channel of liquid rocket engine thrust chamber", Engineering Computations: International Journal for Computer-Aided Engineering and Software, Vol. 23, No. 8, pp. 907-921, Emerald Group Publishing Limited 0264-4401, 2006.

[34] Kim, K., and D. Ju, "Development of 'Chase-10' Liquid Rocket Engine Having 10tf Thrust Using LOX & LNG (Methane)", AIAA Paper 2006-4907, 42nd AIAA/ASME/SAE/ASEE Joint Propulsion Conference & Exhibit, Sacramento, California, July 9 - 12, 2006.

[35] Brown, C. D., "Spacecraft Propulsion", AIAA Educational Series, American Institute of Aeronautics and Astronautics, Inc., Washington, D. C., 1996.

[36] Shames, I. H., and F. A. Cozzarelli, "Elastic and Inelastic Stress Analysis", Revised Printing, Taylor & Francis Ltd., Philadelphia, PA, 1997.

[37] Minato, R., K. Higashino, M. Sugioka, T. Kobayashi, S. Ooya, Y. Sasayama, "LNG Rocket Engine with Coking Inhibited Regenerative Cooling System", AIAA Paper 2009-7392, 16th AIAA/DLR/DGLR International Space Planes and Hypersonic Systems and Technologies Conference, 2009.

[38] Reid, R. C., J. M. Prausnitz, and T. K. Sherwood, "The Properties of Gases and Liquids", 3rd ed., McGraw-Hill, 1977.

[39] Bradford, C., "Class Notes for MECH 5310, Advanced Thermodynamics with Dr. Bronson at The University of Texas at El Paso", unpublished, Fall 2010.

[40] Oxtoby, D. W., H. P. Gillis, and N. H. Nachtrieb, "Principles of Modern Chemistry", 4th ed., Saunders College Publishing, Harcourt Brace & Company, Orlando, FL, 1999.

[41] Versteeg, H. K., and W. Malalasekera, "An introduction to computational fluid dynamics. The finite volume method." Longman Scientific & Technical, Essex, England, 1995.

[42] Daimon, Y., Y. Ohnishi, H. Negishi, and N. Yamanishi, "Combustion and Heat Transfer Modeling in Regeneratively Cooled Thrust Chambers (Co-axial Injector Flow Analysis)", AIAA Paper 2009-5492, 45th AIAA/ASME/SAE/ASEE Joint Propulsion Conference & Exhibit, Denver, Colorado, August 2 - 5, 2009.

[43] Bertin, J. J., "Aerodynamics for Engineers", 4th ed., Prentice Hall, Inc., Upper Saddle River, NJ, 2002.

[44] Ahmad, R. A., "Internal Flow Simulation of Enhanced Performance Solid Rocket Booster for the Space Transportation System", AIAA Paper 2001-5236, 37th AIAA/ASME/SAE/ASEE Joint Propulsion Conference and Exhibit, Salt Lake City, UT, July 8-11, 2001.

[45] Lomax, H., T. H. Pulliam, and D. W. Zingg, "Fundamentals of Computational Fluid Dynamics", Springer, New York, 2003.

[46] Bhaskaran, R., and Y. S. Khoo, "FLUENT Learning Modules - Forced Convection", Swanson Engineering Simulation Program, Sibley School of Mechanical and Aerospace Engineering, Cornell University, website, retrieved 1/17/2011: https://confluence.cornell.edu/display/SIMULATION/FLUENT+-+Forced+Convection

[47] "FLUENT 6.3 User's Guide", Fluent Inc., Lebanon, New Hampshire, 2006.

[48] "ANSYS FLUENT 12.0 User's Guide", ANSYS, Inc., 2009.

[49] Woschnak, A., and M. Oschwald, "Thermo- and Fluidmechanical Analysis of High Aspect Ratio Cooling Channels", AIAA Paper 2001-3404, 37th AIAA/ASME/SAE/ASEE Joint Propulsion Conference and Exhibit, Salt Lake City, UT,

July 8-11, 2001.

[50] Pizzarelli, M., F. Nasuti, R. Paciorri, and M. Onofri, "A Numerical Model for Supercritical Flow in Rocket Engines Applications", AIAA Paper 2007-5501, 43rd AIAA/ASME/ASE/ASEE Joint Propulsion Conference & Exhibit, Cincinnati, OH, July 8-11, 2007.

[51] "ANSYS FLUENT 12.0 Theory Guide", ANSYS, Inc., 2009.

[52] website with information copyright Fluent, Inc., 2007, retrieved 3/30/11: http://progdata.umflint.edu/MAZUMDER/Fluent/Fluent%20Tutorial/Multiphase%20flow%20tutorial/fuel%20cell/pemfc.pdf

[53] Gerald, C. F., and Wheatley, P. O., "Applied Numerical Analysis", 6th ed., Addison Wesley Longman, Inc., 1999.

[54] Bradford, C., "Class Notes for AERO 320, Numerical Methods with Dr. Haisler at Texas A&M University", unpublished, Spring 2002.

[55] Setzmann, U., and W. Wagner, "A New Equation of State and Tables of Thermodynamic Properties for Methane Covering the Range from the Melting Line to 625 K at Pressures up to 1000 MPa", J. Phys. Chem. Ref. Data, Vol. 20, No. 6, 1991, pgs 1061 to 1155.

APPENDIX I: MAPLE Code to Calculate Adiabatic Flame Temperature

CH4O2 flame temperature.mws; adiabatic flame temperature for the methane oxygen combustion

```
> restart:
```

```
> hf_ch4 := -74873;
```

$$hf\_ch4 := -74873$$

```
> hf_co2 := -393522;
```

$$hf\_co2 := -393522$$

```
> hf_h2o := -241827;
```

$$hf\_h2o := -241827$$

```
> hf_co := -110530;
```

$$hf\_co := -110530$$

```
> cp_ch4 := -672.87 + 439.74*(T/100)^(0.25) -
24.875*(T/100)^(0.75) + 323.88*(T/100)^(-0.5);
```

$$cp\_ch4 := -672.87 + 139.0579978\ T^{.25} - .7866165679\ T^{.75} + \frac{3238.800000}{T^{.5}}$$

```
> cp_o2 := 37.432 + 0.020102*(T/100)^(1.5) - 178.57*(T/100)^(-
1.5) + 236.88*(T/100)^(-2);
```

$$cp\_o2 := 37.432 + .00002010200000\ T^{1.5} - \frac{178570.0000}{T^{1.5}} + \frac{.236880000\ 10^{7}}{T^{2}}$$

```
> cp_co2 := -3.7357 + 30.529*(T/100)^(0.5) - 4.1034*(T/100) +
0.024198*(T/100)^(2);
```

$$cp\_co2 := -3.7357 + 3.052900000\ T^{.5} - .04103400000\ T + .2419800000\ 10^{-5}\ T^{2}$$

```
> cp_h2o := 143.05 - 183.54*(T/100)^(0.25) + 82.751*(T/100)^(0.5)
- 3.6989*(T/100);
```

$$cp\_h2o := 143.05 - 58.04044417\ T^{.25} + 8.275100000\ T^{.5} - .03698900000\ T$$

```
> cp_co := 69.145 - 0.70463*(T/100)^(0.75) - 200.77*(T/100)^(-
0.5) + 176.76*(T/100)^(-0.75);
```

$$cp\_co := 69.145 - .02228235708\ T^{.75} - \frac{2007.700000}{T^{.5}} + \frac{5589.641992}{T^{.75}}$$

```
> n_ch4 := 1;
```

$$n\_ch4 := 1$$

```
> n_o2 := 1.60135209701;
```

$$n\_o2 := 1.60135209701$$

```
> n_co2 := 0.20270419402;
```

$$n\_co2 := .20270419402$$

```
> n_h2o := 2;
```

$$n\_h2o := 2$$

```
> n_co := 0.79729580598;
```

$$n\_co := .79729580598$$

```
> zero := -1*n_ch4*hf_ch4 - int(n_ch4*cp_ch4 + n_o2*cp_o2,
T=526.222222..298.15) + n_co2*hf_co2 + n_h2o*hf_h2o + n_co*hf_co
+ int(n_co2*cp_co2 + n_h2o*cp_h2o + n_co*cp_co, T=298.15..Tad);
```

$$zero := -616464.0160 + 340.4717764\ Tad + 11.44602375\ Tad^{(3/2)} - .04114788195\ Tad^{2} + .1635012029\ 10^{-6}\ Tad^{3} - 92.86471064\ Tad^{(5/4)} - .01015178849\ Tad^{(7/4)} - 3201.461580\ \sqrt{Tad} + 17826.39247\ Tad^{(1/4)}$$

```
> plot(zero, Tad=0..5000);
```

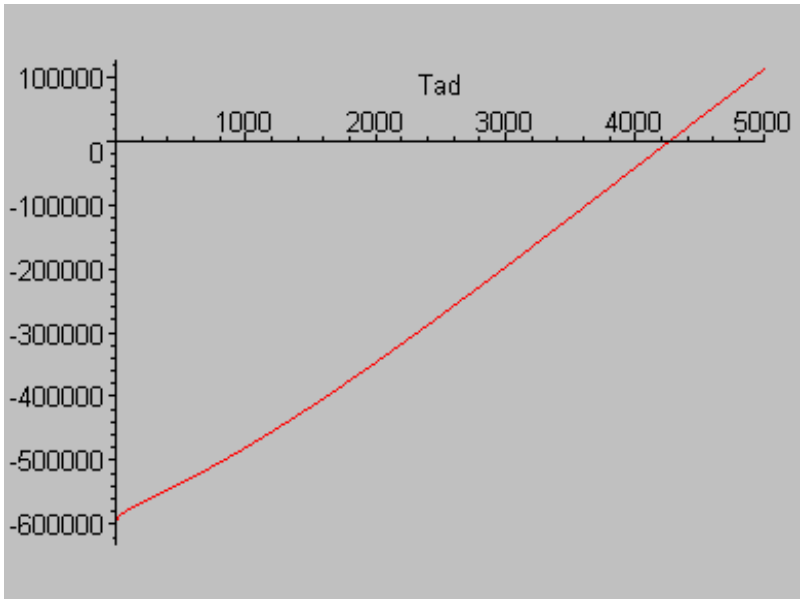

the "fsolve" function computes zeros of functions within a specified range

```
> fsolve(zero, Tad, 4000..5000);
```

4269.158187

>

APPENDIX II: Bartz Heat Transfer Coefficient Values Along True Length

true length, [mm]	h_g, [W/m2-K]	true length, [mm]	h_g, [W/m2-K]	true length, [mm]	h_g, [W/m2-K]	true length, [mm]	h_g, [W/m2-K]
0.000	120.023	4.137	134.908	8.275	152.751	12.412	174.580
0.103	120.364	4.241	135.315	8.378	153.241	12.516	175.188
0.207	120.708	4.344	135.724	8.482	153.731	12.619	175.798
0.310	121.052	4.448	136.133	8.585	154.226	12.723	176.414
0.414	121.398	4.551	136.545	8.689	154.727	12.826	177.031
0.517	121.745	4.655	136.959	8.792	155.229	12.930	177.651
0.621	122.093	4.758	137.375	8.896	155.728	13.033	178.273
0.724	122.445	4.862	137.792	8.999	156.232	13.136	178.898
0.827	122.797	4.965	138.212	9.102	156.741	13.240	179.526
0.931	123.152	5.068	138.634	9.206	157.251	13.343	180.159
1.034	123.506	5.172	139.058	9.309	157.763	13.447	180.794
1.138	123.863	5.275	139.486	9.413	158.278	13.550	181.430
1.241	124.223	5.379	139.915	9.516	158.797	13.654	182.073
1.345	124.582	5.482	140.345	9.620	159.318	13.757	182.721
1.448	124.943	5.586	140.777	9.723	159.842	13.860	183.369
1.552	125.306	5.689	141.210	9.826	160.366	13.964	184.019
1.655	125.671	5.792	141.645	9.930	160.890	14.067	184.671
1.758	126.038	5.896	142.081	10.033	161.421	14.171	185.327
1.862	126.405	5.999	142.522	10.137	161.958	14.274	185.989
1.965	126.774	6.103	142.967	10.240	162.492	14.378	186.655
2.069	127.146	6.206	143.412	10.344	163.026	14.481	187.321
2.172	127.517	6.310	143.858	10.447	163.576	14.585	187.989
2.276	127.889	6.413	144.306	10.550	164.132	14.688	188.665
2.379	128.265	6.516	144.756	10.654	164.688	14.791	189.349
2.482	128.643	6.620	145.206	10.757	165.246	14.895	190.027
2.586	129.021	6.723	145.659	10.861	165.808	14.998	190.713
2.689	129.401	6.827	146.119	10.964	166.378	15.102	191.401
2.793	129.784	6.930	146.582	11.068	166.940	15.205	192.092
2.896	130.169	7.034	147.042	11.171	167.510	15.309	192.787
3.000	130.553	7.137	147.505	11.275	168.085	15.412	193.481
3.103	130.938	7.241	147.967	11.378	168.661	15.515	194.189
3.207	131.328	7.344	148.434	11.481	169.241	15.619	194.896
3.310	131.721	7.447	148.905	11.585	169.818	15.722	195.603
3.413	132.111	7.551	149.377	11.688	170.407	15.826	196.315
3.517	132.505	7.654	149.853	11.792	170.995	15.929	197.035
3.620	132.902	7.758	150.327	11.895	171.584	16.033	197.759
3.724	133.300	7.861	150.808	11.999	172.177	16.136	198.483
3.827	133.701	7.965	151.289	12.102	172.774	16.239	199.211
3.931	134.101	8.068	151.775	12.205	173.374	16.343	199.944
4.034	134.504	8.171	152.262	12.309	173.976	16.446	200.680

true length, [mm]	h_g, [W/m2-K]	true length, [mm]	h_g, [W/m2-K]	true length, [mm]	h_g, [W/m2-K]	true length, [mm]	h_g, [W/m2-K]
16.550	201.420	20.687	234.747	24.825	277.079	28.962	331.884
16.653	202.165	20.791	235.682	24.928	278.281	29.066	333.457
16.757	202.916	20.894	236.625	25.032	279.495	29.169	335.039
16.860	203.669	20.998	237.575	25.135	280.712	29.272	336.631
16.964	204.426	21.101	238.531	25.238	281.934	29.376	338.235
17.067	205.188	21.204	239.493	25.342	283.165	29.479	339.850
17.170	205.955	21.308	240.458	25.445	284.404	29.583	341.476
17.274	206.727	21.411	241.427	25.549	285.652	29.686	343.114
17.377	207.503	21.515	242.405	25.652	286.910	29.790	344.768
17.481	208.281	21.618	243.390	25.756	288.176	29.893	346.434
17.584	209.063	21.722	244.379	25.859	289.451	29.996	348.111
17.688	209.849	21.825	245.374	25.962	290.729	30.100	349.800
17.791	210.640	21.928	246.375	26.066	292.014	30.203	351.499
17.894	211.435	22.032	247.382	26.169	293.312	30.307	353.215
17.998	212.235	22.135	248.392	26.273	294.621	30.410	354.932
18.101	213.041	22.239	249.408	26.376	295.935	30.514	356.669
18.205	213.852	22.342	250.436	26.480	297.261	30.617	358.497
18.308	214.666	22.446	251.470	26.583	298.591	30.721	360.335
18.412	215.484	22.549	252.509	26.687	299.935	30.824	362.192
18.515	216.307	22.653	253.556	26.790	301.286	30.927	364.041
18.619	217.139	22.756	254.603	26.893	302.642	31.031	365.943
18.722	217.966	22.859	255.660	26.997	304.017	31.134	367.842
18.825	218.805	22.963	256.730	27.100	305.396	31.238	369.749
18.929	219.647	23.066	257.801	27.204	306.782	31.341	371.670
19.032	220.494	23.170	258.880	27.307	308.177	31.445	373.609
19.136	221.346	23.273	259.962	27.411	309.582	31.548	375.565
19.239	222.198	23.377	261.058	27.514	310.998	31.651	377.541
19.343	223.068	23.480	262.160	27.617	312.422	31.755	379.530
19.446	223.938	23.583	263.265	27.721	313.858	31.858	381.530
19.549	224.807	23.687	264.376	27.824	315.305	31.962	383.548
19.653	225.681	23.790	265.494	27.928	316.762	32.065	385.585
19.756	226.564	23.894	266.619	28.031	318.229	32.169	387.638
19.860	227.453	23.997	267.751	28.135	319.705	32.272	389.707
19.963	228.347	24.101	268.891	28.238	321.190	32.376	391.790
20.067	229.246	24.204	270.041	28.342	322.685	32.479	393.888
20.170	230.148	24.308	271.197	28.445	324.190	32.582	396.004
20.273	231.057	24.411	272.359	28.548	325.708	32.686	398.138
20.377	231.975	24.514	273.528	28.652	327.237	32.789	400.293
20.480	232.895	24.618	274.704	28.755	328.775	32.893	402.469
20.584	233.818	24.721	275.888	28.859	330.324	32.996	404.656

true length, [mm]	h_g, [W/m2-K]	true length, [mm]	h_g, [W/m2-K]	true length, [mm]	h_g, [W/m2-K]	true length, [mm]	h_g, [W/m2-K]
33.100	406.856	37.237	512.212	41.374	663.719	45.512	894.189
33.203	409.081	37.340	515.344	41.478	668.337	45.615	901.404
33.306	411.326	37.444	518.504	41.581	673.003	45.719	908.730
33.410	413.589	37.547	521.693	41.685	677.712	45.822	916.178
33.513	415.869	37.651	524.910	41.788	682.505	45.926	923.647
33.617	418.167	37.754	528.156	41.892	687.285	46.029	931.237
33.720	420.483	37.858	531.431	41.995	692.171	46.133	938.912
33.824	422.819	37.961	534.761	42.099	697.072	46.236	946.645
33.927	425.175	38.065	538.075	42.202	702.037	46.339	954.549
34.031	427.551	38.168	541.455	42.305	707.063	46.443	962.515
34.134	429.964	38.271	544.846	42.409	712.110	46.546	970.581
34.237	432.364	38.375	548.272	42.512	717.264	46.650	978.750
34.341	434.806	38.478	551.737	42.616	722.447	46.753	987.042
34.444	437.256	38.582	555.206	42.719	727.698	46.857	995.436
34.548	439.725	38.685	558.755	42.823	733.004	46.960	1003.925
34.651	442.238	38.789	562.316	42.926	738.367	47.063	1012.518
34.755	444.745	38.892	565.915	43.029	743.788	47.167	1021.213
34.858	447.301	38.995	569.546	43.133	749.273	47.270	1030.030
34.961	449.861	39.099	573.207	43.236	754.817	47.374	1038.986
35.065	452.451	39.202	576.906	43.340	760.423	47.477	1048.060
35.168	455.061	39.306	580.648	43.443	766.092	47.581	1057.256
35.272	457.684	39.409	584.426	43.547	771.826	47.684	1066.577
35.375	460.331	39.513	588.239	43.650	777.624	47.788	1076.030
35.479	463.008	39.616	592.089	43.754	783.485	47.891	1085.613
35.582	465.707	39.719	595.976	43.857	789.411	47.994	1095.331
35.685	468.431	39.823	599.898	43.960	795.402	48.098	1105.166
35.789	471.176	39.926	603.855	44.064	801.465	48.201	1115.119
35.892	473.940	40.030	607.854	44.167	807.599	48.305	1125.231
35.996	476.732	40.133	611.898	44.271	813.807	48.408	1135.496
36.099	479.554	40.237	615.978	44.374	820.089	48.512	1145.877
36.203	482.396	40.340	620.096	44.478	826.441	48.615	1156.384
36.306	485.257	40.444	624.261	44.581	832.863	48.718	1167.033
36.410	488.147	40.547	628.472	44.684	839.360	48.822	1177.825
36.513	491.068	40.650	632.721	44.788	845.932	48.925	1188.764
36.616	494.014	40.754	637.009	44.891	852.588	49.029	1199.852
36.720	496.986	40.857	641.344	44.995	859.325	49.132	1211.070
36.823	499.975	40.961	645.724	45.098	866.135	49.236	1222.437
36.927	502.984	41.064	650.154	45.202	873.023	49.339	1233.931
37.030	506.030	41.168	654.631	45.305	879.998	49.442	1245.578
37.134	509.107	41.271	659.152	45.408	887.057	49.546	1257.362

true length, [mm]	h_g, [W/m2-K]	true length, [mm]	h_g, [W/m2-K]	true length, [mm]	h_g, [W/m2-K]	true length, [mm]	h_g, [W/m2-K]
49.649	1269.359	53.731	1345.534	60.042	445.909	110.000	183.147
49.753	1281.389	53.837	1329.978	60.254	431.208	120.000	183.147
49.856	1293.646	53.945	1313.705	60.466	417.239	130.000	183.147
49.960	1306.049	54.053	1296.777	60.678	403.950	140.000	183.147
50.063	1318.598	54.162	1279.204	60.890	391.318	140.100	183.147
50.167	1331.372	54.272	1260.977	61.102	379.305	156.249	183.147
50.270	1344.213	54.383	1242.101	61.314	367.846		
50.373	1357.361	54.496	1222.688	61.526	356.932		
50.477	1370.524	54.610	1202.701	61.738	346.514		
50.580	1383.313	54.725	1182.170	61.950	336.568		
50.684	1396.257	54.842	1161.113	62.162	327.055		
50.787	1408.901	54.960	1139.614	62.374	317.955		
50.890	1420.668	55.081	1117.579	62.586	309.247		
50.992	1431.521	55.203	1095.113	62.798	300.896		
51.094	1441.373	55.328	1072.217	63.010	292.906		
51.195	1450.344	55.455	1048.886	63.222	285.223		
51.296	1458.304	55.584	1025.091	63.434	277.852		
51.397	1465.226	55.716	1000.890	63.645	270.781		
51.498	1471.191	55.852	976.286	63.857	263.972		
51.598	1476.128	55.991	951.209	64.069	257.439		
51.698	1480.021	56.134	925.717	64.281	251.137		
51.799	1482.856	56.281	899.800	64.493	245.077		
51.899	1484.624	56.433	873.452	64.705	239.245		
51.999	1485.374	56.590	846.637	64.917	233.622		
52.099	1485.102	56.754	819.413	65.129	228.195		
52.199	1483.703	56.925	791.687	65.341	222.966		
52.299	1481.289	57.105	763.433	65.553	217.917		
52.399	1477.867	57.295	734.586	65.765	213.044		
52.499	1473.343	57.499	704.904	65.977	208.332		
52.600	1467.837	57.711	675.498	66.189	203.777		
52.701	1461.315	57.923	647.899	66.401	199.376		
52.802	1453.747	58.135	621.928	66.613	195.116		
52.903	1445.210	58.347	597.507	66.825	190.996		
53.005	1435.730	58.558	574.528	67.037	187.007		
53.107	1425.290	58.770	552.877	67.249	183.147		
53.210	1413.921	58.982	532.472	67.349	183.147		
53.313	1401.614	59.194	513.196	70.000	183.147		
53.416	1388.451	59.406	494.988	80.000	183.147		
53.521	1374.507	59.618	477.750	90.000	183.147		
53.625	1360.313	59.830	461.408	100.000	183.147		

APPENDIX III: MATLAB Code to Iterate the Fin Height Equation

```
% 1/25/11 to 3/15/11
%
%%%%%%%%%%%%%%%%%%%%%%%%%%
%
% this code iterates the heat transfer theory equation for the height of a
% cooling channel with the various equations for the heat
% transfer coefficient of convection inside a cooling channel; see other
% notes for details
%
%%%%%%%%%%%%%%%%%%%%%%%%%%
clc
clear
% constants and knowns:
hmax = 0.008; % max channel height by fabrication constraint, [m]
% minimum and maximum number of cooling channels to iterate for, calculated
% such that the channel widths are guaranteed to fall within the machining
% and stress limits because these two numbers are calculated based on
% those limits, by hand:
ncmin = 19; % minimum number of cooling channels to iterate for, calculated
ncmax = 37; % maximum number of cooling channels to iterate for, calculated
nciter = ncmax-ncmin+1; %%%debug%%% 2; % total number of iterations for n_c
cp_bm = 2222; % specific heat of methane, standard reference temperature
              % FLUENT Material Database constant, [J/kg-K]

lambda_bm = 0.0332; % thermal conductivity of methane, s.r.t.F.M.D.c., [W/m-
K]

mu_bm = 1.087e-5; % viscosity of methane, s.r.t.F.M.D.c., [kg/m-s]
mdot_t = 0.018; % total mass flow rate of methane, ref. [9], [kg/s]
r_o = 0.006248; % outer radius of nozzle at throat, calculated, [m]
hinitial = 0.001; %%%debug%%% 0.00001 % initial guess for the fin height [m]

deltah = 0.0001; % delta h for adding incremental height at each iteration
[m]

lambda_f = 295; % thermal conductivity of NARloy-Z, ref. [25], [W/m-K]
T_co = 298.15; % standard reference temperature for "coolant bulk
               % temperature", [K]
T_wc = 533; % coolant side wall temperature, ref. [16], [K]
mu_w = 1.7525e-5; % coolant (methane) viscosity at coolant-side wall
                  % temperature T_wc, calculated, [kg/m-s]
diff = zeros(1,2); % initiate dummy difference variable
converge = 1.0e-6; % convergence criteria
hi = zeros(1,2); % iteration values holder for h
% matrix of solutions:
% rows = range of n_c values
% column 1 = n_c value
% column 2 = w value for n_c [m]
% column 3 = delta_f value for n_c [m]
% column 4 = mdot_c for n_c [kg/s]
% column 5 = alpha_g_1 value [W/m2-K]
```

```
% column 6 = h_1 value for alpha_g_1 [m]
% column 7 = channel AR_1 value for alpha_g_1
% column 8 = alpha_g_2 value [W/m2-K]
% column 9 = h_2 value for alpha_g_2 [m]
% column 10 = channel AR_2 value for alpha_g_2
% column 11 = alpha_g_3 value [W/m2-K]
% column 12 = h_3 value for alpha_g_3 [m]
% column 13 = channel AR_3 value for alpha_g_3
% column 14 = alpha_g_4 value [W/m2-K]
% column 15 = h_4 value for alpha_g_4 [m]
% column 16 = channel AR_4 value for alpha_g_4
solutions = zeros(nciter,16);

% alpha_g equation constant coefficients:
% A for alpha_g_1
A = 0.023*((4/pi)^0.8)*(cp_bm^0.33)*(mu_bm^(-0.47))*(lambda_bm^0.67);
% B for alpha_g_2

B = 0.023*((4/pi)^0.8)*(lambda_bm^0.6)*(mu_bm^(-0.26))*(cp_bm^0.4)*(mu_w^(-
0.14))*(mdot_t^0.8);

% D for alpha_g_3

D = 0.027*((4/pi)^0.8)*(lambda_bm^(2/3))*(mu_bm^(-49/150))*(cp_bm^(1/3))*
(mu_w^(-0.14))*(mdot_t^0.8);

% E for alpha_g_4

E = 0.029*((4/pi)^0.8)*(lambda_bm^(2/3))*(mu_bm^(-7/15))*(cp_bm^(1/3))*
((T_co/T_wc)^(0.55))*(mdot_t^0.8);

% loops
for n_c_e=1:nciter % loop for each n_c

    n_c = ncmin + n_c_e - 1; %%%debug%%% ; % figure out which n_c to use for
this loop

    % record and report values for this n_c:
    solutions(n_c_e,1) = n_c; % number of channels
    n_c = n_c % display which n_c the current iteration is for
    %pause(2.0) %%%debug%%% %
    solutions(n_c_e,2) = 2*pi*r_o/(2.1*n_c); % w value
    solutions(n_c_e,3) = 1.1*solutions(n_c_e,2); % delta_f value
    solutions(n_c_e,4) = mdot_t/n_c; % mdot_c value
    % initial value for h, re-initialize for each n_c:
    hi(:) = hinitial;
    % re-calculate initial alpha values for each n_c:

    alpha_g_1 = A*((mdot_t/n_c)^0.8)*((2*pi*r_o*hinitial/(pi*r_o+
1.05*n_c*hinitial))^(-1.8));

    alpha_g_2 = B*(n_c^(-0.8))*((2*pi*r_o*hinitial/(pi*r_o+
1.05*n_c*hinitial))^(-1.8));

    alpha_g_3 = D*(n_c^(-0.8))*((2*pi*r_o*hinitial/(pi*r_o+
1.05*n_c*hinitial))^(-1.8));
```

```
    alpha_g_4 = E*(n_c^(-0.8))*((2*pi*r_o*hinitial/(pi*r_o+
1.05*n_c*hinitial))^(-1.8));

    diff(:) = 1000; % re-initialize for each n_c
    for n_alpha=1:4 %loop for each alpha_g
        %n_alpha = n_alpha %%%debug%%% %

        % choose which initial alpha_g value to use and set index to store
solution

        if (n_alpha == 1)
            alpha_g = alpha_g_1;
            index = 5;
        elseif (n_alpha == 2)
            alpha_g = alpha_g_2;
            index = 8;
        elseif (n_alpha == 3)
            alpha_g = alpha_g_3;
            index = 11;
        else
            alpha_g = alpha_g_4;
            index = 14;
        end

        hi(:) = hinitial; % re-initialize for each alpha_g (which use
hinitial)

        diff(:) = 1000; % re-initialize for each alpha_g
        ee = 0; % WHILE loop counter, re-initialize for each alpha_g
        % loop to iterate h
        while (diff(1,1) > converge)
            ee = ee + 1;

            hi(1,2) = 1.4192*((11*pi*r_o*lambda_f/(21*n_c))^0.5)*
(alpha_g^(-0.5))-(11*pi*r_o/(21*n_c)); %%%debug%%% ;

            diff(1,2) = abs(hi(1,2)-hi(1,1)); %%%debug%%% ;
            %pause(2.0) %%%debug%%% %
            % multiplier to handle divergence
            if (diff(1,2) >= diff(1,1))

                diff(:) = 1000; % reset value to initial if diverging to
start over

                deltahmult = -1; % make hinitial smaller
            else
                deltahmult = 0;
            end
            % multiplier to handle negative values of h
            if (hi(1,2) <= 0.0)

                hi(1,2) = hinitial + deltah*ee; % reset value to initial plus
more each time

                deltahmult = 5; % add a lot more of deltah
```

```
                diff(:) = 1000; % reset since reseting hi
            else
                deltahmult = 0;
            end
            % store the alpha_g value before calculating a new one for the
            % next loop since the current value will correspond to the
            % converged h:
            solutions(n_c_e,index) = alpha_g;
            % prepare for next loop:
            % set current/new hi(1,2) to previous hi(1,1):
            hi(1,1) = hi(1,2) + deltahmult*deltah;
            %hi(1,1) = hi(1,1) %%%debug%%% %
            %pause(2.0) %%%debug%%% %
            % set current diff to previous diff to loop:
            diff(1,1) = diff(1,2);
            % calculate a new alpha_g for the next WHILE loop, depending
            % on which alpha_g is being used for the current WHILE loop:
            if (n_alpha == 1)

                alpha_g_1 = A*((mdot_t/n_c)^0.8)*((2*pi*r_o*hi(1,1)/(pi*r_o+
1.05*n_c*hi(1,1)))^(-1.8));

                alpha_g = alpha_g_1;
            elseif (n_alpha == 2)

                alpha_g_2 = B*(n_c^(-0.8))*((2*pi*r_o*hi(1,1)/(pi*r_o+
1.05*n_c*hi(1,1)))^(-1.8));

                alpha_g = alpha_g_2;
            elseif (n_alpha == 3)

                alpha_g_3 = D*(n_c^(-0.8))*((2*pi*r_o*hi(1,1)/(pi*r_o+
1.05*n_c*hi(1,1)))^(-1.8));

                alpha_g = alpha_g_3;
            else

                alpha_g_4 = E*(n_c^(-0.8))*((2*pi*r_o*hi(1,1)/(pi*r_o+
1.05*n_c*hi(1,1)))^(-1.8));

                alpha_g = alpha_g_4;
            end
        end
        % diff(1,1) = diff(1,1) %%%debug%%% %
        %converge = converge %%%debug%%% %
        %pause(2.0) %%%debug%%% %
        % handle machining restriction and save the associated alpha:
        if (hi(1,1) > hmax)
            hi(1,1) = hmax
            if (n_alpha == 1)

                alpha_g_1 = A*((mdot_t/n_c)^0.8)*((2*pi*r_o*hi(1,1)/(pi*r_o+
1.05*n_c*hi(1,1)))^(-1.8));

                alpha_g = alpha_g_1;
            elseif (n_alpha == 2)
```

```
                alpha_g_2 = B*(n_c^(-0.8))*((2*pi*r_o*hi(1,1)/(pi*r_o+
1.05*n_c*hi(1,1)))^(-1.8));

                alpha_g = alpha_g_2;
            elseif (n_alpha == 3)

                alpha_g_3 = D*(n_c^(-0.8))*((2*pi*r_o*hi(1,1)/(pi*r_o+
1.05*n_c*hi(1,1)))^(-1.8));

                alpha_g = alpha_g_3;
            else

                alpha_g_4 = E*(n_c^(-0.8))*((2*pi*r_o*hi(1,1)/(pi*r_o+
1.05*n_c*hi(1,1)))^(-1.8));

                alpha_g = alpha_g_4;
            end
            solutions(n_c_e,index) = alpha_g;
        end
        % record and report values for this n_c and alpha_g:
        solutions(n_c_e,index+1) = hi(1,1); % h value, (1,1) because a
                                            % new (1,2) will not be
                                            % recalculated anyway
        hi(1,1) = hi(1,1) % display the determined h value
        %pause(2.0) %%%debug%%% %

        solutions(n_c_e,index+2) = hi(1,1)/solutions(n_c_e,2); % channel AR
value

    end
end
%
% end of program
```

APPENDIX IV: Results of Fin Height Iteration

The results of the fin height iteration are presented in one table in three parts, broken at the jagged lines.

number of channels, n_c	channel width, w, [m]	fin width, delta_f, [m]	mass flow rate per channel, mdot_c, [kg/s]	heat transfer coefficient 1, alpha_g_1, [W/m2-k]	channel (and fin) height, h_1, [m]	channel AR, AR_1
19	0.0009839	0.0010823	0.00094737	2722.4	0.008	8.131
20	0.0009347	0.0010282	0.0009	2837.5	0.008	8.5589
21	0.0008902	0.00097921	0.00085714	2952.7	0.008	8.9869
22	0.0008497	0.0009347	0.00081818	3068	0.008	9.4148
23	0.0008128	0.00089406	0.00078261	3183.4	0.008	9.8427
24	0.0007789	0.00085681	0.00075	3298.8	0.008	10.271
25	0.0007478	0.00082253	0.00072	3414.4	0.008	10.699
26	0.0007190	0.0007909	0.00069231	3547.4	0.0077431	10.769
27	0.0006924	0.00076161	0.00066667	3683.8	0.0074563	10.769
28	0.0006676	0.00073441	0.00064286	3820.2	0.00719	10.769
29	0.0006446	0.00070908	0.00062069	3956.7	0.0069421	10.769
30	0.0006231	0.00068545	0.0006	4093.1	0.0067107	10.769
31	0.0006030	0.00066333	0.00058065	4229.5	0.0064942	10.769
32	0.0005842	0.00064261	0.0005625	4366	0.0062913	10.769
33	0.0005665	0.00062313	0.00054545	4502.4	0.0061006	10.769
34	0.0005498	0.0006048	0.00052941	4638.9	0.0059212	10.769
35	0.0005341	0.00058752	0.00051429	4775.3	0.005752	10.769
36	0.0005193	0.0005712	0.0005	4911.9	0.0055922	10.769
37	0.0005052	0.00055577	0.00048649	5048.3	0.005441	10.769

heat transfer coefficient 2, alpha_g_2, [W/m2-k]	channel (and fin) height, h_2, [m]	channel AR, AR_2	heat transfer coefficient 3, alpha_g_3, [W/m2-k]	channel (and fin) height, h_3, [m]	channel AR, AR_3	heat transfer coefficient 4, alpha_g_4, [W/m2-k]	channel (and fin) height, h_4, [m]
2490.2	0.008	8.131	2985.9	0.008	8.131	2491.1	0.008
2595.5	0.008	8.5589	3112.2	0.008	8.5589	2596.4	0.008
2700.9	0.008	8.9869	3238.5	0.008	8.9869	2701.9	0.008
2806.3	0.008	9.4148	3365	0.008	9.4148	2807.4	0.008
2911.9	0.008	9.8427	3491.6	0.008	9.8427	2913	0.008
3017.5	0.008	10.271	3621.5	0.0079553	10.213	3018.6	0.008
3123.2	0.008	10.699	3772.4	0.0076371	10.213	3124.3	0.008
3228.9	0.008	11.127	3923.3	0.0073434	10.213	3230.1	0.008
3344.2	0.0078447	11.33	4074.2	0.0070714	10.213	3345.5	0.007843
3468	0.0075645	11.33	4225.1	0.0068189	10.213	3469.4	0.0075629
3591.9	0.0073036	11.33	4376	0.0065837	10.213	3593.3	0.0073021
3715.8	0.0070602	11.33	4526.9	0.0063643	10.213	3717.2	0.0070587
3839.6	0.0068324	11.33	4677.7	0.006159	10.213	3841.1	0.006831
3963.5	0.0066189	11.33	4828.6	0.0059665	10.213	3965.1	0.0066175
4087.3	0.0064184	11.33	4979.5	0.0057857	10.213	4089	0.006417
4211.2	0.0062296	11.33	5130.4	0.0056155	10.213	4212.9	0.0062283
4335.1	0.0060515	11.33	5281.3	0.0054551	10.213	4336.9	0.0060503
4459	0.0058834	11.33	5432.2	0.0053036	10.213	4460.8	0.0058822
4582.9	0.0057244	11.33	5583.1	0.0051602	10.213	4584.7	0.0057232

channel AR, AR_4	average alpha	average height	channel half width, [m]	fin half width, [m]	channel half width + fin half width, [m]	
8.131	2672.4	0.008	0.00049195	0.00054115	0.00103310	
8.5589	2785.4	0.008	0.00046735	0.00051410	0.00098145	
8.9869	2898.5	0.008	0.00044510	0.00048961	0.00093470	
9.4148	3011.675	0.0080000	0.00042487	0.00046735	0.00089222	use
9.8427	3124.975	0.0080000	0.00040639	0.00044703	0.00085342	these
10.271	3239.1	0.0079888	0.00038946	0.00042841	0.00081787	channels
10.699	3358.575	0.0079093	0.00037388	0.00041127	0.00078515	only
11.127	3482.425	0.0077716	0.00035950	0.00039545	0.00075495	
11.328	3611.925	0.0075539	0.00034619	0.00038081	0.00072699	
11.328	3745.675	0.0072841	0.00033382	0.00036721	0.00070103	
11.328	3879.475	0.0070329	0.00032231	0.00035454	0.00067685	
11.328	4013.25	0.0067985	0.00031157	0.00034273	0.00065429	
11.328	4146.975	0.0065792	0.00030152	0.00033167	0.00063318	
11.328	4280.8	0.0063736	0.00029210	0.00032131	0.00061340	
11.328	4414.55	0.0061804	0.00028324	0.00031157	0.00059481	
11.328	4548.35	0.0059987	0.00027491	0.00030240	0.00057731	
11.328	4682.15	0.0058272	0.00026706	0.00029376	0.00056082	
11.328	4815.975	0.0056654	0.00025964	0.00028560	0.00054524	
11.328	4949.75	0.0055122	0.00025262	0.00027789	0.00053051	

APPENDIX V: Drawing Coordinates for CFD geometry

n_c =	22				n_c =	23			
(	x	y	z	) mm	(	x	y	z	) mm
A =	0	0	0		A =	0	0	0	
B =	-156.249	0	1.0980		B =	-156.249	0	1.0980	
C =	-156.249	0	9.0980		C =	-156.249	0	9.0980	
D =	-156.249	0.4249	9.0980		D =	-156.249	0.4064	9.0980	
E =	-156.249	0.4249	1.0980		E =	-156.249	0.4064	1.0980	
F =	0	0	1.0980		F =	0	0	1.0980	
G =	0	0.4249	1.0980		G =	0	0.4064	1.0980	
H =	0	0.4249	9.0980		H =	0	0.4064	9.0980	
I =	0	0.8922	9.0980		I =	0	0.8534	9.0980	
J =	0	0.8922	0		J =	0	0.8534	0	
K =	0	0	9.0980		K =	0	0	9.0980	
L =	0	0	10.0980		L =	0	0	10.0980	
M =	0	0.8922	10.0980		M =	0	0.8534	10.0980	
n_c =	24				n_c =	25			
(	x	y	z	) mm	(	x	y	z	) mm
A =	0	0	0		A =	0	0	0	
B =	-156.249	0	1.0980		B =	-156.249	0	1.0980	
C =	-156.249	0	9.0868		C =	-156.249	0	9.0073	
D =	-156.249	0.3895	9.0868		D =	-156.249	0.3739	9.0073	
E =	-156.249	0.3895	1.0980		E =	-156.249	0.3739	1.0980	
F =	0	0	1.0980		F =	0	0	1.0980	
G =	0	0.3895	1.0980		G =	0	0.3739	1.0980	
H =	0	0.3895	9.0868		H =	0	0.3739	9.0073	
I =	0	0.8179	9.0868		I =	0	0.7851	9.0073	
J =	0	0.8179	0		J =	0	0.7851	0	
K =	0	0	9.0868		K =	0	0	9.0073	
L =	0	0	10.0868		L =	0	0	10.0073	
M =	0	0.8179	10.0868		M =	0	0.7851	10.0073	

n_c =	26				n_c =	27			
(	x	y	z	) mm	(	x	y	z	) mm
A =	0	0	0		A =	0	0	0	
B =	-156.249	0	1.0980		B =	-156.249	0	1.0980	
C =	-156.249	0	8.8696		C =	-156.249	0	8.6519	
D =	-156.249	0.3595	8.8696		D =	-156.249	0.3462	8.6519	
E =	-156.249	0.3595	1.0980		E =	-156.249	0.3462	1.0980	
F =	0	0	1.0980		F =	0	0	1.0980	
G =	0	0.3595	1.0980		G =	0	0.3462	1.0980	
H =	0	0.3595	8.8696		H =	0	0.3462	8.6519	
I =	0	0.7550	8.8696		I =	0	0.7270	8.6519	
J =	0	0.7550	0		J =	0	0.7270	0	
K =	0	0	8.8696		K =	0	0	8.6519	
L =	0	0	9.8696		L =	0	0	9.6519	
M =	0	0.7550	9.8696		M =	0	0.7270	9.6519	
n_c =	28				n_c =	29			
(	x	y	z	) mm	(	x	y	z	) mm
A =	0	0	0		A =	0	0	0	
B =	-156.249	0	1.0980		B =	-156.249	0	1.0980	
C =	-156.249	0	8.3821		C =	-156.249	0	8.1309	
D =	-156.249	0.3338	8.3821		D =	-156.249	0.3223	8.1309	
E =	-156.249	0.3338	1.0980		E =	-156.249	0.3223	1.0980	
F =	0	0	1.0980		F =	0	0	1.0980	
G =	0	0.3338	1.0980		G =	0	0.3223	1.0980	
H =	0	0.3338	8.3821		H =	0	0.3223	8.1309	
I =	0	0.7010	8.3821		I =	0	0.6769	8.1309	
J =	0	0.7010	0		J =	0	0.6769	0	
K =	0	0	8.3821		K =	0	0	8.1309	
L =	0	0	9.3821		L =	0	0	9.1309	
M =	0	0.7010	9.3821		M =	0	0.6769	9.1309	

n_c =	30				n_c =	31			
(	x	y	z	) mm	(	x	y	z	) mm
A =	0	0	0		A =	0	0	0	
B =	-156.249	0	1.0980		B =	-156.249	0	1.0980	
C =	-156.249	0	7.8965		C =	-156.249	0	7.6772	
D =	-156.249	0.3116	7.8965		D =	-156.249	0.3015	7.6772	
E =	-156.249	0.3116	1.0980		E =	-156.249	0.3015	1.0980	
F =	0	0	1.0980		F =	0	0	1.0980	
G =	0	0.3116	1.0980		G =	0	0.3015	1.0980	
H =	0	0.3116	7.8965		H =	0	0.3015	7.6772	
I =	0	0.6543	7.8965		I =	0	0.6332	7.6772	
J =	0	0.6543	0		J =	0	0.6332	0	
K =	0	0	7.8965		K =	0	0	7.6772	
L =	0	0	8.8965		L =	0	0	8.6772	
M =	0	0.6543	8.8965		M =	0	0.6332	8.6772	
n_c =	32				n_c =	33			
(	x	y	z	) mm	(	x	y	z	) mm
A =	0	0	0		A =	0	0	0	
B =	-156.249	0	1.0980		B =	-156.249	0	1.0980	
C =	-156.249	0	7.4716		C =	-156.249	0	7.2784	
D =	-156.249	0.2921	7.4716		D =	-156.249	0.2832	7.2784	
E =	-156.249	0.2921	1.0980		E =	-156.249	0.2832	1.0980	
F =	0	0	1.0980		F =	0	0	1.0980	
G =	0	0.2921	1.0980		G =	0	0.2832	1.0980	
H =	0	0.2921	7.4716		H =	0	0.2832	7.2784	
I =	0	0.6134	7.4716		I =	0	0.5948	7.2784	
J =	0	0.6134	0		J =	0	0.5948	0	
K =	0	0	7.4716		K =	0	0	7.2784	
L =	0	0	8.4716		L =	0	0	8.2784	
M =	0	0.6134	8.4716		M =	0	0.5948	8.2784	

n_c =	34				n_c =	35			
(	x	y	z	) mm	(	x	y	z	) mm
A =	0	0	0		A =	0	0	0	
B =	-156.249	0	1.0980		B =	-156.249	0	1.0980	
C =	-156.249	0	7.0967		C =	-156.249	0	6.9252	
D =	-156.249	0.2749	7.0967		D =	-156.249	0.2671	6.9252	
E =	-156.249	0.2749	1.0980		E =	-156.249	0.2671	1.0980	
F =	0	0	1.0980		F =	0	0	1.0980	
G =	0	0.2749	1.0980		G =	0	0.2671	1.0980	
H =	0	0.2749	7.0967		H =	0	0.2671	6.9252	
I =	0	0.5773	7.0967		I =	0	0.5608	6.9252	
J =	0	0.5773	0		J =	0	0.5608	0	
K =	0	0	7.0967		K =	0	0	6.9252	
L =	0	0	8.0967		L =	0	0	7.9252	
M =	0	0.5773	8.0967		M =	0	0.5608	7.9252	
n_c =	36				n_c =	37			
(	x	y	z	) mm	(	x	y	z	) mm
A =	0	0	0		A =	0	0	0	
B =	-156.249	0	1.0980		B =	-156.249	0	1.0980	
C =	-156.249	0	6.7634		C =	-156.249	0	6.6102	
D =	-156.249	0.2596	6.7634		D =	-156.249	0.2526	6.6102	
E =	-156.249	0.2596	1.0980		E =	-156.249	0.2526	1.0980	
F =	0	0	1.0980		F =	0	0	1.0980	
G =	0	0.2596	1.0980		G =	0	0.2526	1.0980	
H =	0	0.2596	6.7634		H =	0	0.2526	6.6102	
I =	0	0.5452	6.7634		I =	0	0.5305	6.6102	
J =	0	0.5452	0		J =	0	0.5305	0	
K =	0	0	6.7634		K =	0	0	6.6102	
L =	0	0	7.7634		L =	0	0	7.6102	
M =	0	0.5452	7.7634		M =	0	0.5305	7.6102	

CURRICULUM VITA

Christopher Bradford is a native (odd to most locals) of El Paso, Texas, graduating from Andress High School in the top 3% of the May 1999 class. Moving on with ephemeral hope for the future, he soon discovered the inadequate preparedness for college and an indication into the true nature of human interaction that his prior years had not afforded. Transferring from The University of Arizona and New Mexico State University, he eventually graduated with a Bachelor of Science degree in Aerospace Engineering from Texas A&M University in May of 2005, although at many times he imagined the benefit of attending a different university. Soon after graduation he realized the negative potential that a lack of knowledge in other fields of study could have on his future, discovering through experience that simply following a standardized curriculum does not necessarily guarantee a person has much intelligence. He thus began taking the initiative to learn from many fields including philosophy, sociology, physics, and other engineering disciplines to supplement his multiple interests and talents, as he highlights at www.myspace.com/christopher_aerospace, if hosting services remain available. While daydreaming, he often ponders the futility of personal human desires, and the true value of money. However, he provides non-legally-binding,, no-liability, academic-style consultation services for a nominal fee when scheduled in advance at "christopherbradford at yahoo dot com" (if email services remain available), because he realized from Plato's writings on Socrates that knowledge itself may fulfill the intellect but not necessarily the stomach. Returning to academia after multiple career ventures, he expects to earn a Master of Science degree in Mechanical Engineering from The University of Texas at El Paso in the summer of 2011. Christopher does not consider himself to reside at any permanent address, for various reasons.